Supercontinuum generation in the silicon nitride platform

Yijun Yang

université PARIS-SACLAY

Supercontinuum generation in the silicon nitride platform

Génération de supercontinuum dans la platforme de nitrure de silicium

Thèse de doctorat de l'université Paris-Saclay

École doctorale n°575: electrical, optical, bio: physics and engineering (EOBE)
Spécialité de doctorat: Electronique, Photonique et Micro-Nanotechnologies Graduate School : Sciences de l'ingénierie et des systèmes Référent : Faculté des sciences d'Orsay

Thèse préparée dans le **Centre de Nanosciences et de Nanotechnologies (Université Paris-Saclay, CNRS)**,
sous la direction de **Laurent VIVIEN**, Directeur de recherche

Thèse soutenue à Paris-Saclay, le 11 decembre 2024, par

Yijun YANG

Composition du jury

Membres du jury avec voix délibérative

Nicolas DUBREUIL Professeur, Institut d'Optique Graduate School, Université Paris-Saclay	Président
Arnaud MUSSOT Professeur, Université de Lille	Rapporteur & Examinateur
Frédéric GARDES Professeur, University of Southampton	Rapporteur & Examinateur
Benjamin WETZEL Chargé de recherche, XLIM Research Institute, Université de Limoges	Examinateur
Quentin WILMART Ingénieur de recherche, CEA-LETI, Université Grenoble Alpes	Examinateur

THESE DE DOCTORAT
NNT : 2024UPAST163

université PARIS-SACLAY

ÉCOLE DOCTORALE
Physique et ingénierie : Electrons, Photons, Sciences du vivant (EOBE)

Titre: Génération de supercontinuum dans la plateforme de nitrure de silicium
Mots clés: photonique au silicium, optique non linéaire, génération de supercontinuum, quasi-accord de phase, compression d'impulsions

Résumé: De nos jours, diverses sources de lumière dans différentes gammes de longueurs d'onde jouent un rôle important tant pour les industries modernes que dans la vie quotidienne des gens, notamment dans les domaines du laser, de la détection, du traitement médical, de la biologie, des télécommunications, etc. La voie cruciale vers la génération de lumière dans une gamme de longueurs d'onde ciblée repose sur l'optique non linéaire, qui se concentre sur l'interaction de la lumière intense avec la matière, entraînant une conversion de fréquence. Avec le réchauffement climatique au centre des préoccupations, la demande de solutions énergétiquement efficaces ne cesse de croître. Parallèlement, la tendance croissante vers les dispositifs portables appelle à des technologies non linéaires innovantes, intégrées et légères qui peuvent être mises en œuvre dans des supports mobiles tels que les humains, les voitures, les drones et les satellites. L'émergence de la photonique sur silicium, qui utilise des matériaux compatibles avec la technologie du silicium tels que le silicium (Si), le nitrure de silicium (Si_3N_4) et le germanium (Ge) pour fabriquer des composants optiques intégrés, répond à ces besoins.

Grâce à son indice de réfraction élevé, son abondance sur Terre et ses procédés de fabrication matures hérités de l'industrie des semi-conducteurs, la photonique sur silicium permet la création de dispositifs photoniques à haute fonctionnalité avec des avantages clés : faible coût, faible consommation d'énergie et évolutivité. En particulier, la forte non-linéarité et le haut indice de réfraction peuvent considérablement réduire la consommation d'énergie nécessaire pour les applications d'optique non linéaire. Au cours de ma thèse, je me suis concentré sur l'exploitation d'un aspect de l'optique non linéaire dans la photonique sur silicium : la génération de supercontinuum (SCG), une source à large bande spectrale qui peut être adaptée à des applications médicales, de spectroscopie et de métrologie, dans les guides d'onde en Si_3N_4. J'ai travaillé à optimiser tous les aspects de la SCG au sein d'une plateforme intégrée en Si_3N_4 afin de créer une solution hautement personnalisable et économe en énergie. Mon objectif ultime était de développer une SCG avec des exigences de puissance de pompe réduites, en adéquation avec les récents progrès dans les lasers à verrouillage de mode intégrés, et de produire un spectre adapté à diverses applications dans les gammes visibles et NIR.

Mon travail inclut la fabrication et la caractérisation des guides d'onde dans un premier temps. Différentes méthodes ont été développées pour caractériser les pertes de propagation, la géométrie des guides d'onde et la dispersion des guides d'onde. Ensuite, une nouvelle condition de quasi-accord de phase sera ajoutée à l'ingénierie de la dispersion actuelle, apportant une grande flexibilité pour contrôler l'élargissement spectral. La clé réside dans la modulation de dispersion importante et contrôlable par la variation de la largeur du guide d'onde. Troisièmement, la compression d'impulsion auto-similaire est proposée sur la plateforme en Si_3N_4, où l'impulsion est amplifiée et compressée. Des simulations ont été réalisées pour déterminer les paramètres adéquats permettant sa réalisation dans un guide d'onde de 5 cm de long, y compris le gain, la puissance initiale de la pompe, la dispersion et la forme initiale de l'impulsion. Un nouveau compresseur d'impulsion est finalement présenté pour démontrer le potentiel de compression d'impulsions atteignant moins de 200 fs.

Ce travail se concentre sur la réalisation de la SCG dans une plateforme de photonique sur silicium. Les méthodes innovantes présentées dans ce manuscrit offrent le potentiel de réaliser un système SCG totalement intégré sur puce, avec un élargissement spectral adaptable à diverses applications.

université PARIS-SACLAY

ÉCOLE DOCTORALE
Physique et ingénierie : Electrons, Photons, Sciences du vivant (EOBE)

Title: Supercontinuum generation in the silicon nitride platform

Keywords: silicon photonics, nonlinear optics, supercontinuum generation, quasi-phase matching, pulse compression

Abstract: Nowadays, various light sources in different wavelength ranges serve an important role both for modern industries and people's daily lives, including laser, detection, medical treatment, biology, telecommunications, and so on. The crucial way to achieve a light source in a targeted wavelength range lies in nonlinear optics, which are centered on strong light interacting with matters to trigger frequency conversion. With global warming at the forefront of concerns, there is a growing demand for energy-efficient alternatives to current solutions. In the same time, the trend towards portable devices is on the rise. This shift requires innovative, integrated, and lightweight nonlinear technologies. These technologies should be suitable for various moving carriers, including humans, cars, drones, and satellites. These challenges can be addressed by the emergence of silicon photonics. This technology utilizes silicon (Si) compatible materials such as silicon nitride (Si_3N_4) and germanium (Ge) to fabricate on-chip optical components.

Due to its high refractive index, abundant quantity on Earth, and mature fabrication inherited from the semiconductor industry, silicon photonics enables the creation of high-functionality photonic devices with key advantages: low cost, low power consumption, and scalability. Particularly, the high nonlinearity, high refractive index can drastically decrease the power consumption needed for nonlinear optics applications. During my thesis, I focus on exploiting one aspect of the nonlinear optics on silicon photonics: supercontinuum generation (SCG), a broadband source, the spectrum of which can be tailored for medical use, spectroscopy and metrology, in Si_3N_4 waveguides. I focused on optimizing every aspect of SCG within an integrated Si_3N_4 platform to create a highly customizable and power-efficient solution. My ultimate goal was to develop an SCG with reduced pump power requirements, aligning with recent advancements in integrated mode-locked lasers, and to produce a spectrum suitable for various applications in the visible and NIR ranges.

My work includes the fabrication and characterization of the waveguide in the first place. Different methods are developed to characterize propagation loss, waveguide geometry and waveguide dispersion. Then, a novel quasi-phase-matching condition will be added to the current dispersion engineering, bringing huge flexibility to control the spectral broadening. The key lies on the controllable large dispersion modulation through waveguide width variation. Third, self-similar pulse compression is proposed to Si_3N_4 platform where the pulse is amplified and compressed. Simulations are made to find out the adequate parameters that enable the realisation in a 5-cm long waveguide, including the gain, initial pump power, dispersion and initial pulse shape. A novel pulse compressor is finally presented to show the potential of pulse compression reaching below 200 fs.

This work focuses on the realization of SCG within a silicon photonics platform. The innovative methods presented in this manuscript hold the potential for the realization of a fully integrated on-chip SCG system, with spectral broadening that can be tailored for various applications.

Contents

1 - Synthèse en français du manuscrit du thèse

Le développement rapide de la photonique au silicium en tant que domaine clé de la photonique intégrée a été stimulé par les progrès de l'industrie des semi-conducteurs au silicium, qui remontent aux années 1980. La photonique au silicium offre un indice de réfraction élevé, une évolutivité, une faible consommation d'énergie et un bon rapport coût-efficacité, grâce aux processus de fabrication éprouvés hérités de la fabrication des semi-conducteurs. Avec des applications allant des communications de données et de l'informatique optique à la détection et à l'imagerie, la photonique au silicium révolutionne la manière dont l'information est traitée, transmise et détectée.
L'une des caractéristiques prometteuses de la photonique au silicium est sa capacité à exploiter l'optique non linéaire. Les guides d'ondes intégrés en silicium présentent un fort confinement des modes optiques, une non-linéarité élevée et des géométries personnalisables, ce qui les rend idéaux pour des interactions non linéaires efficaces. La taille réduite des guides d'ondes intégrés par rapport à la fibre ou à l'optique de masse permet de miniaturiser les systèmes optiques, d'améliorer les interactions entre la lumière et la matière et de réduire les besoins en énergie.
La génération de supercontinuum (SCG), un processus non linéaire dans lequel une impulsion laser intense subit un élargissement spectral important, a suscité une attention considérable en tant que source de lumière à longueurs d'onde multiples. La génération de supercontinuum permet d'accéder à des longueurs d'onde éloignées de la pompe, avec une intensité spectrale élevée, ce qui favorise une série d'applications telles que l'imagerie, la métrologie et la spectroscopie.
Dans ma thèse, je me suis concentré sur l'optimisation de la SCG au sein d'une plate-forme intégrée en Si_3N_4 afin de développer une solution hautement personnalisable et économe en énergie. Le Si_3N_4, un matériau compatible avec le silicium, offre de faibles pertes et une large fenêtre de transparence allant du visible à l'infrarouge moyen. Mon objectif était de créer une SCG flexible avec des exigences réduites en termes de puissance de pompe, en accord avec les avancées récentes dans les lasers à verrouillage de modes intégrés, et de produire un spectre adapté à diverses applications dans les gammes visible et proche infrarouge (NIR). Cette thèse présente deux résultats clés :

- Introduction d'une nouvelle condition de quasi-accord de phase pour améliorer l'ingénierie de la dispersion et contrôler l'élargissement spectral.
- Proposition d'une compression d'impulsions auto-similaires dans la plate-forme Si_3N_4 afin d'amplifier et de comprimer l'impulsion, réduisant ainsi le besoin de pompes ultra-courtes et de forte puissance dans la SCG.

Principe de la génération de supercontinuum dans les guides d'ondes en Si_3N_4

Le supercontinuum dans un guide d'ondes en Si_3N_4 résulte de la non-linéarité optique du troisième ordre et de la dispersion du guide d'ondes. Pour la plupart des matériaux compatibles avec la technologie du silicium, comme le nitrure de silicium (Si_3N_4), leur centro-symétrie présente donc uniquement une non-linéarité du troisième ordre, connue sous le nom d'effet Kerr optique. Parmi les différents effets non-linéaires résultant de l'effet Kerr optique, tels que

la génération de la troisième harmonique et le mélange à quatre ondes, le phénomène le plus important qui contribue à la SCG est la modulation de phase auto-induite (SPM). La SPM provient de la contribution non-linéaire à l'indice de réfraction. L'indice de réfraction n peut s'écrire comme :

$$n(\omega, I) = n_0(\omega) + n_2 I \tag{1.1}$$

où n_0 est l'indice de réfraction linéaire, I est l'intensité optique, et n_2 est l'indice non-linéaire. n_2 est directement lié à $\chi^{(3)}$ et est une valeur intrinsèque pour chaque matériau. Par exemple, $n_{2,\mathrm{Si_3N_4}}$ est égal à $2.4 \times 10^{-19}\,\mathrm{m^2/W}$.
Une interprétation schématique de la SPM est présentée dans la Figure.1.1(a), où le champ E et l'intensité spectrale correspondante d'une impulsion à une distance donnée z sont montrés sans et avec SPM. Lorsque $n_2 > 0$ (ce qui est généralement le cas), la SPM introduit un chirp en fréquence croissant du bord avant au bord arrière, tandis que la forme de l'enveloppe temporelle reste intacte. Dans le domaine fréquentiel, de nouvelles fréquences sont générées symétriquement sous forme de lobes latéraux autour de la fréquence centrale de l'impulsion ω_0.

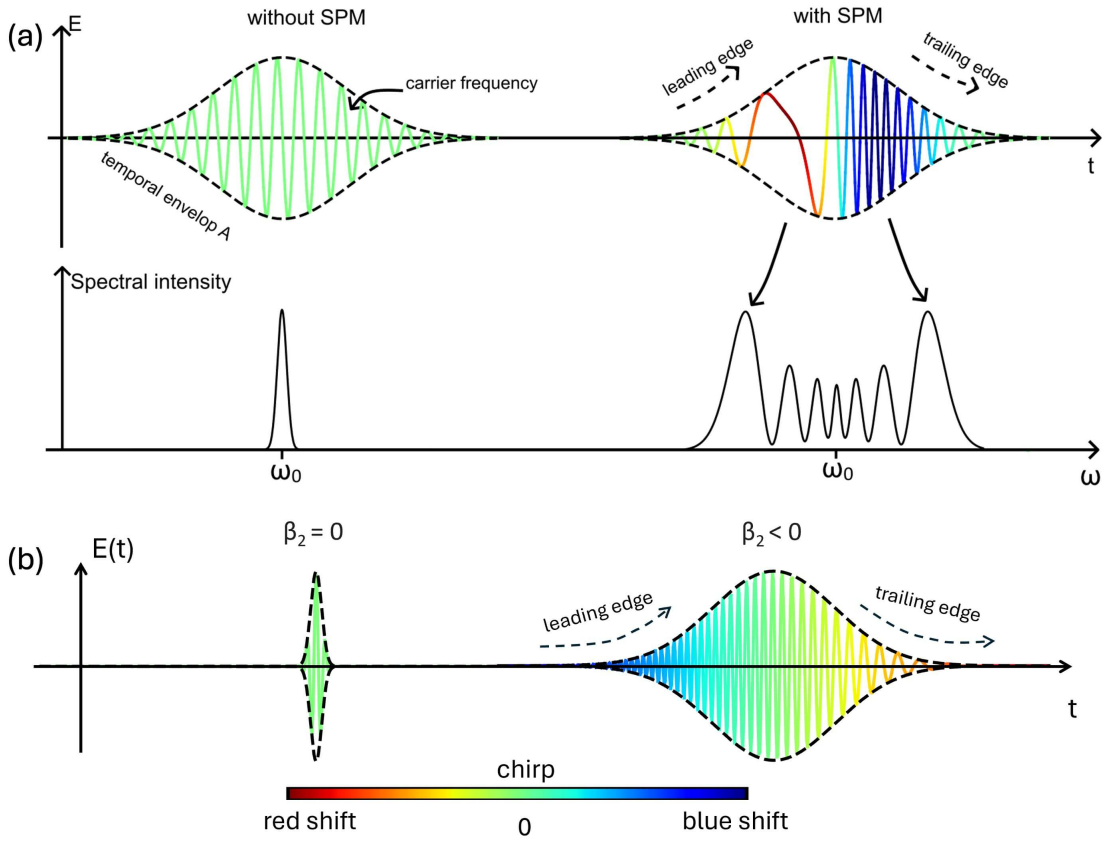

Fig. 1.1. Illustration schématique de la modulation de phase auto-induite et de la vitesse de groupe sur une impulsion. La fréquence instantanée est indiquée par la couleur, où le vert désigne l'absence de chirp et le rouge et le bleu signifient respectivement un chirp négatif et positif. (a) Le champ optique, sans et avec SPM, est représenté en haut, accompagné de leur intensité spectrale correspondante en bas. (b) Le champ de l'impulsion de forme gaussienne initiale est montré à gauche, tandis que le champ tenant compte de la GVD ($\beta_2 < 0$) est montré à droite.

La dispersion de la vitesse de groupe (GVD), exprimée par β_2, est la dispersion du guide d'ondes

qui commence à avoir un effet réel pendant la propagation de l'impulsion. En ce qui concerne le signe, la GVD peut être anormale, où $\beta_2 < 0$ (Figure.1.1(b)), et normale, où $\beta_2 > 0$, respectivement. La longueur d'onde où $\beta_2 = 0$ est appelée longueur d'onde de dispersion nulle (ZDW).
Lorsqu'on combine SPM avec une GVD anormale, le spectre peut s'élargir en raison de la formation de solitons. Dans la Figure.1.2(a), la figure montre l'évolution spectrale d'un soliton avec un nombre de soliton $N = 9$. Lorsque la dispersion d'ordre supérieur β_3 est introduite, des ondes dispersives (DW) peuvent être générées, permettant la conversion d'énergie vers des longueurs d'onde éloignées de la pompe. En considérant tous les ordres de la dispersion d'ordre supérieur, une simulation précise est montrée dans la Figure.1.2(c) utilisant l'Équation de Schrödinger non linéaire (NLSE), montrant des transferts d'énergie significatifs de la pompe vers la DW. La caractéristique temporelle de la DW est montrée dans la Figure.1.2(d). La DW est générée après la fission du soliton et est séparée de la partie soliton en raison de la grande différence de vitesse de groupe.

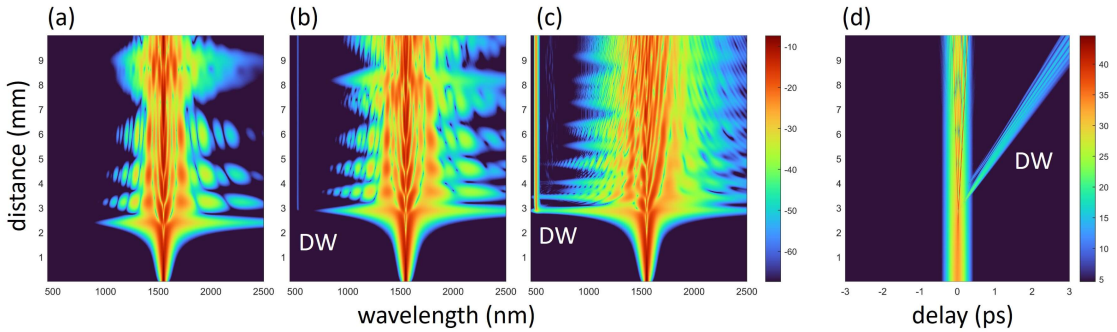

Fig. 1.2. Effet de la dispersion d'ordre supérieur (HOD) sur la génération d'onde dispersive (DW). (a) Seule $\beta_2 = -300\,\mathrm{ps}^2/\mathrm{km}$ est considérée. (b) Une HOD supplémentaire $\beta_3 = -0.38\,\mathrm{ps}^3/\mathrm{km}$ est considérée. (c) La dispersion complète est considérée. (d) L'évolution temporelle simulée de l'impulsion est donnée dans les mêmes conditions que (c), à partir de laquelle la DW est identifiée.

Fabrication du guide d'onde au C2N

La fabrication du guide d'onde en Si_3N_4 est réalisée au C2N. Tout d'abord, une épaisseur adéquate de résine photosensible est déposée sur la plaquette. Ensuite, un petit échantillon est découpé à partir de cette plaquette. La lithographie par faisceau d'électrons suit ensuite le design pour exposer la zone, définissant les parties à retirer par la suite. Après cela, l'échantillon est immergé dans une solution de développement pour retirer la résine exposée au faisceau d'électrons, ne laissant que la résine protectrice sur le motif du design. Par la suite, l'échantillon est gravé à sec afin d'obtenir une paroi latérale isotrope. Avant d'être prêt pour la caractérisation, l'échantillon est nettoyé pour éliminer toute résine restante à la surface. Une étape supplémentaire de recuit peut être introduite dans le processus de fabrication afin de lisser la rugosité des parois latérales et de réduire l'absorption des liaisons N-H.
Une inspection des parois latérales d'un guide d'onde de type strip en Si_3N_4 est réalisée pour évaluer la rugosité, un paramètre crucial pour déterminer les pertes de propagation. Comme le montre la Figure 1.3(b), les parois latérales apparaissent lisses sans rugosité significative détectée. Après le processus de fabrication, l'échantillon est clivé pour observer la section transversale

du guide d'onde, montrée dans la Figure 1.3(c). Le guide d'onde est situé au centre et isolé par deux tranchées. La couche isolante de SiO_2 a une épaisseur de 3 μm. L'imagerie microscopique montre que de nombreux micropiliers sont présents dans les tranchées (Figure 1.3(d)). Ces micropiliers ont une forme rappelant un sapin de Noël. Une explication possible de la formation de ces micropiliers est que la recette de gravure à sec passiverait la surface du Si_3N_4, agissant comme un masque empêchant la gravure.

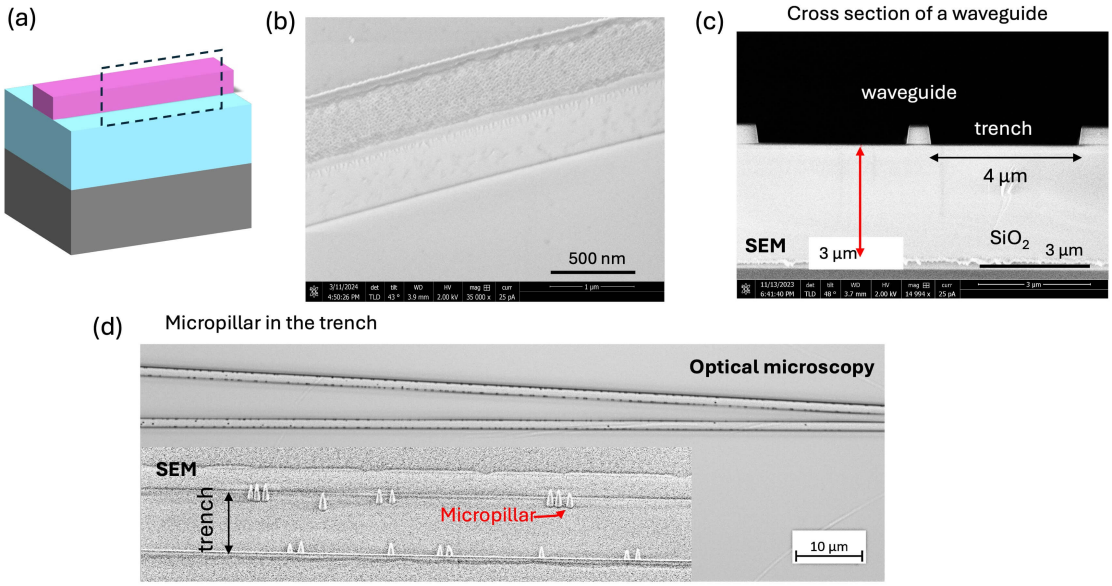

Fig. 1.3. Caractérisation de la qualité du guide d'onde. (a) Illustration d'un guide d'onde de type strip. (b) Image MEB de la paroi latérale d'un guide d'onde. (c) Image MEB de la section transversale. (d) Vue de dessus d'un guide d'onde effilé, où des micropiliers sont présents dans la tranchée. L'image MEB des micropiliers est présentée dans l'encadré.

En plus de la caractérisation de la forme du guide d'onde, la mesure des pertes est également cruciale pour évaluer la qualité du processus. L'analyse du spectre de transmittance d'un résonateur en anneau (Figure.1.4(a)) offre une solution compacte. Une source laser accordable de 1500 nm à 1640 nm est injectée dans le résonateur en anneau pour la mesure de la transmittance.
Pour une résonance donnée, la transmission chute aux longueurs d'onde où l'amplitude du champ s'accumule dans l'anneau. Un exemple de résonance est illustré dans la Figure.1.4(b), où les points de mesure sont ajustés par une fonction lorentzienne qui peut être appliquée pour ajuster la résonance dégénérée comme suit:

$$f(\nu) = -A\frac{1}{1+(\frac{\nu-\nu_{res}}{\Delta\nu_{FWHM}/2})^2} + B(\nu) \tag{1.2}$$

où ν_{res} est la fréquence moyenne de la distribution correspondant à la fréquence de résonance, $\Delta\nu_{\mathrm{FWHM}}$ est la largeur à mi-hauteur, A est l'amplitude et $\mathrm{B}(\nu)$ est la réponse du système de couplage servant de décalage.
En appliquant la méthode des moindres carrés, un ensemble de valeurs $(\mathrm{A},\ \nu_{\mathrm{res}},\ \Delta\nu_{\mathrm{FWHM}})$ peut être trouvé pour chaque résonance, permettant de calculer le facteur de qualité $Q = \frac{\nu_{res}}{\Delta\nu_{FWHM}}$, la finesse $\mathcal{F} = \frac{\Delta\nu_{FSR}}{\Delta\nu_{FWHM}}$ de la résonance, et le rapport d'extinction $\mathcal{E} = \frac{T_{max}}{T_{min}} = \frac{B(\nu_{res})}{B(\nu_{res})-A}$. La perte de propagation peut être calculée à partir de la finesse $\mathcal{F}$ et du rapport d'extinction $\mathcal{E}$

d'une résonance. Une perte de propagation moyenne du guide d'onde de 1100 nm de large est de 0.17 dB/cm dans la gamme spectrale de 1400 nm à 1640 nm (Figure.1.4(c)).

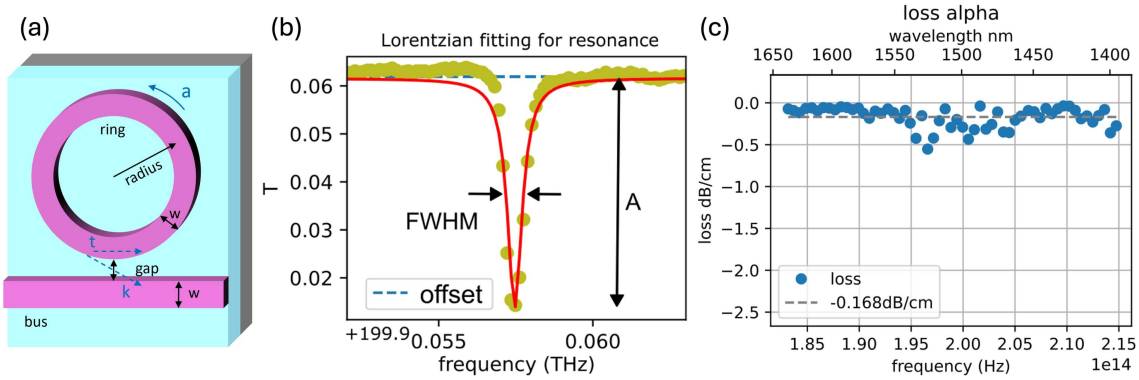

Fig. 1.4. Mesure des pertes par transmission d'un résonateur en anneau. (a) Configuration d'un résonateur en anneau tout-passe. (b) Transmission autour d'une résonance. (c) Pertes de propagation mesurées à partir de l'ajustement des résonances.

Génération de supercontinuum à la quasi-accord de phase

La génération d'ondes dispersives (DW) dans un guide d'ondes à largeur constante est déterminée par sa condition d'accord de phase (PM). Comme la condition de PM est directement liée à la dispersion du guide d'ondes, la position spectrale de la DW est gouvernée par la section transversale spécifique du guide d'ondes. En revanche, l'application du quasi-accord de phase (QPM), obtenu par la modulation de la dispersion le long de la propagation dans le guide d'ondes, permet la génération de multiples DWs. Nous définissons la génération de supercontinuum à quasi-accord de phase (QPM-SCG) comme le supercontinuum avec des DWs générées selon leurs conditions de QPM (QPM-DWs). Le guide d'ondes qui supporte QPM-SCG est ensuite appelé le guide d'ondes QPM.

Lorsqu'un guide d'ondes présente des variations périodiques de largeur entre w_1 et w_2 le long de la direction de propagation, comme illustré dans la Figure.1.5(b), cela introduit une modulation de GVD pour une impulsion en propagation. Ici, l_1 et l_2 représentent les longueurs des largeurs de guide d'ondes w_1 et w_2 au sein d'une période Λ. La modulation de GVD contribue à un terme supplémentaire dans la condition de PM pour la génération de DW, conduisant à la condition QPM suivante :

$$\beta_{eff}(\omega) - \beta_{eff}(\omega_s) - v_{g,eff}^{-1}(\omega - \omega_s) - \frac{\gamma P_s}{2} = \frac{2\pi}{\Lambda} m \tag{1.3}$$

Le côté droit de l'Équation.1.3 montre l'élan supplémentaire où Λ est la période de modulation de la GVD et m est le numéro d'ordre. Bien que la variation de GVD ne soit pas nécessairement une fonction monotone de la variation de largeur, leurs modulations partagent généralement la même période.

Une vue schématique de la génération QPM-SCG est présentée dans la Figure.1.5(c), qui peut être décrite comme suit. Une fois que l'impulsion laser de pompe est envoyée dans la région anormale de la GVD du guide d'ondes QPM définie par $\beta_{2,eff}$, elle subit une évolution d'impulsion sous la condition effective de β_{eff}, aboutissant à la formation d'un soliton. Lorsque le soliton est perturbé par la HOD, plusieurs QPM-DWs sont générées là où les conditions QPM

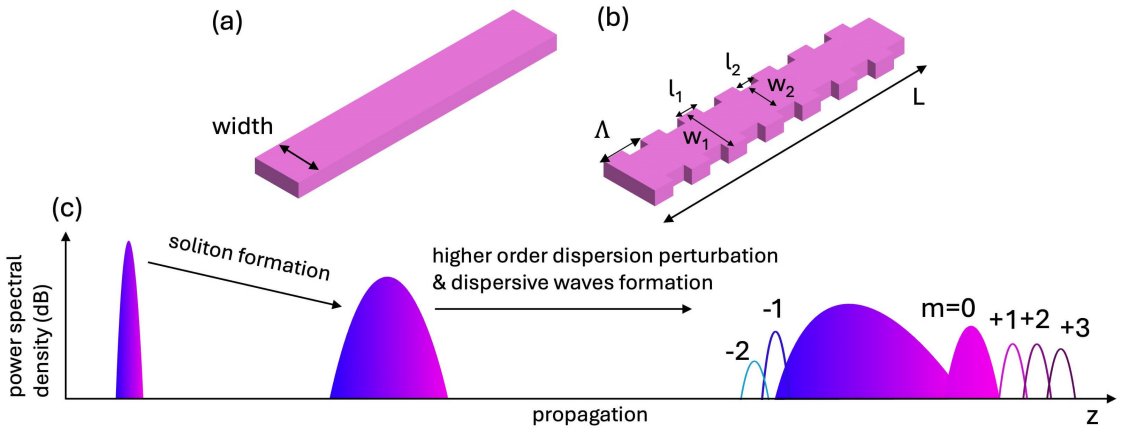

Fig. 1.5. Illustration de la SCG dans un guide d'ondes à quais-accord de phase (QPM). (a) Un guide d'ondes conventionnel à largeur invariée. (b) Un guide d'ondes QPM. (c) Le concept de QPM-SCG : une pompe crée un soliton qui génère des QPM-DWs à des longueurs d'onde définies par la condition QPM.

sont satisfaites, créant ainsi le QPM-SCG.

La vue schématique d'un vrai guide d'ondes Si_3N_4 à QPM est reportée dans la Figure.1.6(a). Le guide d'ondes en spirale, épais de 800 nm et long de 4,3 cm, a été fabriqué au CEA LETI, France. Les indices de réfraction linéaire et non linéaire sont respectivement de 1,98 à une longueur d'onde de 1380 nm mesurée par ellipsométrie et de 2.4×10^{-19} m^2/W selon la littérature. Le guide d'ondes consiste en une alternance périodique de largeurs, allant de 1100 nm à 700 nm dans la direction de propagation (direction longitudinale). Cette configuration, illustrée dans la Figure.1.6(a), incorpore des rétrécissements linéaires pour faciliter les transitions de mode entre les largeurs variées. La largeur du guide d'ondes est fixée à 1100 nm dans les sections droites, se rétrécissant à 700 nm dans les régions de courbure. La perte de propagation est aussi faible que 0,3 dB/cm.

La géométrie du guide d'ondes présente une profondeur de modulation de GVD substantielle de 300 ps^2km^{-1} de la GVD anormale ($w = 1100\,\text{nm}$) à la GVD normale ($w = 700\,\text{nm}$) (Figure.1.6(b)), instiguant ainsi un fort effet QPM à une longueur d'onde de pompe de 1380 nm. La structure en spirale avec des sections de largeur fixe alternée induit un profil de GVD à fort cycle de service dans la direction longitudinale avec une fréquence spatiale légèrement décalée centrée à $393\,m^{-1}$ ($\Lambda = 2.54\,\text{mm}$).

L'élargissement spectral est caractérisé par un laser à femtosecondes. Un laser de pompage polarisé TE de 190 fs (T_{FWHM}) est centré à une longueur d'onde de 1380 nm.

La Figure 1.7(a) montre la densité spectrale de puissance normalisée (PSD) pour l'élargissement spectral expérimental sous une puissance de pompage de crête sur puce de 110 W (courbe noire). Le résultat simulé obtenu en utilisant l'Équation de Schrödinger Nonlinéaire Généralisée (GNLSE) pour la même puissance de crête est montré en rouge. Un bon accord est observé entre la simulation et la mesure avec l'observation de plusieurs pics à des longueurs d'onde d'environ 1104 nm, 1180 nm, 1800 nm, 1930 nm, 2000 nm et 2065 nm. Ces pics, induits par le QPM se produisant le long du guide d'ondes, étendent le spectre de 1050 nm à 2100 nm, couvrant un élargissement d'octave dans une plage de transmission de -40 dB au sein de la limite de détection. Les positions des longueurs d'onde des QPM-DWs déterminées graphiquement sont montrées dans la Figure 1.7(b) par des lignes vertes. En plus de l'ordre 0, les ordres de QPM-DWs allant de -2 à +3 sont identifiés.

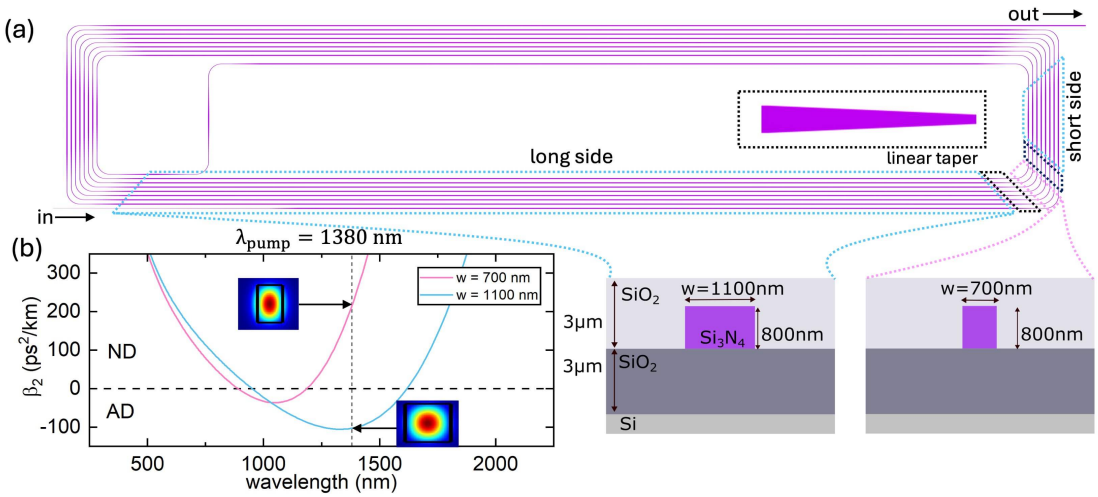

Fig. 1.6. Un guide d'ondes QPM en spirale en Si_3N_4. (a) Les guides d'ondes droits aux côtés courts et longs ont une largeur de $w = 1100\,\text{nm}$, tandis que le guide d'ondes dans le virage a une largeur de $w = 700\,\text{nm}$. Des rétrécissements linéaires permettent la transition des modes optiques entre les deux largeurs de guide d'ondes. Les sections transversales du guide d'ondes sont montrées dans le coin inférieur droit. (b) Courbe de GVD pour les deux géométries de guide d'ondes $w = 1100\,\text{nm}$ et $700\,\text{nm}$. Les distributions d'intensité du mode TE correspondant sont également montrées à la longueur d'onde de pompe de 1380 nm.

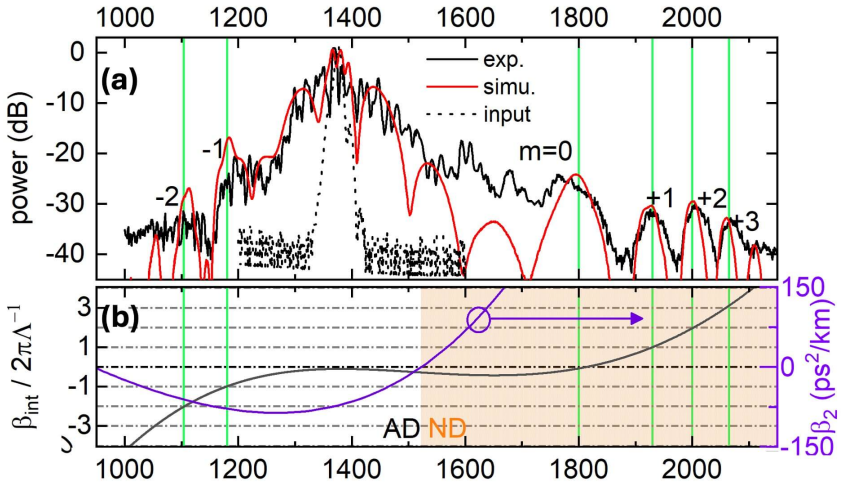

Fig. 1.7. Élargissement spectral du guide d'ondes QPM à une longueur d'onde de pompage de 1380 nm et une puissance de crête de 110 W. (a) Densité spectrale de puissance normalisée des spectres expérimentaux et simulés provenant du guide d'ondes en spirale QPM. Le spectre du pouls de pompage d'entrée est également inclus. (b) Axe de gauche : paramètre de désaccord de phase en noir. Différents ordres du terme QPM sont notés par des lignes horizontales grises en pointillé. Les solutions graphiques des conditions QPM sont rapportées par des lignes verticales vertes. Axe de droite : le paramètre GVD est montré en violet, incluant les régions de dispersion normale (ND, en arrière-plan jaune) et de dispersion anormale (AD, en arrière-plan blanc).

Compression d'impulsion auto-similaire sur puce

Un système idéal de génération de supercontinuum sur puce peut être réalisé en intégrant une source laser sur puce directement avec le guide d'ondes qui déclenche la SCG. Pour une SCG efficace et cohérente, qui vise à atteindre à la fois une large couverture spectrale et une haute cohérence temporelle, la durée du pouls laser de pompage doit idéalement être inférieure à 200 fs. En pratique, pour générer efficacement des ondes dispersives (DW) avec un rendement de conversion élevé d'environ 10% dans la plage de longueurs d'onde ciblée, une durée de pouls de l'ordre de dizaines de femtosecondes est fortement préférée. Les sources laser sur puce à la pointe de la technologie atteignent généralement des durées de pouls dans la plage des picosecondes ou sous-picosecondes avec une puissance de crête de 1 watt. Ainsi, la compression des pouls est un élément clé pour réaliser une SCG sur puce.
Dans ce contexte, le schéma de compression auto-similaire, qui a été largement étudié en optique des fibres, est appliqué à la plateforme intégrée en Si_3N_4. Une illustration est fournie dans la Figure.1.8. Le schéma se compose de deux étapes. Dans la première étape, le pouls initial se propage dans un milieu amplificateur avec une dispersion normale, ce qui entraîne un pouls en forme de parabole amplifié. L'objectif est de tirer parti des phénomènes de propagation auto-similaire pour générer des pouls à décalage linéaire avec une puissance suffisante. Dans la seconde étape, un compresseur de pouls à large bande est utilisé pour compresser le pouls. Une configuration novatrice d'un compresseur de pouls à base de réseau dispersif est proposée pour atteindre la largeur de bande nécessaire à la compression de la durée du pouls à moins de 200 fs. Ce design promet d'être utile pour des applications dans la génération de supercontinuum cohérente utilisant des lasers de pompage à impulsion picoseconde.

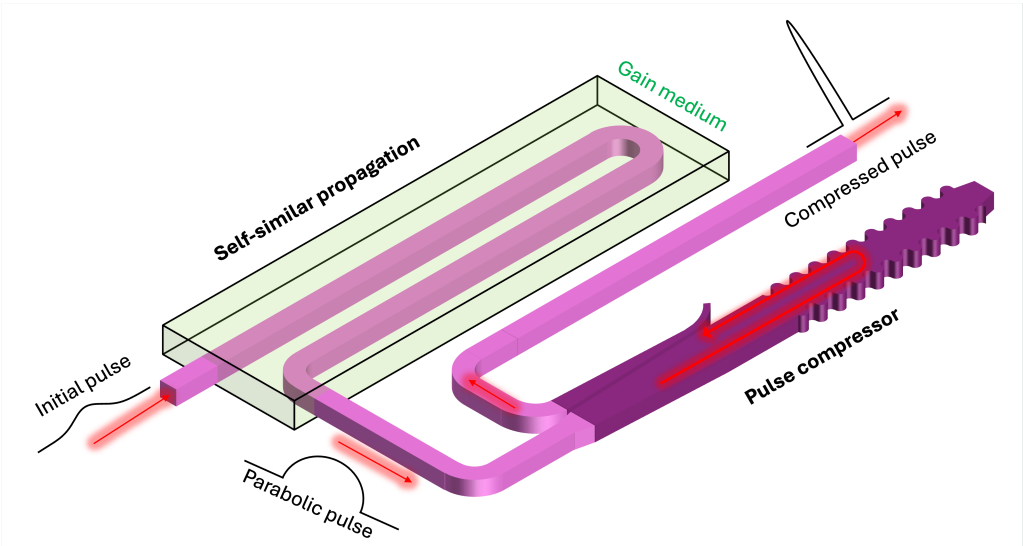

Fig. 1.8. Illustration d'une compression de pulse auto-similaire sur puce. Le pulse initial se propage d'abord dans un guide d'ondes avec gain, subissant une propagation auto-similaire. Ensuite, un compresseur de pulse réaligne le chirp pour compresser le pulse.

Les impulsions se propagent dans un guide d'ondes qui présente une GVD normale et subissent un phénomène appelé rupture d'onde optique (OWB), qui linéarise le chirp de fréquence. De plus, lorsque le gain distribué est introduit pendant la propagation, la forme de l'impulsion d'entrée converge progressivement et asymptotiquement vers une impulsion parabolique présen-

tant des caractéristiques auto-similaires, indépendamment de la forme de l'impulsion initiale. L'impulsion en propagation auto-similaire présente des caractéristiques fascinantes en ce qui concerne le chirp de fréquence : un chirp linéaire qui dépend uniquement de la dispersion et du gain, quelle que soit la forme de l'impulsion initiale. En considérant un guide d'ondes en Si_3N_4 de dimensions 700 × 700 nm, un gain de $g = 46\,\mathrm{m}^{-1}$ (équivalent à 2 dB/cm) est une valeur réalisable pour une plateforme intégrée. Ce gain peut être obtenu par intégration hétérogène avec des matériaux oxydés dopés à l'erbium ou au thulium. La largeur du guide d'ondes est fixée à 700 nm, lui permettant de présenter une GVD normale avec $\beta_2 = 700\,\mathrm{ps}^2/\mathrm{km}$, $\beta_3 = -1.44 \cdot 10^{-38}\,\mathrm{s}^3/\mathrm{m}$ à une longueur d'onde de 1550 nm et un coefficient non linéaire de $\gamma = 1\,\mathrm{W}^{-1}\mathrm{m}^{-1}$.

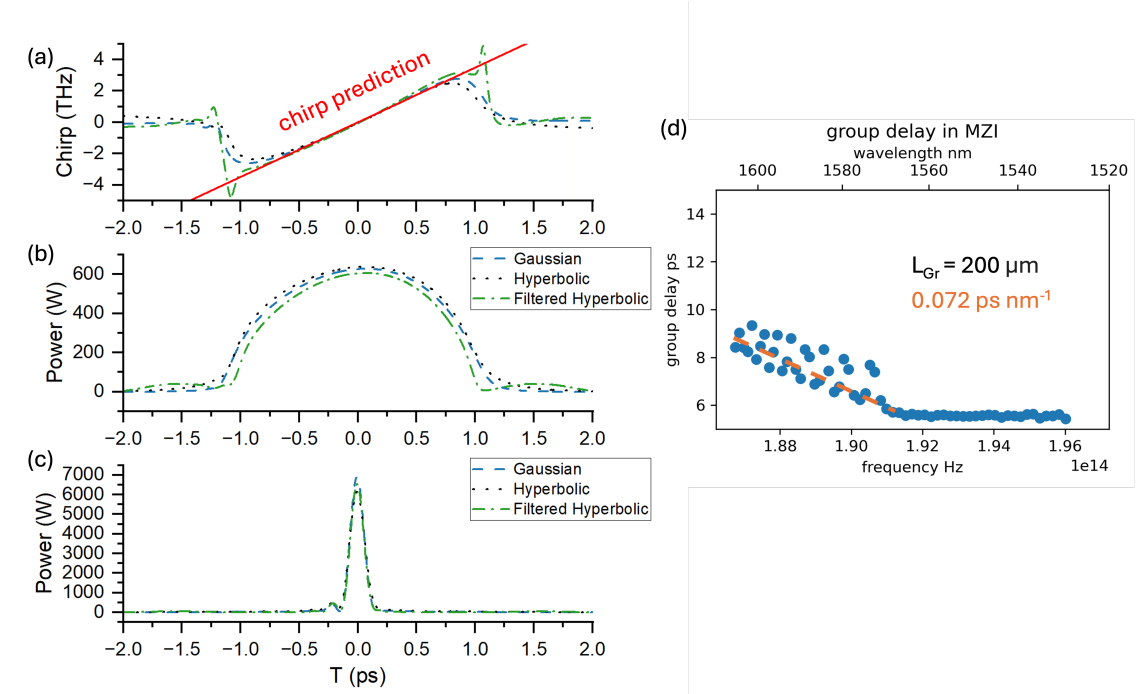

Fig. 1.9. (a,b,c) Pulses après 5 cm de propagation avec différentes formes d'impulsions initiales. Les résultats notés en bleu, noir et vert proviennent de formes d'impulsions initiales de Gaussienne, de secante hyperbolique et de secante hyperbolique filtrée, respectivement. (a) Chirp d'impulsion et la prédiction sont montrés en rouge. (b) Profil temporel de l'impulsion. (c) Profil temporel de l'impulsion après la même compensation de GVD anormale. **(d) Retard de groupe introduit par un compresseur d'impulsions.**

Dans la Figure 1.9(a,b), nous comparons les résultats de simulation de différentes formes d'impulsion initiales avec les mêmes paramètres, à savoir une puissance de crête initiale de 100 W et une durée d'impulsion de 1 ps. Bien qu'il y ait de légères différences dans les détails, trois formes d'impulsion initiales différentes présentent un résultat similaire en termes de chirp d'impulsion et de profil temporel d'impulsion, ce qui vérifie la caractéristique de la propagation auto-similaire. En appliquant un retard de groupe de 0.0716 ps/nm, les impulsions amplifiées sont comprimées temporellement (Figure 1.9(c)), dont le profil partage une puissance de crête similaire de 6 kW à 7 kW, indiquant qu'un facteur de compression similaire peut être atteint avec différentes formes d'impulsion initiales.
La durée d'impulsion T_{FWHM} est d'environ 150 fs après compression d'impulsion, ce qui correspond à une bande passante de 60 nm centrée à 1550 nm. En pratique, atteindre un réseau

qui introduit une dispersion anormale dans cette large plage est un défi. Par conséquent, un nouveau réseau conçu pour la compression de courtes impulsions sera introduit dans ce qui suit.
Pour réaliser la compression d'impulsions, un compresseur d'impulsions basé sur un réseau dispersif est nécessaire. Typiquement, un réseau dispersif fonctionne comme un dispositif réfléchissant. Il atteint une GVD substantielle qui dépasse la GVD du guide d'ondes jusqu'à trois ordres de grandeur. Cela est accompli en réfléchissant différentes longueurs d'onde à des positions spatiales distinctes à l'intérieur du réseau. Nous dissocions le compresseur d'impulsions en un réseau de Bragg asymétrique réfléchissant et en un coupleur directionnel modal. Les larges bandes passantes de ces deux composants garantissent la large bande passante de l'appareil. Une vue schématique du compresseur d'impulsions peut être trouvée dans la Figure 1.8.
La caractérisation du retard de groupe est réalisée par un interféromètre de Mach-Zehnder (MZI), dont un bras est remplacé par le compresseur. En effet, une large bande passante de travail est observée expérimentalement, couvrant de 1530 nm à 1600 nm (Figure 1.9(d)). La couverture de bande passante a le potentiel de comprimer l'impulsion à une durée de 150 fs. En utilisant le gradient du retard de groupe (la pente indépendamment de l'oscillation), les dispersions totales calculées sont notées en orange. En ce qui concerne la dispersion nécessaire pour la compression d'impulsion après propagation auto-similaire compte tenu des conditions, le meilleur choix de compresseur d'impulsions est celui avec une longueur de réseau de $200\,\mu\mathrm{m}$.

Conclusion

Ce manuscrit explore le développement d'une source de supercontinuum sur puce basée sur Si_3N_4. Une nouvelle ingénierie de la dispersion via le quasi-accord de phase permet un élargissement spectral amélioré avec plusieurs ondes dispersives. Pour améliorer encore la génération de supercontinuum, un schéma d'auto-compression d'impulsion est proposé, avec le potentiel de réduire la durée des impulsions à 150 fs sur une plateforme de guide d'ondes en Si_3N_4. Ces innovations offrent des perspectives prometteuses vers des systèmes intégrés de génération de supercontinuum entièrement sur puce.

2 - Introduction

Summary

The fast development of silicon photonics as a part of integrated photonics has been largely driven by the established silicon semiconductor industry, which has existed since the early 1980s. Due to its high refractive index, abundant quantity on Earth and mature fabrication inherited from semicondutor industry, silicon photonics enables the creation of high-functionality photonic devices with key advantages: low cost, low power consumption, and scalability. With applications spanning data communications, optical computing, sensing and imaging, the integration of silicon photonics is transforming how information is generated, processed, transmitted, and detected.

One of the main research topic is to the bring the light emission capability to silicon photonics. However, silicon has limitations as a photonic material for light emission. First, due to its indirect bandgap, which results in weak light emission efficiency. This characteristic limits silicon's capacity for efficient light generation, posing a significant challenge in photonic device design. A promising solution lies in hybrid integration, where new optical materials and structures are incorporated into silicon-based platforms. This approach has enabled the development of highly compact and efficient photonic components such as III-V lasers on silicon, optical amplifiers, and high-speed electro-optic (EO) modulators.

Another promising functionality to bring on silicon photonics is the nonlinear optics. Integrated silicon waveguide has a high optical mode confinement, high optical nonlinearity and a tailorable waveguide geometry, which are favorable for efficient nonlinear optics. The integrated optical waveguide is significantly smaller than fiber or bulk optical components. This reduction in size allows optical systems to shrink from table-sized setups to compact, finger-sized devices. Additionally, the smaller waveguide better confines light, enhancing light-matter interaction and thereby reducing the required power.

2.1 . Context of nonlinear optics

Nonlinear optics includes a broad spectrum of phenomena centered on intense light interacting with matters. Since the first demonstration of frequency conversion via second-harmonic generation in the early 1960s[1], nonlinear optics has attracted researchers, driving both fundamental research and the development of numerous applications.

One of the most crucial aspects of nonlinear optics, frequency conversion, gives birth to various light sources in different wavelength ranges and serves an important role both for modern industries and people's daily lives, including laser, detection, medical treatment, biology, telecommunications, and so on. For instance, Stimulated Raman Scattering (SRS) leads to Coherent Anti-Stokes Raman Spectroscopy (CARS), enabling the detection of nuclear vibrations in chemical bonds of the interest material. Third-harmonic generation has facilitated the development of femtosecond UV lasers used in eye surgery. Additionally, Raman fiber amplifiers provide an effective method for signal amplification in telecommunications without the need for ion-doping fiber.

With global warming at the forefront of concerns, there is a growing demand for power-efficient alternatives to current solutions. Simultaneously, the increasing trend toward portable devices calls for innovative, integrated, and lightweight nonlinear-based technologies that can be implemented in moving carriers like humans, cars, drones, and satellites. In this context, using integrated waveguides has attracted much attention.

In the need for a multi-wavelength light source, supercontinuum generation (SCG) has attracted much attention. SCG is a frequency conversion process where an intense laser pulse undergoes substantial spectral broadening. If the continuum maintains a good temporal coherence, it is also an optical frequency comb. The ability to reach wavelengths far from the pump with high spectral intensity enables diverse applications in imaging, metrology, and spectroscopy. The integrated optics offer unique advantages for SCG as it offers a flexible waveguide geometry and a high nonlinearity, which are two crucial aspects for an efficient SCG.

Many materials have been applied for on-chip SCG, including III-V materials like AlGaAs[2], lithium-niobate[3], [4], GaN[5], chalcogen material in [6]–[8], and inevitably, group IV materials (like silicon). A comprehensive review of different materials for on-chip SCG can be found in [9]. Silicon has garnered significant attention due to its high nonlinearity, well-established fabrication processes, and non-toxic characteristics.

Four commonly used Si-compatible materials and their properties are shown in Table.2.1. SiO_2 is usually used as the buried layer or upper cladding, and is not used for the waveguide core, thus it is out of consideration. For silicon, although it has a high nonlinear index n_2, indicating a high nonlinearity, its transparent window is limited from 1.1–9 μm, not covering the important visible and NIR range. Moreover, Si suffers from two-photon absorption (TPA) in a telecom waveguide of 1550 nm. In TPA, two photons are absorbed simultaneously, limiting the maximum pump power and increasing the risk of waveguide damage; thus, TPA is considered a nonlinear loss. Therefore, silicon is more suitable for SCG in the MIR. Germanium is another suitable material for MIR, with transparency windows extending up to 14 μm.

In particular, Si_3N_4 offers an exceptionally wide transparency window, spanning from 0.35 μm to 7 μm. Compared to Si, Si_3N_4 exhibits negligible two-photon absorption (TPA) in the near-infrared range, thereby minimizing nonlinear losses that typically restrict the shortest usable wavelength for the pump. Although Si_3N_4 has a moderate Kerr nonlinearity compared to Si and Ge, its ultra-low loss characteristic enables long propagation lengths to accumulate sufficient nonlinear effects. This makes it an excellent platform for exploring various novel nonlinear phenomena and positions it as a strong candidate for commercialization[10], [11].

Material	Transparency window (μm)	Bandgap E_g	n	n_2 (cm^2/W)
Si	1.1 - 9	1.12 eV	3.48	$\sim 6 \times 10^{-14}$
SiO_2	0.13 - 3.5	9 eV	1.46	$\sim 2.7 \times 10^{-16}$
Si_3N_4	0.35 - 7	5 eV	2	$\sim 2.4 \times 10^{-15}$
Ge	2 - 14	0.7 eV	4 (at 4 μm)	$\sim 0.5 - 1 \times 10^{-13}$ (in MIR)

Table 2.1. Properties of Si-compatible materials. Values of refractive index n and n_2 are at 1.55 μm unless stated otherwise. The transparency window is defined as the band where the absorption loss is below 2 dB/cm. This table is adapted from [9].

2.2 . State of the art

Significant advancements have been made in SCG within integrated Si_3N_4 and silicon (Si) waveguides. These breakthroughs include demonstrations of SCG spanning the visible, near-infrared (NIR), and mid-infrared (MIR) regions, opening up vast opportunities for various on-chip applications. A wide variety of waveguide designs have been developed to meet specific requirements for spectral broadening and coherence. Concurrently, considerable efforts have been made to adapt the pump conditions to match integrated laser sources, with the ultimate goal of achieving a fully integrated SCG system on-chip.
This chapter highlights key advancements in SCG based on Si and Si_3N_4 platforms. We first review the current state of spectral broadening and its relevant applications. Following that, we discuss various waveguide designs and the corresponding pumping conditions. In the context of pumping conditions, we emphasize the importance of two essential components for realizing fully integrated SCG systems: on-chip amplification and pulse compression. A detailed review of these components is also provided in this chapter.

2.2.1 . Spectral range and applications

Although supercontinuum generation in Si_3N_4 is typically pumped in the IR range because this is where most of the commercial pulse lasers can be found, its spectral broadening can be tailored to favor the NIR, MIR, and visible regions, providing crucial conditions for potential applications across these spectral ranges (Figure.2.1). Moreover, if SCG maintains good temporal coherence, it unlocks a broad range of applications that require an optical frequency comb.
In NIR, integrated SC sources are promising for compact and high-performance optical coherence tomography (OCT) systems (Figure.2.1(c)). Low-noise spectral broadening in Si_3N_4 waveguide has been realized to drive an OCT system in low power without compromising sensitivity[12]. A similar system can be applied to biology and medical applications. Another potential application is in telecommunication, serving as a wavelength division multiplexing (WDM) source. The coherent and high repetition rate SC source[13] covering the telecommunication wavelength can be a solution for the fast-growing traffic demand (Figure.2.1(d)).
The SC in the MIR range serves as an important source for spectroscopy (Figure.2.1(b)). Due to its broad transparent windows, Si_3N_4 allows the SC to extend beyond 3 μm[14], covering strong absorption lines from various vibrational modes, which provides an optical absorption fingerprint for many hydrocarbons, nitrogen dioxide, greenhouse gases, and specimens detectable in breath analysis[15]. Additionally, dual-comb spectroscopy has been demonstrated[16], obtaining performance equivalent to bulk MIR dual-comb system.
A strong energy conversion to the visible range is important for developing frequency metrology via frequency combs (Figure.2.1(a)). Many works have demonstrated self-referenced frequency

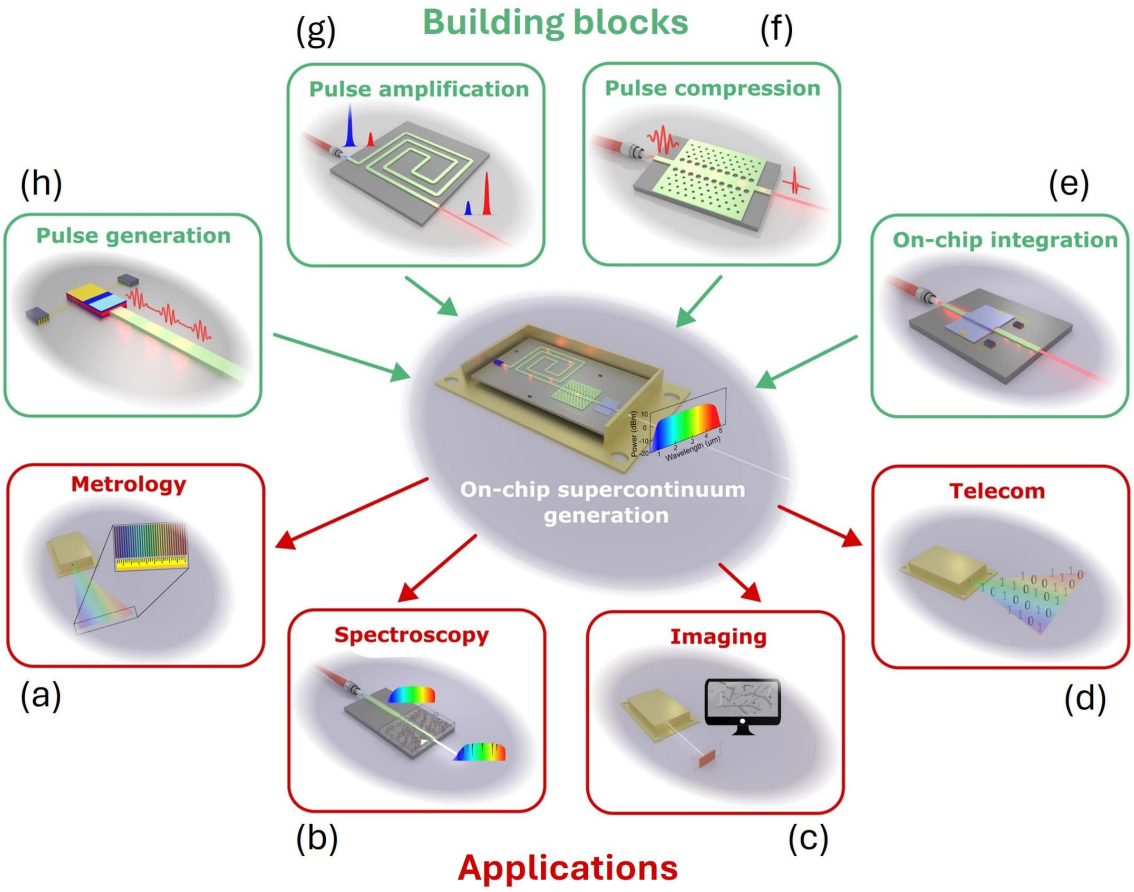

Fig. 2.1. Building block (up in green) and applications (down in red) for a fully integrated SC source. The figure is adapted from [9].

comb by overlapping the coherent broadened SC spectrum with the second or third harmonic generation (SHG, THG)[17]–[20]. The harmonic signal can be generated either from external crystal[18] or by the Si_3N_4 waveguide itself monolithically[19], [20]. Such configurations can be used to create ultra-stable RF frequencies or as a component of an optical atomic lock.

2.2.2 . Spectral broadening methodologies

One of the key advantages of supercontinuum generation (SCG) is the ability to tailor the spectrum to suit specific applications. We present in this section main results of spectral broadening in Si_3N_4/Si waveguides with their strategies, which is illustrated in Figure.2.2 and references and details are shown in Table.2.2.

SCG is influenced by the combined effects of optical nonlinearity and waveguide dispersion, which are dominated by material property and waveguide geometry, respectively. Since optical nonlinearity is generally constant over a wide wavelength range, spectral broadening is primarily designed by manipulating waveguide geometry, specifically by adjusting the waveguide width on an integrated platform, as the waveguide height is typically fixed. This is called dispersion engineering. The second order derivative of the waveguide guide dispersion, or known as group velocity dispersion (GVD parameter β_2), usually looks like a parabolic curve which can cross the zero (see more details in Chapter.3). According to β_2 is above of below zero, normal dispersion (ND) and anomalous dispersion (AD) are distinguished. Because spectral broaden-

ing dynamics are different when the pump locates in AD and ND, the state-of-the-art will be presented separately. Additionally, a waveguide can also have all its β_2 above zero, giving an all-normal-dispersion (ANDi) waveguide, which will be discussed later.

The most common way for on-chip SCG in put the pump in the AD of the waveguide (Figure.2.2(c-h)), where soliton dynamics plays a principle role (see details in Chapter.3). The most practical way is changing the width of a width-invariant waveguide to tune the preferable wavelength for energy transition. It also allows a very wide spectral broadening as an over two-octave broadening has been achieved (Figure.2.2(c)). A notched waveguide is also proposed to provide an extra degree of freedom of dispersion engineering[21] (Figure.2.2(d)). With this kind of waveguide with additional opening in the middle, a strengthen energy transition to the targeted MIR wavelength has been demonstrated.

More precise spectral broadening control can be realised by segmented waveguides which is composed of several waveguides with different widths or tapers. This is because they allow precise dispersion control in different spectral broadening stages. A waveguide composed of 7 sections is suggested in [22] to achieve a flatter spectrum by group-velocity matching (Figure.2.2(e)). Similar strategy has also been applied on a free-form waveguide, where the width variation with waveguide length is controlled by inverse design[23] (Figure.2.2(f)). Another segmented waveguide is proposed to obtain an ultra-efficient spectral broadening by alternating the dispersion sign so that the pulse peak power remains high through the propagation[24] in Figure.2.2(g).

Metamaterial waveguides [25] (Figure.2.2(h)) have also been utilized for dispersion engineering. The sub-wavelength periodic structure induces an effective material, where different wavelengths experience distinct refractive indices. This approach introduces additional design flexibility in tailoring the dispersion properties of the waveguide.

Demonstration has also been made when the pump locates in ND (Figure.2.2), where self-phase modulation and optical wave breaking are the main reason for the spectral broadening. In [26], a broad spectral broadening is created with very high temporal coherence due to the pump at 1300 nm locating at the ND of of a width-invariant waveguide.

An octave-spanning spectral broadening has also been demonstrated in an all-normal dispersion (ANDi) waveguide (Figure.2.2(a)). This width-invariant Si_3N_4 waveguide exhibits a dispersion profile that remains positive across the entire guided wavelength range. At the pump wavelength of 1560 nm, the group velocity dispersion (GVD) is nearly zero, helping to preserve the pump's peak power. Additionally, the resulting spectrum maintains excellent temporal coherence.

Recent developments in waveguide design for SCG show that most efforts are still focused on the AD regime, with emerging novel waveguide designs offering enhanced control over the generated spectrum. SCG pumped in the ND regime continues to rely on width-invariant waveguides.

Platform	Method	length	Pump (nm)	P_p^c (kW) & T_{FWHM} (fs)	Bandwidth (-30 dB)
Si_3N_4, (a), 2022 [13]	width-invariant	200 mm	1560 (ND)	6.5, 50	1-2 µm
Si_3N_4, (b), 2017 [26]	width-invariant	20 mm	1300 (ND)	1.3, 200	0.65-1.5 µm
Si_3N_4, (c), 2017 [27]	width-invariant	6 mm	1560 (AD)	11, 120	0.53-2.60 µm
Si, (d), 2018, [21]	notch	10 mm	3000 (AD)	1.2, 100	2.5-6.2 µm
Si. (e), 2020, [22]	7-segment (wave trapping)	3 mm	2260 (AD)	0.47, 70	1.25-2.6 µm
Si_3N_4, (f), 2024, [23]	inverse design	5.5 mm	1560 (AD)	9.5, 50	0.5-2.75 µm
Si_3N_4, (g), 2023, [24]	sign-alternating dispersion	94 mm	1554	0.3, 165	1.25-2.5 µm
Si, (h), 2022, [25]	metamaterial	4 mm	3500 (AD)	1, 220	1.5-7.8 µm

Table 2.2. Summary of the main SCG results obtained in silicon nitride and silicon waveguides. Results are also presented in Figure.2.2

.

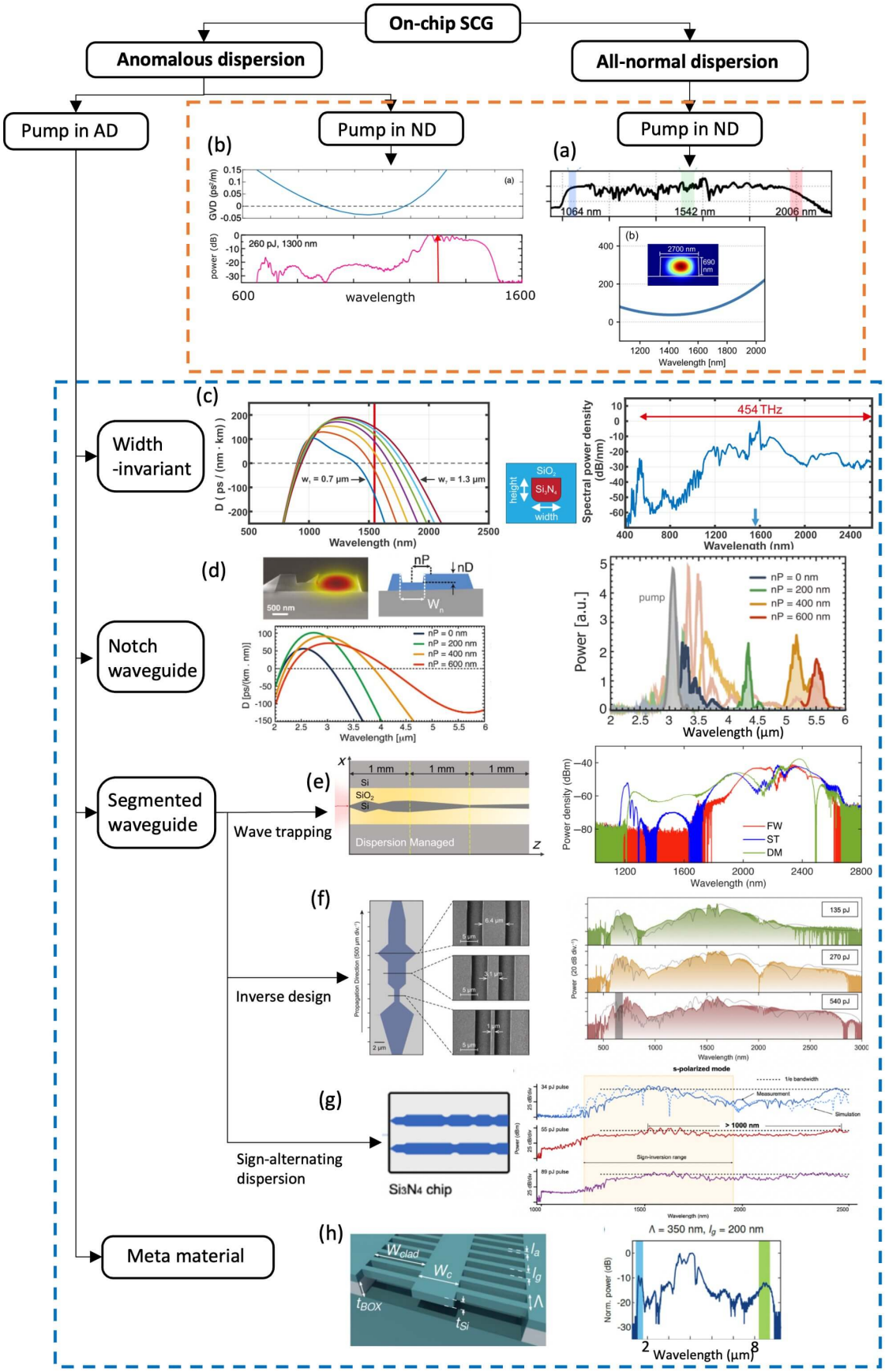

Fig. 2.2. Strategies of on-chip SCG in silicon photonics. Details can be found in Table.2.2

.

2.2.3 . Demand for pump laser source

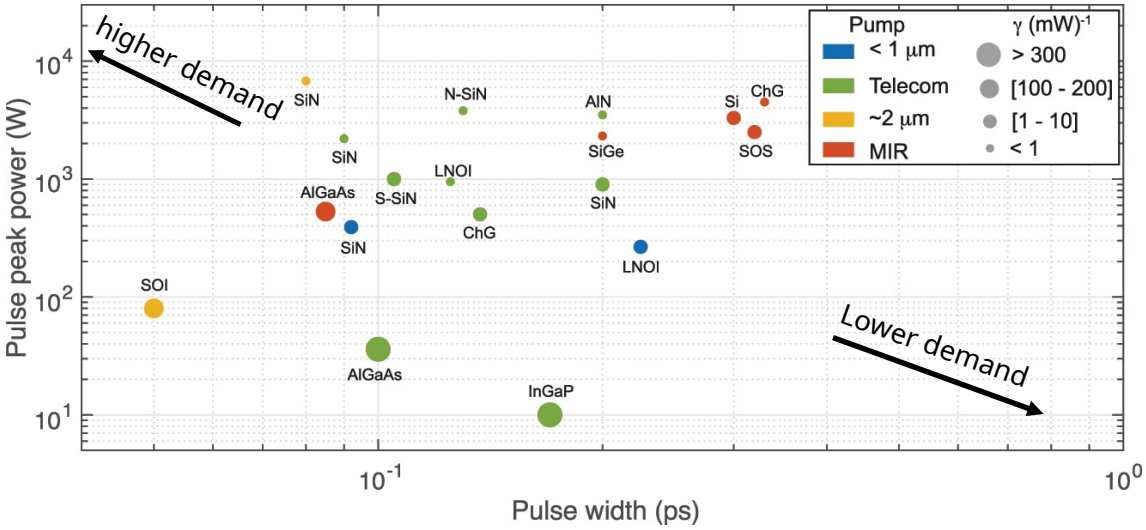

Fig. 2.3. Peak power and pulse width for various demonstrations of octave-spanning SC in chip-based platforms. The colors indicate the wavelength of the pump. The size of the marker indicates the magnitude of the nonlinear coefficient of the used platform. The figure is adapted from [9]

.

The initial pump laser pulse condition plays a vital role because SCG results from a delicate balance between optical nonlinearity and dispersion. Generally, a shorter pulse (sub-picosecond) is preferred because it helps maintain the low noise characterization during the spectral broadening. From Table.2.2, it can be found that for Si_3N_4 platform, an octave coherent spectral broadening requires sub-200 fs pulse width with a typical peak power of 1 kW pumped in anomalous dispersion. The pulse width can be relaxed to picosecond if an all-normal dispersion waveguide is used[13] but reaching an octave spanning still needs femtosecond pulses.
A general overview of the pump pulse requirements for various integrated platforms is illustrated in Figure.2.3, adapted from [9]. The x-axis represents the pulse width, while the y-axis represents the pulse peak power. A longer pulse width with lower peak power indicates less demanding pump conditions, placing it in the lower-right corner. Conversely, a shorter pulse width with higher peak power, located in the upper-left corner, indicates higher pump requirements. Notably, all demonstrated results so far involve pulse widths shorter than 400 fs, with a minimum peak power of at least 10 W. As a result, current research on on-chip supercontinuum generation still heavily relies on large, table-top ultra-short laser setups.

2.2.4 . On-chip amplification

In order to achieve a fully integrated compact octave SCG system, it is ideal to pump the waveguide with an integrated laser source. Integrated laser source in the recent study can now reach the pico or sub-picosecond regime either by electro-optic modulation[30], [31] or through mode-lock lasing[32]. However, their relative low peak power (around 1 W) is the main limitation for spectral broadening. These demands call for essential building blocks in integrated platforms: on-chip power amplification and pulse compression.
On-chip amplification is generally achieved through two methods: heterogeneous integration[33], where amplification occurs within III-V materials, and Er-doped waveguide amplifiers

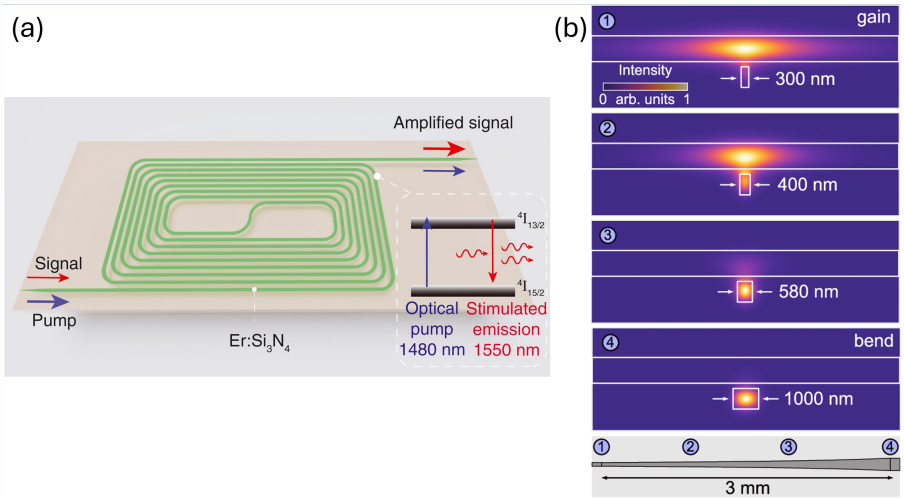

Fig. 2.4. Two ways to achieve high-gain on-chip amplification. (a) Integrated erbium-implanted Si_3N_4 waveguide amplifier. The figure is adapted from [28]. (b) Large mode area (LMA) waveguide. The figure is adapted from [29].

(EDWA)[34]–[36], where amplification is facilitated by doping the waveguides. Although EDWA is easier to integrate, the achievable output power is particularly challenging and limited because of the doping concentration. Efforts have been made to significantly enlarge the overlap between the embedded ion and the optical mode to realize high gain and high output power. One way is through wafer-scale ion implementation[28] (Figure.2.4(a)); the other way is using a large mode area (LMA) waveguide[37], [38], pushing the output continuous laser power to hundreds of mW till 1 W (Figure.2.4(b)). However, most of the current works are continuous wave amplification.

Recent advancements have demonstrated on-chip pulse amplification for femtosecond pulses, achieving over 50-fold amplification of 1 GHz-repetition-rate chirped femtosecond pulses in a CMOS-compatible photonic chip. Using a LMA waveguide, this device achieved a peak power of 800 W with a pulse duration of 116 fs. This breakthrough highlights the potential for future on-chip pulse amplification technologies.

2.2.5 . On-chip pulse compression

Table 2.3. Summary of the main on-chip pulse compression strategies and results. USRN: ultra-silicon-rich nitride. HOS: higher-order soliton. Fund. S: fundamental soliton. Bragg S: Bragg soliton. T_{FWHM}: full width half maximum of a pulse duration. P_0: peak power. F_c: compression factor. Q_c: compression quality. γ: nonlinear coefficient. The dispersion in (a) and (b) are from the Bragg grating used for pulse compression.

platform	method	input properties			output properties			Device properties		
		T_{FWHM}	P_0(W)	WL(nm)	T_{FWHM}	Fc	Qc	dispersion	γ($W^{-1}m^{-1}$)	length
Si, (a), 2010[39]	two stage	7ps	10	1550	1ps	7	0.26	-3300ps^2/m	300	6.5mm
USRN,(b),2021[40]	two stage	5.8ps	13.3	1550	0.55ps	11	0.85	-600ps^2/m	440	5.5mm
USRN, 2019[41]	HOS	2ps	7.2	1550	0.23ps	8.7	0.25~0.12	-170ps^2/km	440	7mm
Si3N4, 2019, [42]	HOS	60fs	3400	1560	12fs	5	0.4	-77ps^2/km	1	3mm
Si3N4,(c),2021[43]	HOS	1.2ps	21	1540	66fs	18	0.3~0.4	-79ps^2/km	1	40cm
Si, (d), 2017,[44]	fund. S	1ps	0.67	2490	57fs	17.5	0.91	-6~-0.3ps^2/km	30	51mm
USRN,(e),2019[45]	Bragg S	4.9ps	1.62	1543	0.86ps	5.7	unknown	-810 ps^2/m	440	6mm

As has been mentioned before, the on-chip laser sources have their limited pulse duration around 1 ps, not short enough for coherent SCG. There are two common ways to achieve

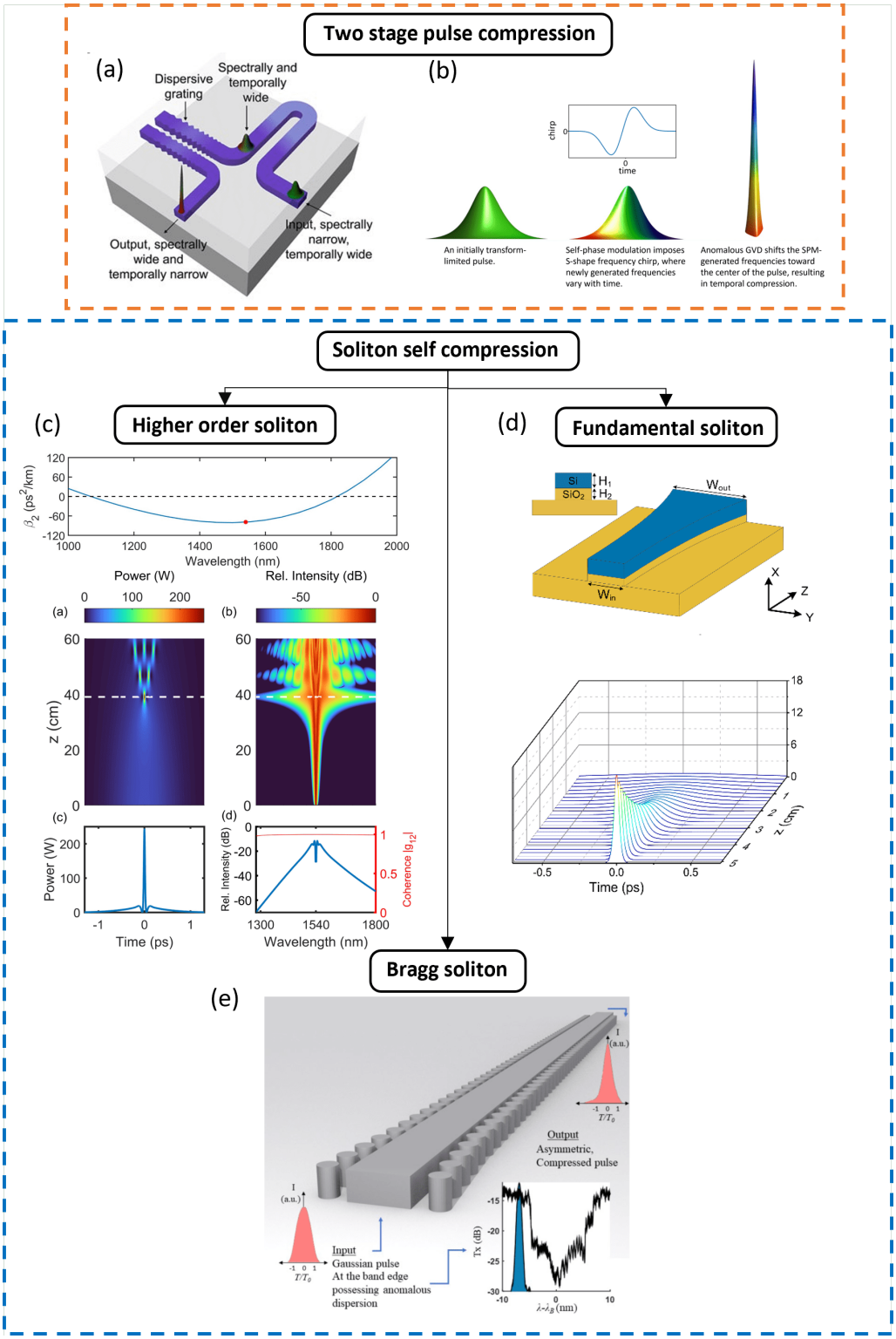

Fig. 2.5. On-chip pulse compression. (a,b) Schematic view of a two-stage pulse compression: SPM and a dispersive grating. (c) Pulse compression through higher-order soliton dynamics. (d) Pulse compression achieved by fundamental soliton evolution. (e) Pulse compression through a Bragg soliton. Details can be found in Table.2.3.

on-chip pulse compression: two stage pulse compression and soliton self compression. The illustrations of these two methods are shown in Figure.2.5, the details and references can be found in Table.2.3. The compression quality is evaluated by the compression factor F_c and quality factor Q_c. F_c is defined by the full width half maximum of the input pulse over the output. Q_c characterizes how much power remains in the main pulse after pulse compression, which is defined as:

$$Q_c = \frac{P_0^{\text{out}}}{P_0 \cdot F_c} \tag{2.1}$$

where P_0 and P_0^{out} are the peak power of the input and output pulse.
In a two stage pulse compression, the initial pulse is sent into a nonlinear waveguide (Figure.2.5(a, b)). The self phase modulation (SPM) broadens the spectrum and leads to a chirped pulse. Then, the pulse is sent to a dispersive grating with strong anomalous dispersion to compensate for the chirp introduced by SPM, thus resulting in a pulse compression. The SPM is usually efficient, since integrated waveguide usually obtains high optical Kerr nonlinearity. However, the realisation of on-chip dispersive grating is challenging. The efficient chip-scale integrated of this reflective device commonly requires a circulator [46], which remains a challenge nowadays in silicon phonics. In order to collect the reflected light, one existing solution is using a pair of coupled waveguide grating[47]. However, the bandwidth of dispersive grating limits the pulse compression. None of the grating can work on a large enough bandwidth that can support below 200 fs pulse compression. According to different grating structures, their bandwidths vary from a few nanometers to tens of nanometers, and the best result is a compression to 550 fs achieved in the bandwidth of 20 nm[40]. The compression quality can be good if the dispersive grating compensate perfectly the pulse chirp, with Q_c has reached to 0.85.
Another method to achieve on-chip pulse compression is to take advantage of soliton self compression (Figure.2.5(c,d,e)). The initial pulse is sent to the anomalous dispersion of the waveguide to form soliton. The soliton dynamic enables a single-stage pulse compression reaching the femtosecond level. The waveguide length needs to be carefully decided based on input pulse parameters, waveguide nonlinearity, and waveguide dispersion[41]–[43]. The higher order soliton offers definitely the highest compression factor (Figure.2.5(c), [43], $F_c = 18$). However, the temporal pulse shape is compromised due to the uncompensated nonlinear frequency chirp, giving a low $Q_c < 0.4$. Alternatively, simulation has also been studied to achieve pulse compression by fundamental soliton, offering a good compression factor and quality factor in the same time. The principle relies on controlling the waveguide dispersion variation along the propagation so that the pulse can be compressed through the adiabatic evolution of the fundamental soliton (Figure.2.5(d)). However, no experimental results have been demonstrated.
The Bragg soliton has also been employed for on-chip pulse compression (Figure.2.5(e)). A Bragg soliton forms when a pulse is launched in the strong dispersion region near the stop-band of a Bragg waveguide. Despite the strong dispersion, the pulse can still propagate while forming a soliton, known as the Bragg soliton. A compression factor F_c of 5.7 has been achieved while the quality factor was missed from characterization. The compressed pulse generated by the Bragg soliton has been reported to enhance supercontinuum broadening efficiency [48].
The summary of the main on-chip pulse compression strategies and results are shown in Table.2.3, the two stage pulse compression method has a good balance between compression factor F_c and quality factor Q_c while keeping the compact device footprint. However, the current work only focused on picosecond pulse compression to sub-picosecond pulse, which is not short enough for coherent SCG.

2.3 . Organization of the manuscript

During my thesis, I focused on optimizing every aspect of SCG within an integrated Si_3N_4 platform to create a highly customizable and power-efficient solution. My ultimate goal was to develop a flexible SCG with reduced pump power requirements, aligning with recent advancements in integrated mode-locked lasers, and to produce a spectrum suitable for various applications in the visible and NIR ranges. To address the progress, two main results will be presented and explained. First, a novel quasi-phase-matching condition will be add to the current dispersion engineering, bring huge flexibility to control the spectral broadening. Second, self-similar pulse compression is proposed to Si_3N_4 platform where the pulse is amplified and compressed. The aim is to relax the SCG demand for ultra-short, high-power pump pulse. This thesis manuscript is organized as follows:

- **Chapter.**3 introduces the dispersion and nonlinear effect essential for SCG. The spectral broadening of SCG when being pumped in different dispersion regions are also discussed.
- **Chapter.**4 presents two low-loss Si_3N_4 fabrications: in the foundry of our cooperator CEA LETI and the local clean room in C2N. The fabrication process, geometry, loss, dispersion are discussed and characterized.
- **Chapter.**5 introduces the SCG in a width-invariant waveguide. The experimental setup is presented, including key aspects such as coupling efficiency estimation and spectral broadening, which are crucial for accurate nonlinear characterization.
- **Chapter.**6 proposes a novel dispersion engineering method: the quasi-phase-matching method. It allows for customizable spectrum design tailored to specific applications. The underlying principles and design guidelines are discussed, along with the spectral broadening achieved under different dispersion conditions.
- **Chapter.**7 introduces the pulse compression method. It presents a potential method to bridge the gap between the pump pulse requirements for on-chip SCG and the mode-lock laser specifications enabled by recent advances. The approach consists of two parts: first, modeling self-similar propagation in integrated Si_3N_4 with amplification, discussing the necessary parameters; second, proposing a wideband pulse compressor design to achieve femtosecond pulse compression.
- **Chapter.**8. The manuscript end by a conclusion summarising the main results and the perspectives of this work at short and long terms.

References

[1] P. A. Franken, A. E. Hill, C. W. Peters, and G. Weinreich, "Generation of Optical Harmonics", en, *Physical Review Letters*, vol. 7, no. 4, pp. 118–119, 1961, ISSN: 0031-9007. DOI: 10.1103/PhysRevLett.7.118.

[2] B. Kuyken, M. Billet, F. Leo, K. Yvind, and M. Pu, "Octave-spanning coherent supercontinuum generation in an AlGaAs-on-insulator waveguide", en, *Optics Letters*, vol. 45, no. 3, p. 603, 2020, ISSN: 0146-9592, 1539-4794. DOI: 10.1364/OL.45.000603.

[3] M. Yu, B. Desiatov, Y. Okawachi, A. L. Gaeta, and M. Lončar, "Coherent two-octave-spanning supercontinuum generation in lithium-niobate waveguides", en, *Optics Letters*, vol. 44, no. 5, p. 1222, 2019, ISSN: 0146-9592, 1539-4794. DOI: 10.1364/OL.44.001222.

[4] J. Lu, J. B. Surya, X. Liu, Y. Xu, and H. X. Tang, "Octave-spanning supercontinuum generation in nanoscale lithium niobate waveguides", en, *Optics Letters*, vol. 44, no. 6, p. 1492, 2019, ISSN: 0146-9592, 1539-4794. DOI: 10.1364/OL.44.001492.

[5] W. Fan, M. Ludwig, I. Rousseau, *et al.*, "Supercontinua from integrated gallium nitride waveguides", en, *Optica*, vol. 11, no. 8, p. 1175, 2024, ISSN: 2334-2536. DOI: 10.1364/OPTICA.528341.

[6] M. R. Lamont, B. Luther-Davies, D.-Y. Choi, S. Madden, and B. J. Eggleton, "Supercontinuum generation in dispersion engineered highly nonlinear (= 10 /W/m) As_2s_3 chalcogenide planar waveguide", en, *Optics Express*, vol. 16, no. 19, p. 14 938, 2008, ISSN: 1094-4087. DOI: 10.1364/OE.16.014938.

[7] Q. Du, Z. Luo, H. Zhong, *et al.*, "Chip-scale broadband spectroscopic chemical sensing using an integrated supercontinuum source in a chalcogenide glass waveguide", en, *Photonics Research*, vol. 6, no. 6, p. 506, 2018, ISSN: 2327-9125. DOI: 10.1364/PRJ.6.000506.

[8] P. Wang, J. Huang, S. Xie, J. Troles, and P. St.J. Russell, "Broadband mid-infrared supercontinuum generation in dispersion-engineered As $_2$ S $_3$ -silica nanospike waveguides pumped by 2.8 m femtosecond laser", en, *Photonics Research*, vol. 9, no. 4, p. 630, 2021, ISSN: 2327-9125. DOI: 10.1364/PRJ.415339.

[9] C.-S. Brès, A. Della Torre, D. Grassani, V. Brasch, C. Grillet, and C. Monat, "Supercontinuum in integrated photonics: generation, applications, challenges, and perspectives", en, *Nanophotonics*, vol. 12, no. 7, pp. 1199–1244, 2023, ISSN: 2192-8614. DOI: 10.1515/nanoph-2022-0749.

[10] (), [Online]. Available: https://www.ligentec.com/.

[11] octave$_p$*hotonics*. (), [Online]. Available: https://www.octavephotonics.com/.

[12] X. Ji, D. Mojahed, Y. Okawachi, A. L. Gaeta, C. P. Hendon, and M. Lipson, "Millimeter-scale chip–based supercontinuum generation for optical coherence tomography", en, *Science Advances*, vol. 7, no. 38, eabg8869, 2021, ISSN: 2375-2548. DOI: 10.1126/sciadv.abg8869.

[13] I. Rebolledo-Salgado, Z. Ye, S. Christensen, *et al.*, "Coherent supercontinuum generation in all-normal dispersion Si $_3$ N $_4$ waveguides", en, *Optics Express*, vol. 30, no. 6, p. 8641, 2022, ISSN: 1094-4087. DOI: 10.1364/OE.450987.

[14] H. Guo, C. Herkommer, A. Billat, *et al.*, "Mid-infrared frequency comb via coherent dispersive wave generation in silicon nitride nanophotonic waveguides", en, *Nature Photonics*, vol. 12, no. 6, pp. 330–335, 2018, ISSN: 1749-4885, 1749-4893. DOI: 10.1038/s41566-018-0144-1.

[15] M. Vainio and L. Halonen, "Mid-infrared optical parametric oscillators and frequency combs for molecular spectroscopy", en, *Physical Chemistry Chemical Physics*, vol. 18, no. 6, pp. 4266–4294, 2016, ISSN: 1463-9076, 1463-9084. DOI: 10.1039/C5CP07052J.

[16] D. Grassani, E. Tagkoudi, H. Guo, *et al.*, "Mid infrared gas spectroscopy using efficient fiber laser driven photonic chip-based supercontinuum", en, *Nature Communications*, vol. 10, no. 1, p. 1553, 2019, ISSN: 2041-1723. DOI: 10.1038/s41467-019-09590-3.

[17] P. Manurkar, E. F. Perez, D. D. Hickstein, *et al.*, "Fully self-referenced frequency comb consuming 5 watts of electrical power", en, *OSA Continuum*, vol. 1, no. 1, p. 274, 2018, ISSN: 2578-7519. DOI: 10.1364/OSAC.1.000274.

[18] A. S. Mayer, A. Klenner, A. R. Johnson, *et al.*, "Frequency comb offset detection using supercontinuum generation in silicon nitride waveguides", en, *Optics Express*, vol. 23, no. 12, p. 15 440, 2015, ISSN: 1094-4087. DOI: 10.1364/OE.23.015440.

[19] D. R. Carlson, D. D. Hickstein, A. Lind, *et al.*, "Self-referenced frequency combs using high-efficiency silicon-nitride waveguides", en, *Optics Letters*, vol. 42, no. 12, p. 2314, 2017, ISSN: 0146-9592, 1539-4794. DOI: 10.1364/OL.42.002314.

[20] A. Ishizawa, K. Kawashima, R. Kou, *et al.*, "Direct f-3f self-referencing using an integrated silicon-nitride waveguide", en, *Optics Express*, vol. 30, no. 4, p. 5265, 2022, ISSN: 1094-4087. DOI: 10.1364/OE.449575.

[21] N. Nader, D. L. Maser, F. C. Cruz, *et al.*, "Versatile silicon-waveguide supercontinuum for coherent mid-infrared spectroscopy", en, *APL Photonics*, vol. 3, no. 3, p. 036 102, 2018, ISSN: 2378-0967. DOI: 10.1063/1.5006914.

[22] J. Wei, C. Ciret, M. Billet, F. Leo, B. Kuyken, and S.-P. Gorza, "Supercontinuum Generation Assisted by Wave Trapping in Dispersion-Managed Integrated Silicon Waveguides", en, *Physical Review Applied*, vol. 14, no. 5, p. 054 045, 2020, ISSN: 2331-7019. DOI: 10.1103/PhysRevApplied.14.054045.

[23] C.-Y. Lee, Y. Liu, Y. Cheng, C. Lao, and Q.-F. Yang, "Inverse design of coherent supercontinuum generation using free-form nanophotonic waveguides", en, *APL Photonics*, vol. 9, no. 6, p. 066 108, 2024, ISSN: 2378-0967. DOI: 10.1063/5.0196434.

[24] H. Zia, K. Ye, Y. Klaver, D. Marpaung, and K.-J. Boller, "Ultraefficient on-Chip Supercontinuum Generation from Sign-Alternating-Dispersion Waveguides", en, *Advanced Photonics Research*, p. 2 200 296, 2023, ISSN: 2699-9293, 2699-9293. DOI: 10.1002/adpr.202200296.

[25] T. T. D. Dinh, X. L. Roux, M. Montesinos-Ballester, *et al.*, *Dispersive wave control enabled by silicon metamaterial waveguides*, arXiv:2201.06516 [physics], 2022.

[26] Y. Okawachi, M. Yu, J. Cardenas, X. Ji, M. Lipson, and A. L. Gaeta, "Coherent, directional supercontinuum generation", en, *Optics Letters*, vol. 42, no. 21, p. 4466, 2017, ISSN: 0146-9592, 1539-4794. DOI: 10.1364/OL.42.004466.

[27] M. A. G. Porcel, F. Schepers, J. P. Epping, *et al.*, "Two-octave spanning supercontinuum generation in stoichiometric silicon nitride waveguides pumped at telecom wavelengths", en, *Optics Express*, vol. 25, no. 2, p. 1542, 2017, ISSN: 1094-4087. DOI: 10.1364/OE.25.001542.

[28] Y. Liu, Z. Qiu, X. Ji, *et al.*, "A photonic integrated circuit–based erbium-doped amplifier", en, *Science*, vol. 376, no. 6599, pp. 1309–1313, 2022, ISSN: 0036-8075, 1095-9203. DOI: 10.1126/science.abo2631.

[29] M. A. Gaafar, M. Ludwig, K. Wang, *et al.*, "Femtosecond pulse amplification on a chip", en, *Nature Communications*, vol. 15, no. 1, p. 8109, 2024, ISSN: 2041-1723. DOI: 10.1038/s41467-024-52057-3.

[30] M. Zhang, B. Buscaino, C. Wang, *et al.*, "Broadband electro-optic frequency comb generation in a lithium niobate microring resonator", en, *Nature*, vol. 568, no. 7752, pp. 373–377, 2019, ISSN: 0028-0836, 1476-4687. DOI: 10.1038/s41586-019-1008-7.

[31] Y. Hu, M. Yu, B. Buscaino, *et al.*, "High-efficiency and broadband on-chip electro-optic frequency comb generators", en, *Nature Photonics*, vol. 16, no. 10, pp. 679–685, 2022, ISSN: 1749-4885, 1749-4893. DOI: 10.1038/s41566-022-01059-y.

[32] A. Hermans, K. Van Gasse, J. Ø. Kjellman, *et al.*, "High-pulse-energy III-V-on-silicon-nitride mode-locked laser", en, *APL Photonics*, vol. 6, no. 9, p. 096 102, 2021, ISSN: 2378-0967. DOI: 10.1063/5.0058022.

[33] K. Van Gasse, R. Wang, and G. Roelkens, "27 dB gain III–V-on-silicon semiconductor optical amplifier with > 17 dBm output power", en, *Optics Express*, vol. 27, no. 1, p. 293, 2019, ISSN: 1094-4087. DOI: 10.1364/OE.27.000293.

[34] J. Rönn, W. Zhang, A. Autere, *et al.*, "Ultra-high on-chip optical gain in erbium-based hybrid slot waveguides", en, *Nature Communications*, vol. 10, no. 1, p. 432, 2019, ISSN: 2041-1723. DOI: 10.1038/s41467-019-08369-w.

[35] J. Rönn, J. Zhang, W. Zhang, *et al.*, "Erbium-doped hybrid waveguide amplifiers with net optical gain on a fully industrial 300 mm silicon nitride photonic platform", en, *Optics Express*, vol. 28, no. 19, p. 27 919, 2020, ISSN: 1094-4087. DOI: 10.1364/OE.399257.

[36] J. Mu, M. Dijkstra, J. Korterik, H. Offerhaus, and S. M. García-Blanco, "High-gain waveguide amplifiers in Si $_3$ N $_4$ technology via double-layer monolithic integration", en, *Photonics Research*, vol. 8, no. 10, p. 1634, 2020, ISSN: 2327-9125. DOI: 10.1364/PRJ.401055.

[37] N. Singh, J. Lorenzen, M. Sinobad, *et al.*, "Silicon photonics-based high-energy passively Q-switched laser", en, *Nature Photonics*, vol. 18, no. 5, pp. 485–491, 2024, ISSN: 1749-4885, 1749-4893. DOI: 10.1038/s41566-024-01388-0.

[38] N. Singh, J. Lorenzen, M. Sinobad, *et al.*, "Watt-Class CMOS-Compatible Power Amplifier", en, in *2023 Conference on Lasers and Electro-Optics Europe & European Quantum Electronics Conference (CLEO/Europe-EQEC)*, Munich, Germany: IEEE, 2023, pp. 1–1, ISBN: 9798350345995. DOI: 10.1109/CLEO/Europe-EQEC57999.2023.10231735.

[39] D. T. Tan, P. C. Sun, and Y. Fainman, "Monolithic nonlinear pulse compressor on a silicon chip", en, *Nature Communications*, vol. 1, no. 1, p. 116, 2010, ISSN: 2041-1723. DOI: 10.1038/ncomms1113.

[40] J. W. Choi, E. Sahin, B.-U. Sohn, *et al.*, "High spectro-temporal compression on a nonlinear CMOS-chip", en, *Light: Science & Applications*, vol. 10, no. 1, p. 130, 2021, ISSN: 2047-7538. DOI: 10.1038/s41377-021-00572-z.

[41] J. W. Choi, B.-U. Sohn, G. F. R. Chen, D. K. T. Ng, and D. T. H. Tan, "Soliton-effect optical pulse compression in CMOS-compatible ultra-silicon-rich nitride waveguides", en, *APL Photonics*, vol. 4, no. 11, p. 110 804, 2019, ISSN: 2378-0967. DOI: 10.1063/1.5113758.

[42] D. R. Carlson, P. Hutchison, D. D. Hickstein, and S. B. Papp, "Generating few-cycle pulses with integrated nonlinear photonics", en, *Optics Express*, vol. 27, no. 26, p. 37 374, 2019, ISSN: 1094-4087. DOI: 10.1364/OE.27.037374.

[43] R. Oliver, Y. Okawachi, X. Ji, *et al.*, "Soliton-effect compression of picosecond pulses on a photonic chip", en, *Optics Letters*, vol. 46, no. 18, p. 4706, 2021, ISSN: 0146-9592, 1539-4794. DOI: 10.1364/OL.436016.

[44] J. Yuan, J. Chen, F. Li, *et al.*, "Mid-infrared self-similar compression of picosecond pulse in an inversely tapered silicon ridge waveguide", en, *Optics Express*, vol. 25, no. 26, p. 33 439, 2017, ISSN: 1094-4087. DOI: 10.1364/OE.25.033439.

[45] E. Sahin, A. Blanco-Redondo, P. Xing, *et al.*, "Bragg Soliton Compression and Fission on CMOS-Compatible Ultra-Silicon-Rich Nitride", en, *Laser & Photonics Reviews*, vol. 13, no. 8, p. 1 900 114, 2019, ISSN: 1863-8880, 1863-8899. DOI: 10.1002/lpor.201900114.

[46] K. O. Hill, F. Bilodeau, B. Malo, *et al.*, "Chirped in-fiber Bragg gratings for compensation of optical-fiber dispersion", *Opt. Lett.*, vol. 19, no. 17, pp. 1314–1316, 1994, Publisher: Optica Publishing Group. DOI: 10.1364/OL.19.001314.

[47] D. T. H. Tan, K. Ikeda, and Y. Fainman, "Coupled chirped vertical gratings for on-chip group velocity dispersion engineering", en, *Applied Physics Letters*, vol. 95, no. 14, p. 141 109, 2009, ISSN: 0003-6951, 1077-3118. DOI: 10.1063/1.3242028.

[48] E. Sahin, A. Blanco-Redondo, B.-U. Sohn, *et al.*, "Wideband Spectral Enhancement through On-Chip Bragg-Soliton Dynamics", en, *Advanced Photonics Research*, vol. 2, no. 8, p. 2 100 107, 2021, ISSN: 2699-9293, 2699-9293. DOI: 10.1002/adpr.202100107.

3 - Principle of supercontinuum generation

Summary

We consider an optical pulse propagates in z direction, the electric field $\mathbf{E}$, with a transverse profile $\mathbf{F}(x, y)$ and a temporal envelope $A(z, t)$, is expressed as:

$$\mathbf{E}(x, y, z, t) = Re[A(z, t)\mathbf{F}(x, y) \exp(-i\omega_0 t + i\beta z)] \tag{3.1}$$

ω_0 is the carrier frequency. β is the propagation constant which can be expressed by wavelength λ_0 and refractive index n as $\beta = \frac{2\pi}{\lambda_0} \cdot n$. $\mathbf{F}(x, y)$ represents transverse optical mode. The temporal intensity $I = |A(z, t)|^2$.

3.1 . Self-phase modulation from the optical Kerr effect

3.1.1 . General principle

The optical nonlinearity of a material can be presented as its instantaneous nonlinear polarization $\mathbf{P_{NL}}$ depends on the quadratic and cubic response to the incident electric field E, which is written as:

$$\mathbf{P_{NL}} = \epsilon_0 \left(\chi^{(2)} : \mathbf{EE} + \chi^{(3)} \vdots \mathbf{EEE} \right) \tag{3.2}$$

ϵ_0 is the vacuum permittivity. $\chi^{(2)}$ and $\chi^{(3)}$ are the material's second and third-order susceptibility, respectively. Second-order nonlinearity is responsible for nonlinear effects such as second-harmonic generation and sum-frequency generation. Nevertheless, it exists only in materials that don't obtain an inversion symmetry like lithium niobate ($LiNbO_3$). For most materials that are compatible with silicon technology, like silicon (Si), silicon nitride (Si_3N_4), and germanium (Ge), their centro-symmetry, therefore, only exhibits third-order nonlinearity, known as the optical Kerr effect.

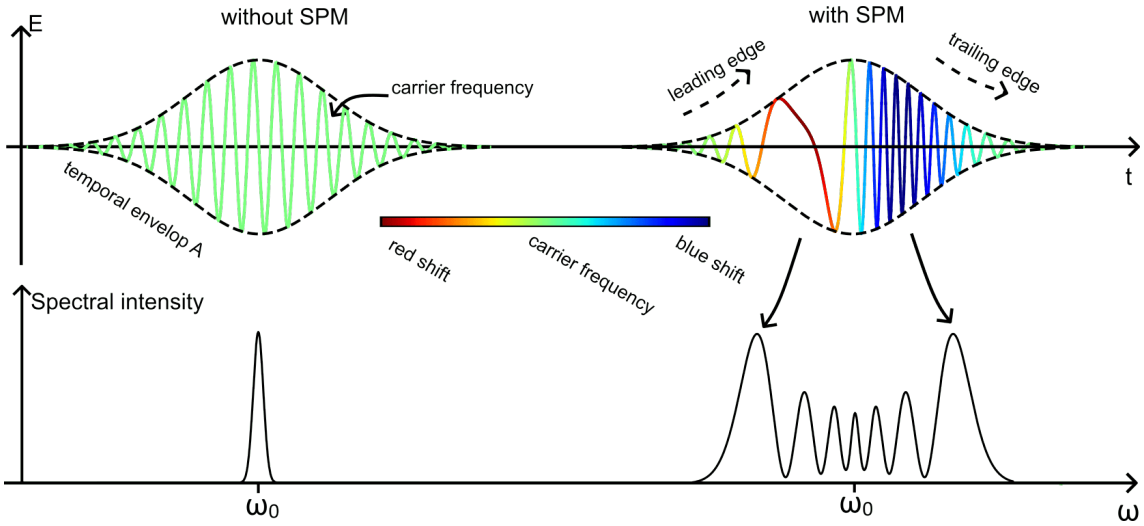

Fig. 3.1. Schematic illustration of self-phase modulation effect on a pulse. The optical field, both without and with SPM, is depicted at the top, accompanied by their corresponding spectral intensity at the bottom. The instantaneous frequency is indicated by color, where green denotes no chirp and red and blue signify negative and positive chirp, respectively.

Among all the different nonlinear effects resulting from the optical Kerr effects, like third-harmonic generation and four-wave mixing, the most important phenomenon that contributes to SCG is self-phase modulation (SPM). SPM comes from the nonlinear contribution to the refractive index. The refractive index n can be written as:

$$n(\omega, I) = n_0(\omega) + n_2 I \tag{3.3}$$

where n_0 is the linear refractive index, I is the optical intensity, and n_2 is the nonlinear index. n_2 is directly related to $\chi^{(3)}$ and is an intrinsic value for each material. For example, n_{2,Si_3N_4} equals to $2.4 \times 10^{-19}\,\mathrm{m}^2/\mathrm{W}$. With Equation 3.3, the temporal electric field E is rewritten as follows, ignoring transverse profile $\mathbf{F}(x, y)$:

$$E(z,t) = Re[A(z,t)\exp\left(-i\omega_0 t + i\beta_0 z + n_2 I(t)\beta_0 z\right)] \tag{3.4}$$

where the propagation constant $\beta_0 = \frac{2\pi}{\lambda_0} \cdot n_0$. The extra intensity-dependent nonlinear phase shift after a propagation z is written as:

$$\phi_{NL} = n_2 I(t)\beta_0 z \tag{3.5}$$

A schematic interpretation of SPM is shown in Figure.3.1, where the field E and the corresponding spectral intensity of a pulse at a given distance z is shown without and with SPM. On the left, a field without the optical Kerr effect ($n_2 = 0$) is shown as the temporal envelope A on a carrier frequency ω_0, while the field with SPM ($n_2 > 0$) is presented on the right. Due to the time-dependent nonlinear phase ϕ_{NL}, the instantaneous frequency undergoes a red and blue shift compared to the carrier frequency, thus generating new frequency components. The instantaneous frequency shift from carrier frequency ω_0 is called the frequency chirp $\delta\omega$ defined by the derivative of additional time-dependent phase $\phi(z,t)$ over time t:

$$\delta\omega(z,t) = -\frac{d\phi(z,t)}{dt} \tag{3.6}$$

Here, $\phi(z,t) = \phi_{NL}$. The minus sign is due to the choice of $exp(-i\omega_0 t)$ in Equation.3.1. When $\delta\omega$ grows with time t, it is called frequency up chirp, meaning that the instantaneous frequency grows with time. Conversely, it is called frequency down chirp. When $n_2 > 0$ (which is usually the case), SPM introduced a frequency up chirp from leading edge to trailing edge while the temporal envelope's shape is untouched. In the frequency domain, new frequencies are generated symmetrically as side lobes around the center frequency of the pulse ω_0 (Figure.3.1 at the bottom)).
SPM serves as an important role to soliton formation and dispersive wave generation, both of which are fundamental mechanisms in frequency conversion processes within SCG. Furthermore, when a non-chirped pulse undergoes SPM, it becomes chirped, leading to significant spectral broadening with out-of-phase frequency components. By realigning these frequency components using a dispersive grating, the pulse can be compressed, which is the fundamental principle behind two-stage pulse compression.

3.1.2 . Self-phase modulation in an integrated Si_3N_4 waveguide

For a guided mode of which its effective index is n_{eff}, the nonlinear coefficient γ is more commonly used to describe the nonlinearity. It can be written in terms of the nonlinear refractive index n_2 as:

$$\gamma = \omega_0 n_2/(cA_{eff}) \tag{3.7}$$

where c is the speed of light, and A_{eff} is the mode effective area defined by transverse profile $\mathbf{F}(x,y)$ in Equation.3.1 as:

$$A_{eff} = \frac{\iint_{-\infty}^{\infty} |\mathbf{F}(x,y)|^4 dxdy}{(\iint_{-\infty}^{\infty} |\mathbf{F}(x,y)|^2 dxdy)^2} \tag{3.8}$$

By using the nonlinear coefficient γ, a characteristic length of SPM can be defined by

$$L_{NL} = 1/(\gamma P_0) \tag{3.9}$$

This pertains to the distance over which a pulse with an input peak power P_0 accumulates a nonlinear phase shift of 1 radian in a waveguide possessing a nonlinear coefficient γ. To give an idea, for a Si_3N_4 waveguide, L_{NL} is of millimeter magnitude given $\gamma = 1\,\mathrm{W}^{-1}\mathrm{m}^{-1}$ and P_0 varying from hundreds Watts to kilowatts as typical values.
An example of SPM simulated in a 5-cm long Si_3N_4 waveguide is shown in Figure.3.2. The initial pulse has a squared hyperbolic secant ($sech^2$) shape, which is a typical pulse shape in a mode lock laser. The temporal envelope $A(t, z = 0)$ of the pulse can be expressed by peak power P_0 and T_0 shown in Equation.3.10.

$$A(t, z = 0) = \sqrt{P_0 \cdot sech^2(t/T_0)} \tag{3.10}$$

where $T_0 = T_{FWHM}/1.76$. The input pulse is set to have $T_{FWHM} = 190\,\mathrm{fs}$ and $P_0 = 200\,\mathrm{W}$. In Figure.3.2(a), SPM introduces a frequency up-chirp around the temporal center of the pulse, which means the instantaneous frequency increases from the leading to the trailing edge, while a frequency down-chirp at the edge. The total frequency chirp shape is not linear for the whole duration of the pulse. Instead, it presents a S shape. The initial spectrum is shown in black in Figure.3.2(b), while the broadening spectrum due to the SPM is shown in blue. The temporal and spectral evolution of the pulse within the 5-cm long waveguide is also simulated and shown in Figure 3.3. The simulation confirms that while SPM does not alter the temporal shape of

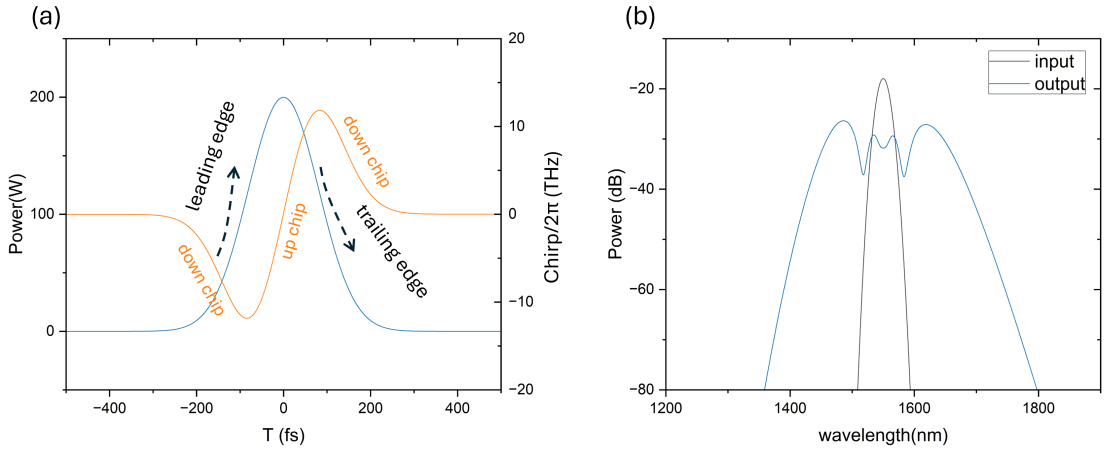

Fig. 3.2. The effect of self-phase modulation on a pulse in the temporal and spectral domain. The waveguide is 5 cm long with a nonlinear coefficient$\gamma = 1\,\mathrm{W/m}$. The input pulse is a hyperbolic secant pulse with a full width at half maximum (FWHM) of 190 fs and a peak power of 200 W. Dispersion effects are not considered in this scenario. (a) The pulse shape in blue and chirp in orange. (b) The initial and braodened spectrum is shown in black and blue.

the pulse, it continuously induces spectral broadening. The simulation details will be explained in Section.3.3.

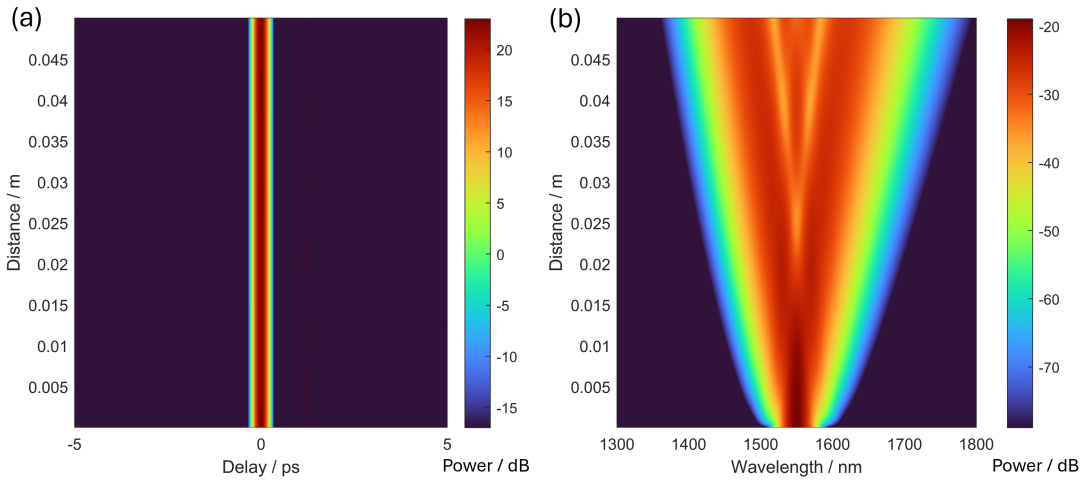

Fig. 3.3. The influence of SPM on the evolution of pulse temporal profile and spectrum. The conditions are the same as Figure.3.2. (a) The temporal evolution through propagation distance indicates an invariant temporal pulse. (b) The spectrum evolution through propagation distance indicates a continued spectrum broadening.

3.2 . Group velocity dispersion

3.2.1 . General principle

We represent here the electric field $\mathbf{E}$ which propagates in z direction shown in Equation.3.1:

$$\mathbf{E}(x, y, z, t) = Re[A(z, t)\mathbf{F}(x, y) \exp(-i\omega_0 t + i\beta z)] \tag{3.11}$$

Considering the non-monochromatic nature of the pulse, it is necessary to consider the frequency-dependent response of the propagation constant β, also called dispersion. $\beta(\omega)$ can be expressed as the Taylor expansion around the center frequency ω_0:

$$\beta(\omega_0) = \sum_{n=0}^{\infty} \frac{\beta_n}{n!}(\omega - \omega_0)^n \tag{3.12}$$

where

$$\beta_n = (\frac{d^n \beta}{d\omega^n}|_{\omega=\omega_0}) \tag{3.13}$$

Various physical interpretations can be ascribed to β_n. Specifically, β_0 is the wave number at the center frequency ω_0, while β_1 signifies the group velocity n_g, such that

$$v_g = 1/\beta_1 \tag{3.14}$$

In a frame of reference moving with the pulse at the v_g, both β_0 and β_1 are disregarded. The group velocity dispersion (GVD) expressed in β_2 is the waveguide dispersion that begins to have a real effect during pulse propagation. Regarding the sign, GVD can be anomalous, where $\beta_2 < 0$, and normal, where $\beta_2 > 0$, respectively. The wavelength where $\beta_2 = 0$ is called zero dispersion wavelength (ZDW). For a typical integrated waveguide, it is usually as a two ZDW system. However, in fiber optics, it is only considered as a one ZDW system because the second ZDW is located too far away from a reachable wavelength of visible and IR spectrum. It has to be noticed that the dispersion parameter D is also often used in literature defined as

$$D = -\frac{\omega_0^2 \beta_2}{2\pi c} \tag{3.15}$$

However, the sign of D in normal and anomalous GVD is opposite to that of β_2. In normal GVD, higher frequency components travel slower than lower ones. In anomalous GVD, higher frequency components travel faster than lower ones. For the orders $n > 2$ (as β_3, β_4, β_5, ...), they are called higher order dispersion (HOD), playing an important role in energy conversion preference in SCG which is later explained in Section.3.4.2.

For a non-chirped pulse (a Fourier transfer limit pulse of which all the frequencies are in-phase), the existence of GVD chirps the pulse. A schematic illustration is presented in Figure 3.4. The electric field $E(t)$ of a pulse with a Gaussian-shaped envelope and peak power P_0 is depicted on the left, where $\beta_2 = 0$. The Gaussian envelope follows the form described in Equation 3.16.

$$A = \sqrt{P(t)} = \sqrt{P_0 \cdot 2^{-(2t/T_{FWHM})^2}} \tag{3.16}$$

When given an anomalous GVD ($\beta_2 < 0$), the initial pulse is stretched in the temporal domain as shown on the right of Figure.3.4. The different frequency components in the initial pulse travel at different group velocities, where the blue component is faster than the red component. The instantaneous frequency thus undergoes a frequency down chirp from the leading edge to

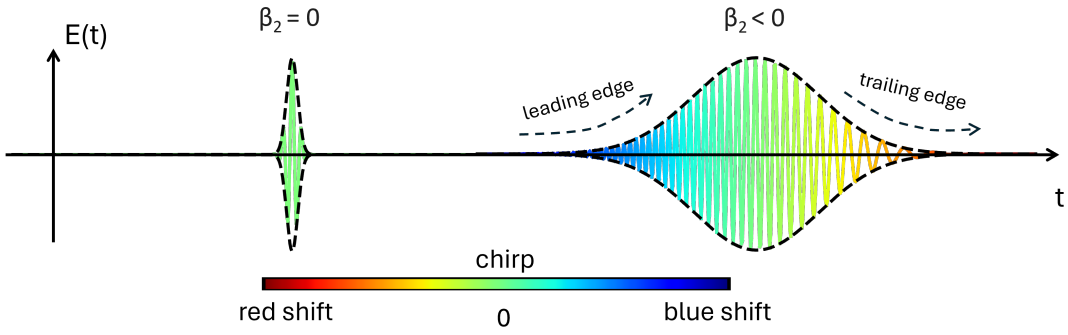

Fig. 3.4. Schematic illustration of group velocity dispersion effect on a pulse. The field of the initial Gaussian shape pulse is shown on the left, while the field considering GVD ($\beta_2 < 0$) is shown on the right. The instantaneous frequency is indicated by color, where green denotes no chirp and red and blue signify negative and positive chirp, respectively.

the trailing edge, which means the instantaneous frequency decreases with time. For a pulse prechirped by SPM (thus up-chirped pulse, see Figure.3.1 and Figure.3.2), the anomalous GVD can compensate for the frequency chirp and realign the phase of newly generated frequency components, resulting in a pulse compression.

The characteristic length of GVD is defined by the following expression $L_D = \frac{T_0^2}{|\beta_2|}$. It corresponds to the propagation length when the dispersive effects become important for a pulse duration of T_0. T_0 is related to T_{FWHM} depending on the different pulse shape. For the squared hyperbolic secant (sech^2) pulse shape shown in Equation.3.10, T_0 equals to $T_{FWHM}/1.76$. In the case of a Gaussian pulse expressed as in Equation.3.16, T_0 is equal to T_{FWHM}. For a typical Si_3N_4 waveguide, whose $\beta_2 \approx 100\,\mathrm{ps}^2/\mathrm{km}$, pumped by a T_0 = 100 fs pulse laser, L_D is in millimeter to centimeter scale.

3.2.2 . An example in a Si_3N_4 waveguide

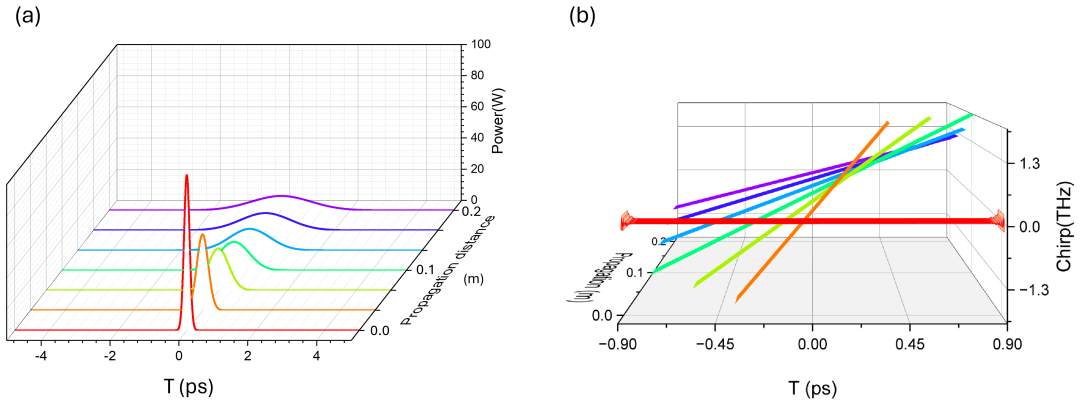

Fig. 3.5. The influence of group velocity dispersion (GVD) on a non-chirped temporal Gaussian shape pulse through 20 cm propagation. Initial pulse duration $T_0 = 100\,\mathrm{fs}$. Normal GVD is $\beta_2 = 700\,\mathrm{ps}^2/\mathrm{km}$ (a) GVD induces a temporal broadening. (b) The non-chirped pulse becomes linear chirped through propagation.

A $T_0 = 100\,\mathrm{fs}$ Gaussian shape pulse is sent to a 20-cm long Si_3N_4 waveguide, of which GVD is given as $\beta_2 = 700\,\mathrm{ps}^2/\mathrm{km}$. No nonlinear effect is considered, so the pulse evolution only

reflects the GVD effect. In Figure.3.5(a), a temporal broadening can be observed as the GVD effect accumulates through propagation. The chirp during the propagation of the pulse is shown in Figure.3.5(b). Starting with zero chirp, the chirp remains linear throughout propagation due to the initial Gaussian pulse shape [1]. The pulse experiences an up-chirp in frequency caused by normal GVD, with the slope of the chirp initially increasing and then decreasing.

3.3 . Nonlinear Schrödinger Equation

Although SPM and GVD are the two most important factors that influence SCG, to have an accurate nonlinear simulation for SCG, a general description of nonlinear process has to be taken into account, including nonlinear coefficient γ, dispersion β_k of all the orders and loss/gain α. The equation is called the Generalised Nonlinear Schrödinger Equation (GNLSE), which is expressed as:

$$\begin{aligned}\frac{\partial A}{\partial z} = &-\frac{\alpha}{2}A + i\sum_{k\geq 2}\beta_k\frac{i^k}{k!}\frac{\partial^k A}{\partial T^k} \\ &+ i\gamma\left(1 + i\tau_{\text{shock}}\frac{\partial}{\partial T}\right)\left[(1-f_r)\left|A\right|^2 A\right] \\ &+ f_r A\int_0^\infty h_r\left(T'\right)\left|A\left(z, T-T'\right)\right|^2 dT'.\end{aligned} \tag{3.17}$$

The first line introduces the linear effect: loss (α in m^{-1}) and dispersion. An accurate simulation requires dispersion parameters from β_2 to HOD. The dispersion operator $\hat{D} = \sum_{k\geq 2}\beta_k\frac{i^k}{k!}\frac{\partial^k}{\partial T^k}$ can be substituted by:

$$\hat{D} = \beta(\omega) - \beta_1(\omega - \omega_0) - \beta_0(\omega) \tag{3.18}$$

In this way, β_2 and all the HODs are considered, giving the most accurate simulation[2].
The second line introduces nonlinear coefficient γ defined by Equation.3.7, giving rise to SPM and another nonlinear effect like degenerated four-wave mixing. The frequency dependence of γ to a first-order extent is characterized by the time constant τ_{shock}, which is presented in Equation.3.19 as:

$$\tau_{shock} = \frac{1}{\omega_0} - \frac{1}{n_{eff}(\omega_0)}\cdot\frac{\partial n_{eff}}{\partial\omega}(\omega_0) - \frac{1}{A_{eff}(\omega_0)}\cdot\frac{\partial A_{eff}}{\partial\omega}(\omega_0) + \frac{1}{n_2(\omega_0)}\cdot\frac{\partial n_2}{\partial\omega}(\omega_0) \tag{3.19}$$

Usually, n_2 of the waveguide material is insensitive to frequency, so the last term of Equation.3.19 equals zero.
In the third line, the integral term corresponds to the delayed nonlinear response attributed to the Raman effect, which is modeled by its temporal response $h_r(t)$ and its fractional contribution f_r. For SCG in Si_3N_4, the Raman effect is negligible.
In conclusion, Equation.3.17 is simplified to NLSE as:

$$\frac{\partial A}{\partial z} = -\frac{\alpha}{2}A + i\sum_{k\geq 2}\beta_k\frac{i^k}{k!}\frac{\partial^k A}{\partial t^k} + i\gamma\left(1 + i\tau_{shock}\frac{\partial}{\partial t}\right)\left|A\right|^2 A \tag{3.20}$$

3.4 . Supercontinuum triggered in anomalous GVD regime

3.4.1 . Optical soliton

The most common configuration to generate a supercontinuum is taking advantage of the optical soliton. To do this, the pump needs to be located at the anomalous GVD regime of the waveguide. During the pulse propagation, the effect of SPM anomalous GVD has opposite outcomes. We consider a Gaussian shape pump with $T_0 = 100\,\mathrm{fs}$, nonlinear coefficient $\gamma = 1\,\mathrm{W/m}$, and a fixed pump peak power $P_p = 100\,\mathrm{W}$ at a wavelength of1550 nm, resulting in $L_{NL} = 0.01\,\mathrm{m}$ according to Equation.3.9. To have SPM and GVD perfectly balanced under these conditions, β_2 is chosen to be $1000\,\mathrm{ps^2/km}$, leading to soliton number $N = 1$ defined as:

$$N = \sqrt{L_D/L_{NL}} \tag{3.21}$$

The evolution for both temporal and spectral profiles don't vary with propagation, also being named as fundamental soliton as shown in Figure.3.6(a). If the SPM effect overcomes anomalous GVD, the pulse evolution goes through a breathing effect, which means the temporal and spectral profile periodically represent themselves through propagation, also known as higher-order soliton. In Figure.3.6(b,c), the breathing effect is shown with $N = 2$ and 3 with $\beta_2 = 250$ and $111\,\mathrm{ps^2/km}$, respectively. The higher-order soliton always first goes through a stage featuring time domain compression and spectral domain broadening. This pulse compression originates from the soliton itself. Thus, it is called soliton self-compression (SSC). The pulse peak power is dramatically increased due to SSC, and the spectrum broadens very efficiently.

The propagation distance for SSC to reach maximum spectrum broadening can be estimated [3]by empirical equation written as:

$$L_{SSC} = \sqrt{L_D} \cdot \sqrt{L_{NL}} = \frac{T_0^2}{|\beta_2|} \cdot \frac{1}{\gamma P_0} \tag{3.22}$$

3.4.2 . Perturbation of higher-order dispersion

In an ideal scenario without higher-order dispersion (HOD), the pulse would eventually revert to its original shape after a certain propagation distance due to the periodic behavior of a higher-order soliton, as discussed previously. However, in practical waveguides, HOD is always present and acts as a perturbation. The existence of HOD will force the GVD to have both anomalous and normal regions. When the spectrum broadens significantly during SCG, potentially reaching the normal dispersion regime, the influence of HOD becomes significant. This prevents the initial soliton from maintaining its form, leading to soliton fission. Although HOD is just one of several factors, like the Raman effect and self-steepening, that lead to soliton fission, it is especially important because it enables a highly efficient frequency conversion during soliton fission called dispersive wave (DW) generation. This process relies heavily on the phase-matching condition, which is closely linked to HOD.

The DWs are usually generated in a normal GVD regime, where soliton cannot exist in a stable way. Therefore, DW generation is considered as an efficient way of spectral broadening. The spectral location of DW is governed by phase-matching condition, being written as:

$$\beta(\omega) - \beta(\omega_s) - v_g^{-1} \cdot (\omega - \omega_s) - \frac{\gamma P_s}{2} = 0 \tag{3.23}$$

who has a physical meaning that the phase constant of the main soliton after soliton fission, whose frequency is ω_s and peak power is P_s, matches the one of the DW? The terms with

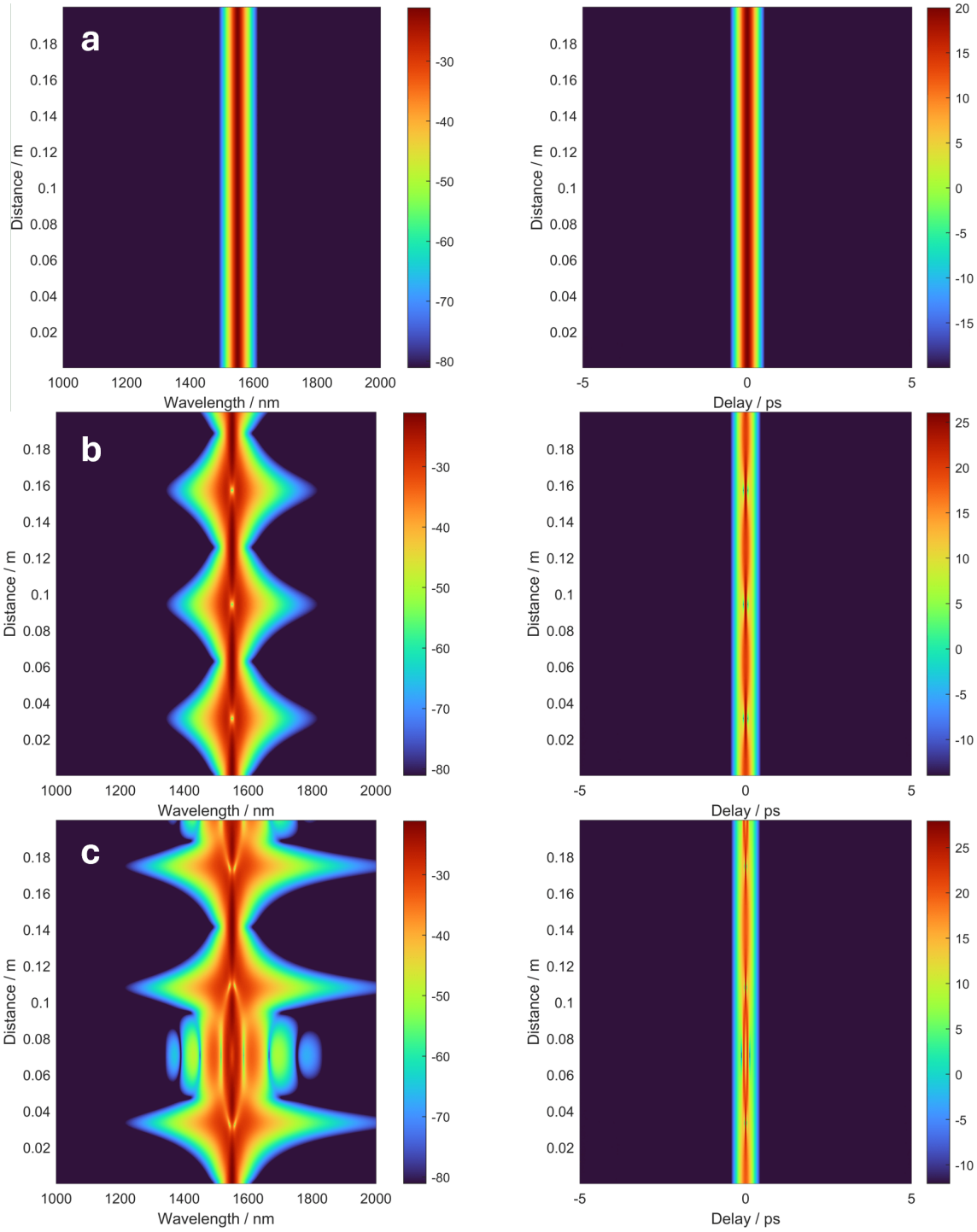

Fig. 3.6. Soliton spectrum (left column) and temporal profile (right column) evolution with propagation distance. The soliton number is N = 1, 2, 3 for (a, b, c) respectively. Gaussian shape pump has properties as $T_0 = 100\,\mathrm{fs}$, pump peak power $P_p = 100\,\mathrm{W}$ at wavelength 1550 nm. β_2 is 1000, 250, and 111 $\mathrm{ps}^2/\mathrm{km}$ respectively for (a, b, c).

v_g and γ represent the phase contribution of soliton group velocity and SPM to the soliton, respectively. P_s is estimated by the formula with peak power P_0 [4]: $P_j = P_0 \frac{(2N-2j+1)^2}{N^2}$ given j = 1 as the first soliton ejected after soliton fission. The soliton frequency ω_s is usually considered the same as the pump frequency ω_o. By disregarding the nonlinear term $\frac{\gamma P_s}{2}$, the left-hand side of Equation.3.23 is termed to be integrated dispersion β_{int}. It can be rewritten as a Taylor expansion around ω_0:

$$\beta_{int}(\omega) = \sum_{n\geq 2} \frac{(\omega-\omega_0)^n}{n!} \frac{\partial^n \beta}{\partial \omega^n} = \sum_{n\geq 2} \frac{(\omega-\omega_0)^n}{n!} \beta_n \tag{3.24}$$

It can be seen from Equation.3.24 that GVD (β_2) and HOD ($\beta_n, n > 2$) govern the phase matching condition for DW, especially when the nonlinear term is negligible when peak power is not so high (in our case, hundreds to kilowatt).

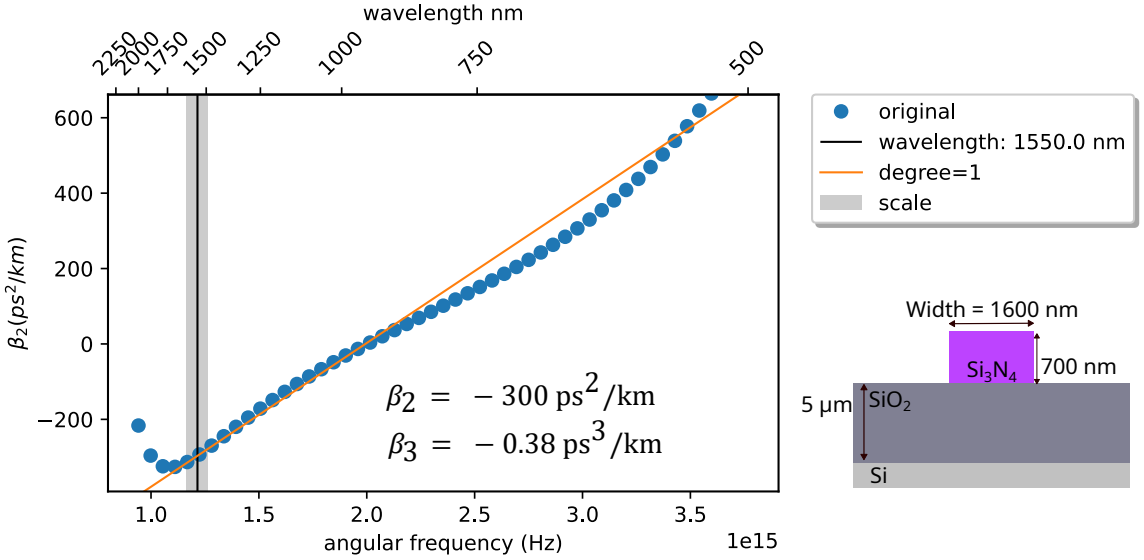

Fig. 3.7. Higher order dispersion at 1550 nm wavelength on a strip 700 nm Si_3N_4 waveguide with width 1600 nm. The β_2 are simulated (in blue dots) given the cross-section as shown in right corner. β_3, as the first order derivative of β_2 over angular frequency using Equation.3.13 in the scale range at 1550 nm wavelength, serves as the higher order dispersion.

Considering a 1-cm long Si_3N_4 waveguide with height 700 nm and width 1600 nm (the cross-section is shown in Figure.3.7), β_2 can be simulated considering the material dispersion and waveguide geometry as shown in Figure.3.7 in blue dot. At 1550 nm wavelength, the GVD β_2 and the dominant HOD β_3 is found to be -300 $\mathrm{ps}^2/\mathrm{km}$ and 0.38 $\mathrm{ps}^2/\mathrm{km}$, respectively. The nonlinear coefficient γ equals to $1.1\mathrm{W/m}$.

Given a pump at a wavelength of 1550 nm that has a squared hyperbolic secant envelope (Equation.3.10), $T_{FWHM} = 190\,\mathrm{fs}$ with $P_0 = 2\,\mathrm{kW}$, the spectral broadening evolution in this 1-cm waveguide are shown in Figure.3.8(a, b, c) taking into account only β_2, β_2 and β_3, and all orders of dispersion, respectively. In Figure.3.8(a), only soliton is observed without DW. The figure shows the spectral evolution of a soliton with soliton number $N = 9.3$, calculated by Equation.3.21. When β_3 is introduced, DW is able to be generated. β_3, the slope of β_2, influences which DW the energy is preferentially transferred to. If $\beta_3 > 0$, the energy favors the generation of a DW on the blue (shorter wavelength) side as shown in Figure.3.8(b). If $\beta_3 < 0$,

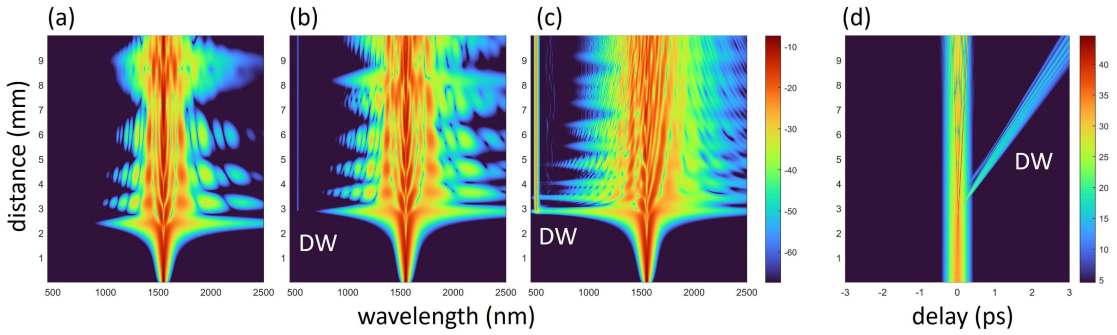

Fig. 3.8. Effect of higher-order dispersion (HOD) to dispersive wave (DW) generation. (a) Only $\beta_2 = -300\,\mathrm{ps}^2/\mathrm{km}$ is considered. (b) Additional HOD $\beta_3 = -0.38\,\mathrm{ps}^3/\mathrm{km}$ is considered. (c) The full dispersion is considered. (d) The simulated temporal pulse evolution is given the same conditions as (c), from which DW is identified.

the red side (longer wavelength) DW is preferred. By considering all orders of HOD using Equation.3.18, an accurate simulation is shown in Figure.3.8(c), showing significant energy transfers from the pump to DW. The temporal characteristic of DW is shown in Figure.3.8(d), which shows the temporal evolution of the SCG as in Figure.3.8(c). The DW is generated after the soliton fission and is separated from the soliton part because of the large group velocity difference.

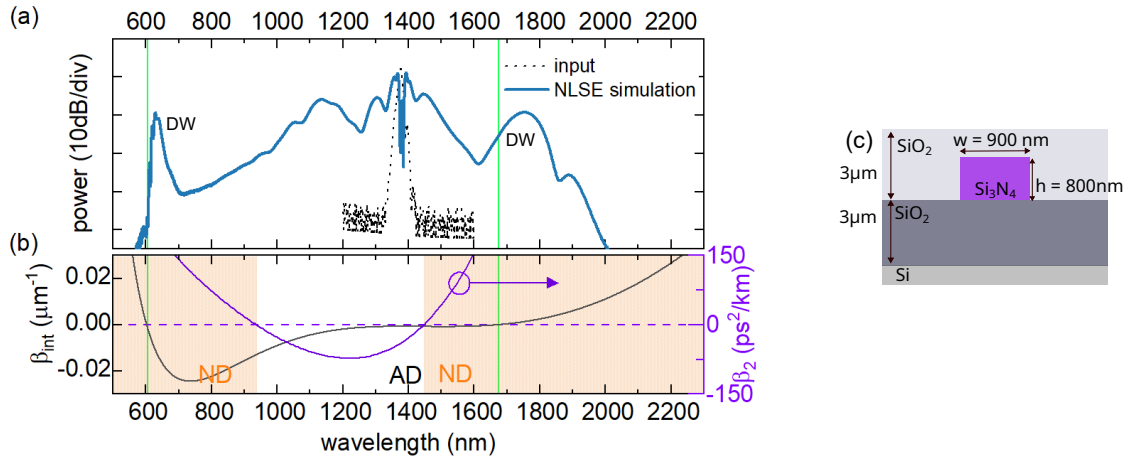

Fig. 3.9. Dispersive wave generation in a waveguide with a hyperbolic-shape GVD curve. (a) Spectral broadening in blue from NLSE simulation. Pump condition: 190 fs squared hyperbolic secant pulse. $P_0 = 290\,\mathrm{W}$ at 1380 nm wavelength. The pump pulse spectrum is shown in the dotted black curve. Propagation distance 2.3 cm. (b) GVD β_2 curve in purple shows a hyperbolic shape, indicating a non-negligible β_3 and β_4 contribution. β_{int} curve is shown in the black curve, indicating two phase-matching wavelengths. (c) The cross-section of the waveguide which the simulation are based on.

Apart from the dispersion curve that is dominated by β_2 and β_3 as shown in Figure.3.7, another common GVD curve is shown in Figure.3.9(b) in purple, where the hyperbolic shape GVD curve indicates an important β_3 and β_4. This GVD curve is simulated from a waveguide geometry shown in Figure.3.9(c), a typical configuration where the waveguide is buried in thick up-cladding. In this case, the anomalous GVD region is surrounded by two normal GVD

regions not far away. If set the pump wavelength in the anomalous region, two phase-matching wavelengths for DWs can be found. The simulated spectral broadening shows the generation of two DWs (Figure.3.9(a)) at the phase-matching wavelengths (in green lines) predicted by the phase-matching condition which is presented in Figure.3.9(b) black curve. These two DWs are located far away from the pump wavelength, broadening the spectrum efficiently.
By varying the waveguide geometry, the GVD shape can be tailored and thus control the DW generation. By carefully designing the waveguide geometry, which is also called dispersion engineering, a suitable supercontinuum can be generated according to different applications.

3.5 . Supercontinuum triggered in normal GVD regime

When the pump is located in the normal GVD regime of the waveguide, the spectral broadening mainly depends on SPM. Indeed, because SPM effect and GVD now impose the same chirp sign to the pulse, the pulse doesn't go through pulse compression but is continuously stretched instead. This leads to a quick decrease in peak power and limits new frequency generation from the SPM effect. Therefore, higher pump power is needed. However, the SCG in an all normal dispersion waveguide brings, in return, a flat and coherent spectral broadening. In an all normal dispersion (ANDi) waveguide, SPM and GVD still comes into play together. Since the pulse is propagates in ANDi, the instantaneous red-shift frequency travels faster than the blue-shift frequency, both of which are generated by SPM. Therefore, the leading edge and trailing edge will eventually be taken over by red-shift components and blue-shift components, respectively. In return, a steepening of the pulse edge and a smoothing of spectrum take place. This phenomenon is called optical wave breaking (OWB). New frequencies are generated during OWB via a degenerate four-wave mixing (FWM) at leading and trailing edge of the pulse. One of the characteristics pattern of OWB is the linearised frequency chirp since there is no longer a shared temporal position for different frequency components in the pulse.
The continuum generated in ANDi exhibits an excellent temporal coherent because SPM and OWB are more resistant to noise amplification than soliton dynamics. It is also interesting utilise this continuum as the first stage of pulse compression due to the linearised frequency chirp.
Supercontinuum triggered in normal GVD is not the center of this PhD thesis, but a detailed result can be found in [5].

3.6 . Spatial coherence and temporal coherence

Spatial coherence describes the ability for two spatial points in the extent of a wave to interfere when averaged over time. It is essential for some supercontinuum applications that need a confocal system like Optical Coherence Tomography and hyperspectral imaging as a diffraction-limited spot at the focal plan is usually needed for the resolution consideration. SCG is highly spatially coherent in general because only the fundamental mode is involved in frequency conversion. However, when using a multimode waveguide, the higher-order mode can be created due to perturbations like bending which harms spatial coherence. In addition, some techniques to tune the dispersive wave by phase-matching conditions in higher order mode[6] can also deteriorate spatial coherence.

Noise modeling for temporal coherence

Temporal coherence, on the other hand, is more critical during SCG. A good temporal coherence in SCG means that different frequency components in the short pulse have a fixed relative phase relation, and this phase relation remains the same for different pulses in the pulse train. The decoherence comes from noise amplification in the nonlinear dynamics, which changes the nonlinear process of each pulse. There are two main noise sources: quantum noise in the frequency domain as one photon per mode (OPPM) fluctuation and amplitude noise corresponding to relative intensity noise (RIN) from the laser source.
Numerically, the parameter of coherence $|g_{12}|$can be defined to evaluate the first-order degree of mutual coherence:

$$|g_{12}(\omega)| = \frac{\left|\left\langle A_i^*(\omega) A_j(\omega)\right\rangle_{i\neq j}\right|}{\sqrt{\left\langle |A_i(\omega)|^2\right\rangle \left\langle |A_j(\omega)|^2\right\rangle}} \tag{3.25}$$

where the angular bracket denotes an ensemble average over the pairs of spectra $[A_i(\omega), A_j(\omega)]$. A mutual coherence degree of 1 indicates perfect coherence within the spectrum, whereas a value of 0 signifies a complete lack of coherence within the spectral broadening. In practice point of view, $|g_{12}|$ is calculated through simulation and $[A_i(\omega), A_j(\omega)]$ refers to individual simulation spectra taking noise model into account. The two main noises come from the quantum shot noise using one photon per mode model and relative intensity noise[7], [8]. The degradation of the temporal coherence comes from noise-sensitive Modulation Instability (MI), which leads to different spectral broadening and soliton fission processes.
OPPM noise is modeled as a fluctuation of a single photon with an angular frequency ω with a random phase at each frequency grid $\delta f = 1/T_{width}$ within the simulation window T_{width}:

$$\delta_{OPPM} = \sqrt{\frac{\hbar\omega}{\delta f}} \cdot e^{i\cdot 2\pi X} \tag{3.26}$$

In Equation.3.26, $\hbar$ is the Plank constant. X is a random variable following a uniform distribution between 0 and 1.
RIN noise is considered in the time domain as a fluctuation in the pump's peak power, with a variance r specified by the laser's specifications:

$$\delta_{RIN} = rY \tag{3.27}$$

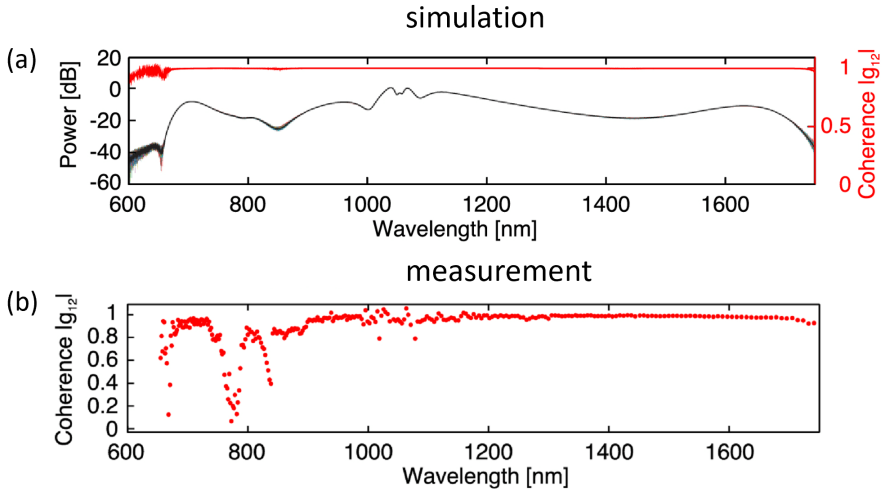

Fig. 3.10. Coherence parameter g_{12} from simulation and measurement. (a) Simulated spectral broadening is the black curve. Simulated $|g_{12}|$ is in red. (b) The measured $|g_{12}|$ by the interference a pulse with its successive counterpart is shown in red. The figure is adapted from [10].

In Equation.3.27, Y is a random variable following a normal distribution. In the end, the pump temporal envelope with noise A_{noise} can be modeled as:

$$A_{noise}(t) = \sqrt{1+\delta_{RIN}} \cdot \mathcal{F}^{-1}[\mathcal{F}[A_0(t)] + \delta_{OPPM}] \tag{3.28}$$

where $\mathcal{F}$ and $\mathcal{F}^{-\infty}$ are Fourier transform and inverse Fourier transform, respectively. $A_0(t)$ is the input pump temporal envelope without noise.
There are two common experimental ways to verify the temporal coherence. First, let the SC interfere with several coherent CW lasers that cover different spectral ranges[5]. The extinction ratio of the fringe will reveal the coherence. Second, imply a Michelson-type interferometry to allow one pulse to interfere with its successive counterpart by introducing a suitable temporal delay[9], [10]. The coherence across the entire spectral range of the continuum can be determined by analyzing the fringe pattern in the spectrum measured using an Optical Spectrum Analyzer. The details of the principle is explained in [10]. A simulated and measured $|g_{12}|$ are shown in Figure.3.10(a) and (b) in red from [10]. The simulation is in good agreement with the measured coherence.

3.7 . Conclusions

In this chapter, we explored the fundamental principles of supercontinuum generation (SCG) in materials exhibiting the optical Kerr effect. We began by examining two key physical mechanisms crucial for SCG: self-phase modulation (SPM) and group velocity dispersion (GVD). Their individual impacts on pulse chirp, which describes the variation of instantaneous frequency over the pulse duration, were analyzed. Next, we introduced the nonlinear Schrödinger equation (NLSE), a simplified version of the generalized nonlinear Schrödinger equation (GNLSE), adapted specifically for the integrated Si_3N_4 platform. This version incorporates all relevant nonlinear dynamics interacting with dispersion, excluding harmonic generation. We then detailed the most common configuration for SCG, where the pump wavelength is positioned in the anomalous dispersion regime. A critical nonlinear spectral broadening process, dispersive wave

(DW) generation, was discussed, which arises due to higher-order dispersion (HOD) perturbations. We also provided a brief introduction to spectral broadening when the pump operates within a waveguide entirely in the normal dispersion regime. Finally, we addressed spatial and temporal coherence, introducing a noise model to simulate the temporal coherence in SCG. This chapter offers foundational knowledge on SCG in dispersion-engineered waveguides, along with essential concepts required to understand pulse compression techniques.

References

[1] *Nonlinear Fiber Optics*, en. Elsevier, 2013, ISBN: 978-0-12-397023-7. DOI: 10.1016/C2011-0-00045-5.

[2] J. M. Dudley, G. Genty, and S. Coen, "Supercontinuum generation in photonic crystal fiber", en, *Reviews of Modern Physics*, vol. 78, no. 4, pp. 1135–1184, 2006, ISSN: 0034-6861, 1539-0756. DOI: 10.1103/RevModPhys.78.1135.

[3] J. M. Dudley and J. R. Taylor, Eds., *Supercontinuum Generation in Optical Fibers*. Cambridge: Cambridge University Press, 2010, ISBN: 978-0-511-75046-5. DOI: 10.1017/CBO9780511750465.

[4] Y. Kodama and A. Hasegawa, "Nonlinear pulse propagation in a monomode dielectric guide", en, *IEEE Journal of Quantum Electronics*, vol. 23, no. 5, pp. 510–524, 1987, ISSN: 0018-9197. DOI: 10.1109/JQE.1987.1073392.

[5] I. Rebolledo-Salgado, Z. Ye, S. Christensen, *et al.*, "Coherent supercontinuum generation in all-normal dispersion Si $_3$ N $_4$ waveguides", en, *Optics Express*, vol. 30, no. 6, p. 8641, 2022, ISSN: 1094-4087. DOI: 10.1364/OE.450987.

[6] D. D. Hickstein, G. C. Kerber, D. R. Carlson, *et al.*, "Quasi-Phase-Matched Supercontinuum Generation in Photonic Waveguides", en, *Physical Review Letters*, vol. 120, no. 5, p. 053 903, 2018, ISSN: 0031-9007, 1079-7114. DOI: 10.1103/PhysRevLett.120.053903.

[7] J. M. Dudley and S. Coen, "Coherence properties of supercontinuum spectra generated in photonic crystal and tapered optical fibers", en, *Optics Letters*, vol. 27, no. 13, p. 1180, 2002, ISSN: 0146-9592, 1539-4794. DOI: 10.1364/OL.27.001180.

[8] E. Genier, P. Bowen, T. Sylvestre, J. M. Dudley, P. Moselund, and O. Bang, "Amplitude noise and coherence degradation of femtosecond supercontinuum generation in all-normal-dispersion fibers", en, *Journal of the Optical Society of America B*, vol. 36, no. 2, A161, 2019, ISSN: 0740-3224, 1520-8540. DOI: 10.1364/JOSAB.36.00A161.

[9] M. Bellini and T. W. Hänsch, "Phase-locked white-light continuum pulses: toward a universal optical frequency-comb synthesizer", en, *Optics Letters*, vol. 25, no. 14, p. 1049, 2000, ISSN: 0146-9592, 1539-4794. DOI: 10.1364/OL.25.001049.

[10] A. R. Johnson, A. S. Mayer, A. Klenner, *et al.*, "Octave-spanning coherent supercontinuum generation in a silicon nitride waveguide", en, *Optics Letters*, vol. 40, no. 21, p. 5117, 2015, ISSN: 0146-9592, 1539-4794. DOI: 10.1364/OL.40.005117.

4 - Fabrication and characterization of Si_3N_4 waveguide

Summary

Thanks to its large band gap close to 5 eV, Si_3N_4 has a wide transparent window from 0.35 μm to 7 μm with no two photon absorption in near-IR range. In return, Si_3N_4 has a moderate Kerr nonlinearity. Therefore, long propagation distance is favorable to accumulate nonlinear effect which inevitable requires low-loss waveguides. Many fabrication techniques have been proposed towards low-loss or even ultra low-low Si_3N_4 circuit. Here, we take advantage of CEA Leti's 800 nm Si_3N_4 platform. The design of this fabrication follows the standard Process Design Kit (PDK) of the foundry, ensuring good waveguide geometry control. In parallel, we also develop our fabrication process for Si_3N_4 circuit based on Si_3N_4 wafer provided by CEA Leti to benefit from more flexible fabrication schedule, small feature size of Ebeam and possiblity to change the cladding material.

4.1 . Ultra-low-loss 800nm silicon nitride platform in CEA Leti

4.1.1 . Fabrication process

The fabrication is performed at CEA-Leti, using its 200 mm Si_3N_4 photonic platform [1]. The stoichiometric Si_3N_4 is deposited by Low Pressure Chemical Vapor Deposition (LPCVD) at 780 °C on top of a 3 µm thick thermal oxide. In order to avoid cracks and delamination, the oxide surface is pre-patterned with dummy holes and the Si_3N_4 is deposited using a two-steps process with a wafer rotation of 45°. The Si_3N_4 film is patterned using 248nm deep ultra-violet photolithography and dry etching. The wafer undergoes a series of thermal annealing in O_2 and N_2 atmospheres. Then, the waveguides are encapsulated using a High Density Plasma oxide deposition. Finally, the facets for edge coupling are defined thanks to the etching of deep trenches in SiO_2 and the Si substrate.

4.1.2 . Dispersion engineering

A schematic view of the waveguide section is shown in Figure.4.1(c). The fixed waveguide height of 800 nm is chosen because of the flexibility of dispersion engineering by changing the

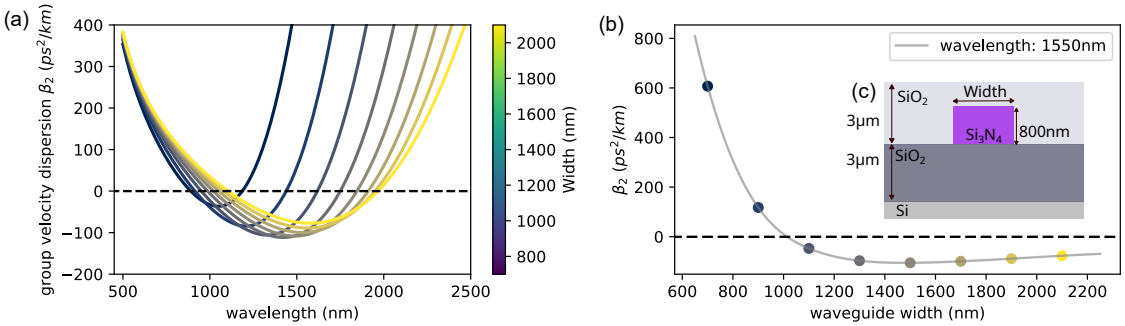

Fig. 4.1. Dispersion engineering for 800 nm Si_3N_4 platform in CEA Leti. Simulations are made in fundamental TE mode. (a) GVD curves as a function of waveguide width. (b) GVD curve in difference waveguide widths at the fixed wavelength of 1550 nm. (c) A schematic view of the waveguide cross section.

waveguide width in this thickness. The GVD curve is calculated using Lumerical Mode solution, considering the material dispersion and the waveguide cross section geometry. In Figure.4.1(a), difference dispersion curves as a function of waveguide width are presented in the wavelength range from 500 nm to 2500 nm in the fundamental TE mode. The anomalous GVD range is tailored by waveguide width, showing that this platform is suitable for SCG pumped from 1 μm to about 2 μm wavelength. At a given wavelength at 1550 nm as shown in Figure.4.1(b), the GVD varies from normal to anomalous region as a function of waveguide width.

4.1.3 . Loss characterisation

There are three common ways to characterize the loss of a waveguide: cut back method, Optical Frequency Domain Reflectometry (OFDR), and resonance of a ring resonator, respectively. We will discuss the advantages and disadvantages of these methods and discuss how these methods help us measure loss on different samples.

Cut-back method

The most commonly used technique to determine waveguide propagation loss is the cut-back method. This involves measuring the transmittance of waveguides with varying propagation lengths. The propagation loss is then calculated as the slope of the linear fit between transmittance and waveguide length.

The experiment setup for transmittance measurement is shown in Figure.4.2(a). A tunable laser is first directed into a polarization controller, where the polarization of the light is adjusted by applying controlled stress to the fiber. Next, it is connected to the optical component tester (CT400) through the IN port, where the power is measured as a reference. The light from the OUT port of the CT400 is then passed through a free-space polarizer to ensure the correct polarization. The polarization controller is aligned such that the combined effect of the controller and the CT400 matches the polarization set by the polarizer as the TE mode. A polarization-maintaining (PM) fiber is subsequently used to preserve the TE mode, which is then coupled into a lens fiber for injection into the sample waveguide. Another lens fiber collects the output from the waveguide and directs the light to the DETECTOR port of the CT400, where the transmittance is measured and calculated relative to the reference power obtained earlier.

An ideal measurement of the cut-back method requires at least three waveguides with different

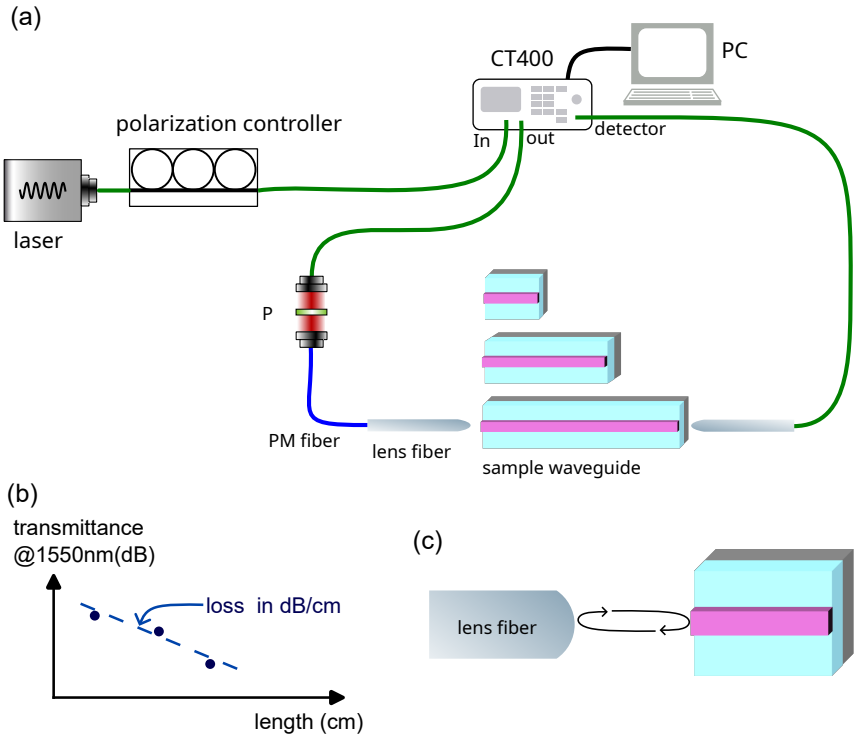

Fig. 4.2. The experimental loss measurement by cut-back method. (a) The experiment setup for transmittance measurement. P: polarizer; PM fiber: polarization-maintaining fiber. (b) Illustration of loss measurement deducing from the slope of the transmittance to the length. (c) The reflection between the lens fiber and waveguide facet forms a Fabry-Perot cavity.

lengths. As shown in Figure.4.2(b), three transmittance measurements can define the slope using least mean square method, thus giving the loss. As the transmittance is measured in a large spectral range, the loss as a function of wavelength can also be deduced.

In Figure.4.3, we show the transmittance measurements of waveguide width 1100 nm with different propagation distances in TE mode. Measurements were performed using cascaded tunable CW lasers with wavelengths ranging from 1260 nm to 1640 nm. However, there is a gap around 1375 nm, as the lasers do not cover this region. Four waveguide lengths were evaluated: 0.4 cm, 2.1 cm, 4.3 cm, and 21 cm, with the waveguides bent in spirals to minimize footprint. Some oscillations were observed in the transmittance, attributed to reflections between the lens fiber and the waveguide facet, forming a Fabry-Perot cavity (as shown in Figure 4.2(c)). For the shorter waveguides (0.4 cm, 2.1 cm, and 4.3 cm), the transmittance curves are very similar, indicating minimal loss. The differences are difficult to distinguish due to the oscillations. However, the transmittance for the 21 cm waveguide is notably lower, reflecting the impact of longer propagation lengths. By comparing the 0.4 cm and 21 cm waveguides, a loss of approximately 0.2-0.3 dB/cm is inferred, with shorter wavelengths experiencing slightly higher losses due to stronger mode confinement.

The main advantage of the cut-back method is that it directly measures propagation loss across different spectral ranges. However, accurate results require waveguides of varying lengths that are well-balanced for effective loss retrieval through linear regression. For low-loss waveguides, longer lengths are necessary to achieve noticeable differences in transmittance, which can demand a substantial footprint, particularly when the loss is below 1 dB/cm. Moreover, the accuracy of the cut-back method is highly dependent on maintaining consistent coupling effi-

ciency across the different waveguides tested.
In conclusion, the cut-back method is suitable for large sample where different length waveguides can be fabricated with similar coupling efficiency.

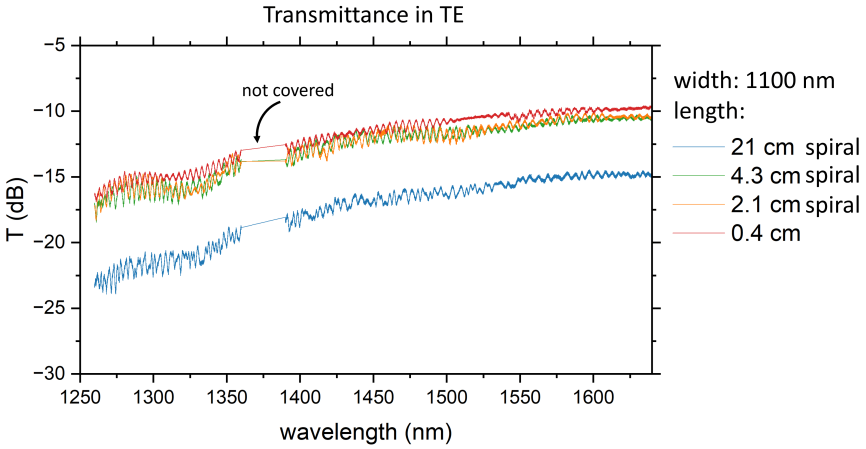

Fig. 4.3. The transmittance measured for cut-back method measured in TE mode. Four different length waveguides with the same waveguide width 1100nm are tested: 0.4cm, 2.1cm, 4.3cm,.3 cm and 21 cm.

Optical Frequency Domain Reflectometry

An alternative method to measure the loss is Optical Frequency Domain Reflectometry (OFDR)[1]. The waveguide is considered as a Mach-Zehnder interferometry, as shown in Figure.4.4(a). Given an input field A_0, a portion of the light (in red) passes straight through the waveguide, undergoing only a phase delay and attenuation without reflection. Another portion of the light (in blue) is reflected twice: once backscattered at distance l and again reflected at the facet. This second portion undergoes an additional amplitude decay of $\exp(-\alpha \cdot 2l)$, where α represents the loss in cm^{-1}, and l denotes the position of the backscattering. The total transmittance can be considered as the interference between these two light portions. By applying a Fourier transform to the transmittance, it is possible to retrieve the reflection response of the waveguide inner reflections in the spatial (or temporal) domain, as depicted in Figure 4.4(b). It should be noted that for a waveguide of length L, the reflection response is based on a two-fold propagation distance due to the two reflections involved. Therefore, the effective propagation distance is $2L$. Aside from the two peaks corresponding to reflections at the input and output facets, the rest of the reflection response (in a waveguide without internal defects causing reflection) exhibits a constant slope. This slope reveals the waveguide loss in dB/cm. The experiment setup is the same as in Section.4.1.3, shown in Figure.4.2(a).
The measurement is carried out in a 4.3-cm long 1100 nm wide Si_3N_4 waveguide in TE mode. The transmittance from wavelength 1400 nm to 1640 nm is shown in Figure.4.5. The transmittance for shorter wavelengths is lower than for longer wavelengths. This is due to the system response, which includes the wavelength-dependent performance of the polarization controller and the coupling efficiency from the lens fiber to the tested waveguide. It is essential to remove the system response from the raw transmittance data because, after applying the Fourier transform, the system response will introduce unwanted artifacts at the beginning of the propagation length. These artifacts can disturb the linear fitting used to determine the waveguide loss.

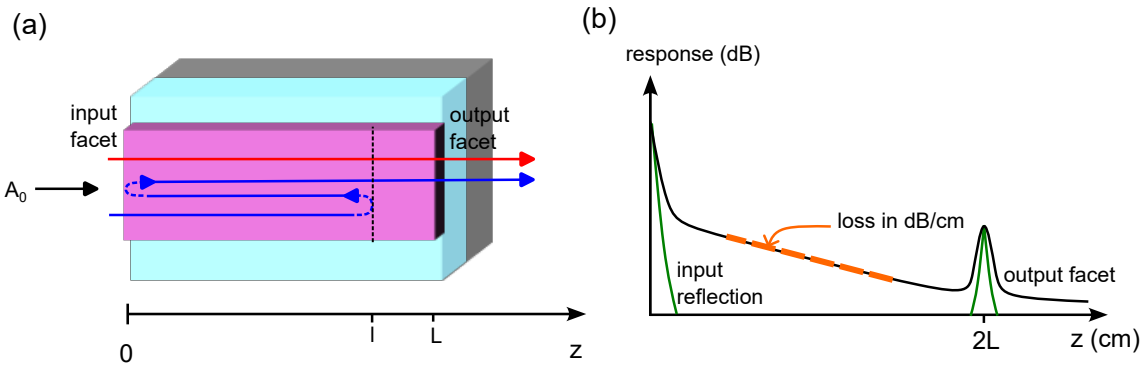

Fig. 4.4. Principle of Optical Frequency Domain Reflectometry. (a) The transmittance is considered as the interference between the light passing straight through the waveguide (red) and the light reflected twice (blue), once at position l and once at the input facet. (b) Reflection response given by the Fourier transform of the transmittance. The slope in the middle corresponds to the loss in dB/cm.

In order to remove the system response, a Savitzky-Golay filter, a kind of moving average filter, is applied to the original transmittance (shown in orange in Figure.4.5). This filter smooths the spectrum and the orange curve is considered as the system response. Then, the system response is removed, giving a filtered transmittance.

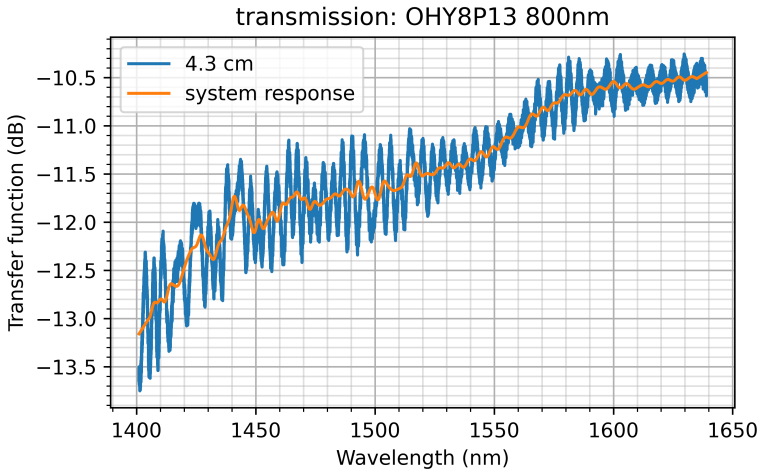

Fig. 4.5. The transmittance of a 4.3-cm long 1100 nm wide Si_3N_4 waveguide. Transmittance (in blue) is measured from 1400 nm to 1640 nm wavelength with a resolution of 1 pm. The system response (in orange) due to the experiment setup is obtained by the Savitzky-Golay filter.

We first analyze the transmittance around the wavelength of 1511 nm. The reflection response from the original transmittance and the filtered transmittance (where the system response has been removed) is presented in Figure 4.6(a) and (b), respectively. It is evident that the artifacts at the beginning of the propagation are significantly suppressed after filtering. In Figure 4.6(b), the reflection response reveals critical information, such as facet reflection (the peak observed at the end) and defects within the waveguide (multiple peaks seen in the middle of the reflectivity profile). The choice of the distance range for which the linear fitting is performed to estimate the loss is arbitrary, as shown between the orange dashed lines around the center. Using this method, the loss in dB/cm is calculated.

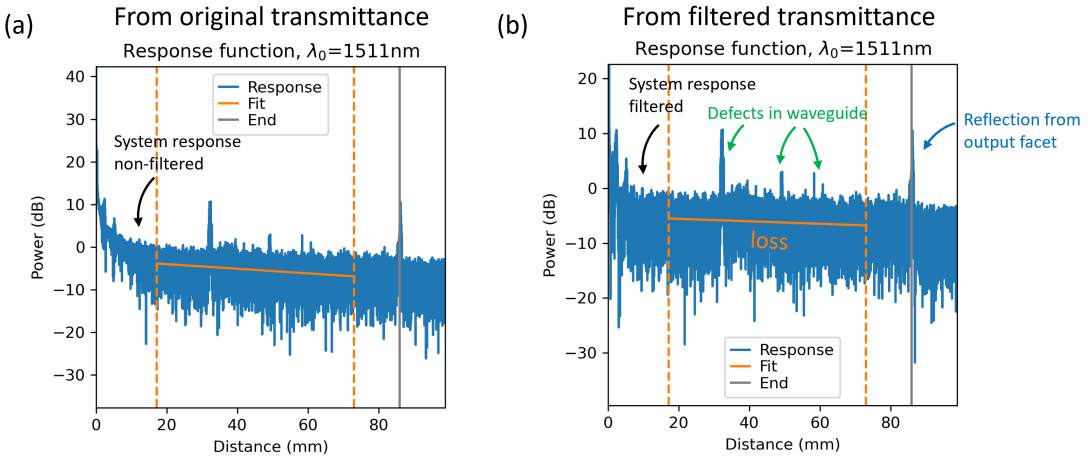

Fig. 4.6. Reflection response by OFDR on a 4.3-cm long 1100 nm wide Si_3N_4 waveguide. Reflection response from the original transmittance and system response filtered transmittance are shown in (a) and (b), respectively. The orange dashed lines indicate the linear fits, with the slopes determining the loss in dB/cm. The gray line represents the two-fold propagation distance, where the reflection from the output facet is located.

The loss in the function of wavelength is presented in Figure.4.7 by analyzing transmittance in different wavelengths. The loss is between 0.2-0.35 dB/cm in a broadband spectral range consistent with the results by cut-back method. The loss at shorter wavelength is characterised to be also strong than longer wavelength, agreeing with the cut-back method. The variances on the fitted coefficients are extracted from the diagonal elements of the covariance matrix, which is then used to calculate the uncertainties of the loss, as shown in Figure.4.7. The

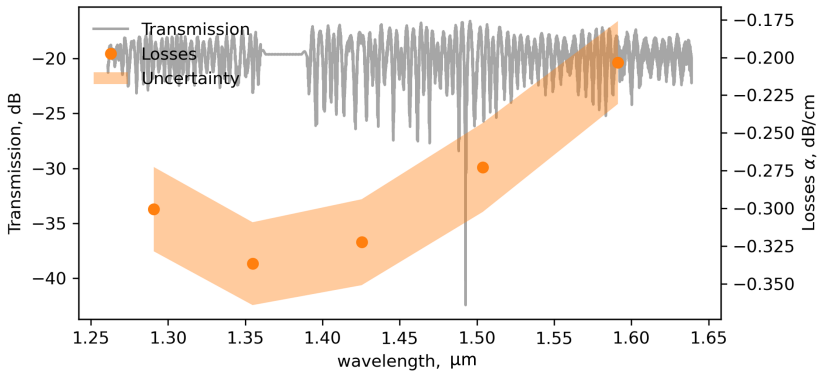

Fig. 4.7. Loss measured by OFDR on a 4.3-cm long 1100 nm wide Si_3N_4 waveguide. The wideband transmittance measurement is conducted from 1260 nm to 1640 nm, with the system response removed, as illustrated in gray. The corresponding loss in dB/cm, calculated from each transmittance, is plotted as a function of wavelength. The losses are shown as orange dots, with the associated uncertainties, derived from the variance of the linear fits, also provided.

loss we measured is higher than what is expected around 0.1 dB/cm[2]. In the reflectivity in Figure.4.6(b), multiple peaks can be found during the propagation which may be the reason for the excess loss. One possible reason for these reflection peaks is the waveguide design itself. The waveguide is structured as a rectangular spiral to minimize the footprint, with turns

implemented through 90-degree bends. The bend radius is 30 μm, which is relatively sharp for a Si_3N_4 waveguide. This sharp radius can cause mode mismatches at each bend, contributing to additional losses in the form of scattering and reflection.
There are some important advantages by using OFDR. First, compared with the cut-back method, OFDR only needs one waveguide to determine the loss. Thus, the footprint of the tested device is reduced to only one device. Second, from the reflection response, defects in the waveguide can be identified through the extra peaks in the propagation distance. However, since the loss calculation relies on the Fourier transform, high-resolution original transmittance measurements are necessary (the transmittance in this case has a resolution of 1 pm). Consequently, OFDR requires a highly tunable laser. Moreover, because a significant difference in reflection response is needed for accurate loss determination, the propagation length must still be sufficiently long, particularly when the loss is below dB/cm, which demands longer waveguides for the test.

Extract loss from a ring resonator

While cut-back and OFDR are powerful methods for loss characterization, waveguides with enough propagation length are needed. When the loss level enters into a low/ultra-low regime (from dB/cm to 0.1dB/cm), the length for a significant transmittance drop increases to several cm, which inevitably consumes a considerable device footprint on the wafer. Alternatively, a ring resonator is a compact device of which propagation loss can be deduced from its quality factor (Q factor)[3].
A basic ring resonator in all-pass configuration consists of a bus waveguide and a ring[4](Figure.4.8). The evanescent field of the mode propagating in the bus waveguide is coupled into the ring. When the optical fields in the ring build up a round trip phase shift that equals an integer times of 2π, they interferes constructively and the cavity is in resonance. The resonance wavelength can be expressed by group index n_g, round trip L and positive integer m as:

$$\lambda_{res} = \frac{n_g L}{m} \quad m = 1, 2, 3, ... \tag{4.1}$$

The resonance frequency ν_{res} can thus be expressed as:

$$\nu_{res} = m \cdot \frac{c}{n_g \cdot L} \quad m = 1, 2, 3, ... \tag{4.2}$$

where c is the speed of light. In transmittance at the resonance wavelength/frequency is present as a dip peak. The frequency range between two resonance or free spectral range (FSR)[5] is described as:

$$\Delta\nu_{FSR} = \frac{c}{n_g \cdot L} \tag{4.3}$$

From Figure.4.9(a), a transmittance of a ring resonator is shown, of which the diameter, waveguide width and gap are 80 μm, 1100 nm and 440 nm, respectively. The experiment setup is the same as is shown in Figure.4.2(a). The input laser is in TE mode. The resonance wavelengths or frequencies are identified and displayed in Figure 4.9(b), where the FSR $\Delta\nu_{FSR}$ can also be determined. Interestingly, in addition to the resonance peaks marked in orange, there are accompanying resonance peaks marked with green dots. This is attributed to the presence of residual TM modes. The polarization of the injected mode is influenced by both the polarizer and the orientation of the polarization-maintaining (PM) fiber. Although the

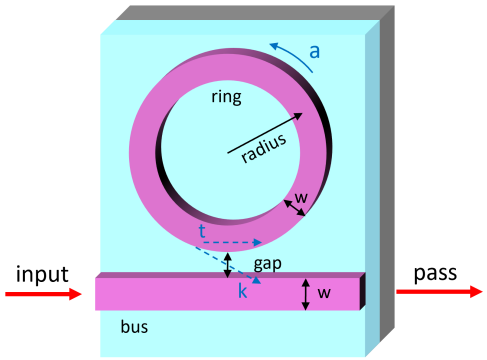

Fig. 4.8. All-pass ring resonator configuration. The bus waveguide and the ring share the same width w, with a small gap between them for coupling. The self-coupling coefficient is denoted by t, the cross-coupling coefficient by k, and a represents the single-pass amplitude transmission, accounting for both propagation loss and the loss at the coupler. Light is injected at the input, and the transmitted signal is measured at the output.

polarizer is set to TE mode, any misalignment of the PM fiber's orientation can reintroduce a TM component, which is then injected into the bus waveguide.
For a given resonance, the transmission drops at those wavelengths where field amplitude builds up in the ring. An example of the resonance is shown in Figure.4.9(c) where the measurement points are fitting by a Lorentzian function that can be applied to fit the degenerate resonance[6] as:

$$f(\nu) = -A\frac{1}{1+(\frac{\nu-\nu_{res}}{\Delta\nu_{FWHM}/2})^2} + B(\nu) \tag{4.4}$$

where ν_{res} is the mean frequency of the distribution corresponding to the resonance frequency, $\Delta\nu_{\mathrm{FWHM}}$ is the full width at half maximum, A is the amplitude and $\mathrm{B}(\nu)$ is the response of the coupling system serving as an offset. This offset can be expressed as:

$$B(\nu) = b_0 + b_1(\nu - \nu_{res}) \tag{4.5}$$

By applying the least mean square method, a set of $(\mathrm{A},\ \nu_{\mathrm{res}},\ \Delta\nu_{\mathrm{FWHM}})$ can be found for each resonance, which can be used to calculate quality factor Q, the finesse $\mathcal{F}$ of the resonance, and the extinction radio $\mathcal{E}$. These characteristics values can be defined as follows:

$$Q = \frac{\nu_{res}}{\Delta\nu_{FWHM}} \tag{4.6}$$

$$\mathcal{F} = \frac{\Delta\nu_{FSR}}{\Delta\nu_{FWHM}} \tag{4.7}$$

$$\mathcal{E} = \frac{T_{max}}{T_{min}} = \frac{B(\nu_{res})}{B(\nu_{res}) - A} \tag{4.8}$$

From Ref.[3], the propagation loss can be calculated from the finesse $\mathcal{F}$ and extinction ratio $\mathcal{E}$ of a resonance. The single-path amplitude transmission (ot the total loss coefficient) is a, which includes both propagation loss in the ring and loss in the coupler[7]. The self-coupling coefficient is t and the cross-coupling coefficient is k with respect to the ring itself. Thus t^2

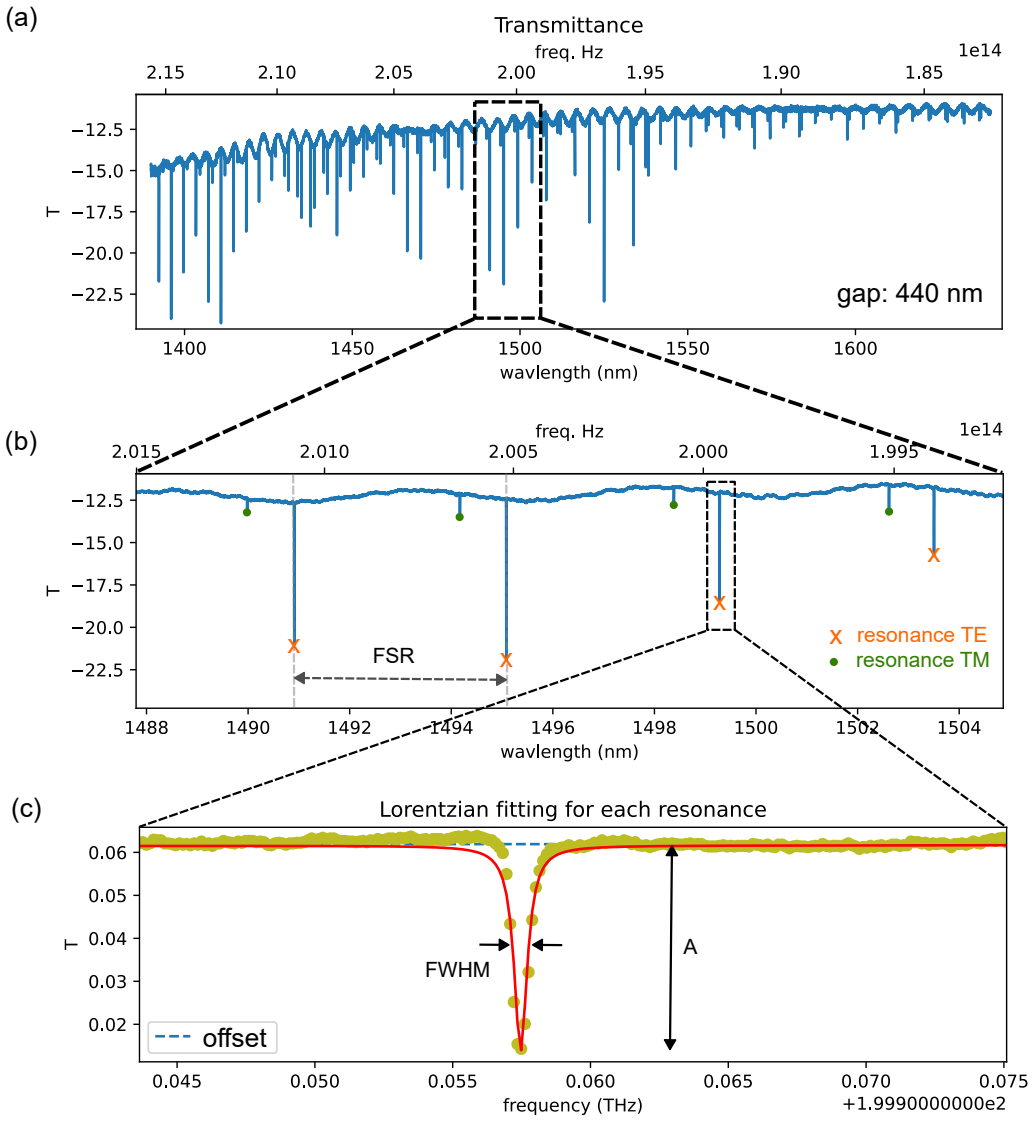

Fig. 4.9. Transmittance measurement, FSR and resonance fitting in a ring resonator. This ring resonator has parameters as follows: diameter 80 μm, gap 440 nm, bus and ring waveguide width 1100 nm. (a) The transmittance is measured from 1390 nm to 1640 nm with 1 pm resolution. (b) A zoom-in to identify the resonance wavelength/frequency. (c) The measurements around the resonance are shown in dots, and the fitting is shown in the red curve.

and k^2 define the power-spitting radios of the coupler, and they follow $\mathrm{t}^2 + \mathrm{k}^2 = 1$ in a lossless coupling section. a and t can be expressed as:

$$(a, t) = (\frac{U}{V})^{1/2} \pm (\frac{U}{V} - U)^{1/2} \tag{4.9}$$

where

$$U = \frac{\cos(\pi/\mathcal{F})}{1 + \sin(\pi/\mathcal{F})} \tag{4.10}$$

$$V = 1 - [\frac{1 - \cos(\pi/\mathcal{F})}{1 + \cos(\pi/\mathcal{F})}] \cdot \frac{1}{\mathcal{E}} \tag{4.11}$$

The solution of (a, t) in Equation.4.9 is interchangeable, with no indication of which root corresponds to which quantity. Therefore, to identify these two quantities, we have to consider their wavelength-dependent behavior. For the total loss coefficient a, it is usually wavelength insensible if the measurement is far away from the absorption line of the material. On the other hand, the self-coupling coefficient t can be approximated to a sinusoidal function with wavelength. Therefore, a large band analysis can distinguish these two parameters.

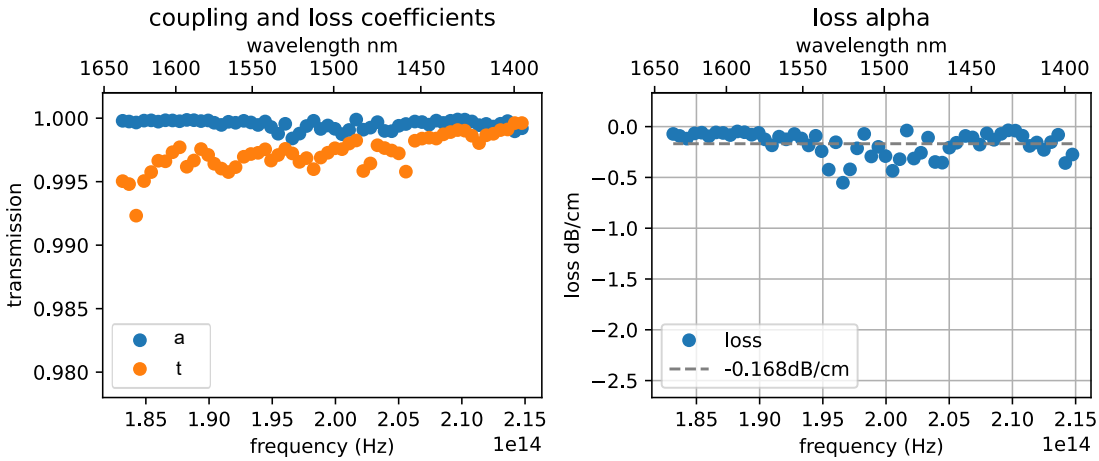

Fig. 4.10. Loss calculation by ring resonator. (a) self-coupling coefficient t and loss coefficient a from the spectrum shown in Figure.4.9 are shown in orange and blue, respectively. (b) The loss deduced from a knowing that the ring has a diameter of 80 μm. Blue dots are measurements and the dashed gray line is the average value.

From the measured transmittance in Figure.4.9(a), (a, t) as a function of frequency (or wavelength) is shown in Figure.4.10(a). The curve that varies significantly with frequency is identified as t, and the other is a. a is higher than t in the measured wavelength range, meaning the ring resonator is over-coupled. The loss of optical intensity in dB/cm can then be deduced by applying $\frac{10}{\mathrm{L}} \cdot \log \mathrm{a}^2$ where $\mathrm{L} = \pi \cdot \mathrm{D}$ is the round trip of a ring resonator and $\mathrm{D} = 80\,\mu\mathrm{m}$ in this sample. The corresponding loss is presented in Figure.4.10(b), indicating an average propagation loss of the 1100 nm wide waveguide is 0.17 dB/cm from 1400 nm to 1640 nm spectral range.

Compared with the results using the cut-back and OFDR methods, the loss obtained by ring resonator is in the same order of magnitude but slightly lower. Knowing that all the calculations from Equation.4.6 to Equation.4.9 are based on the fitting of each resonance, the accuracy of

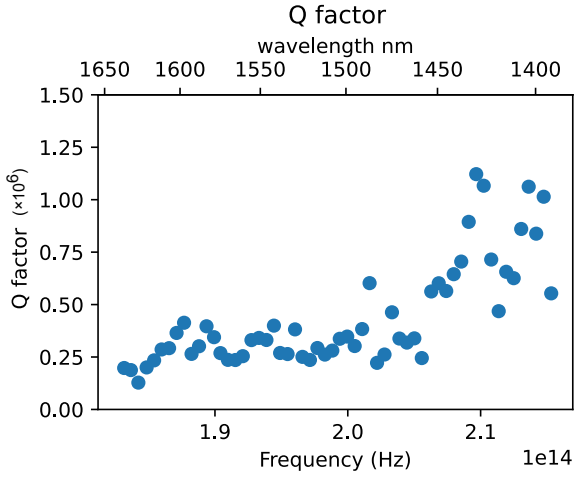

Fig. 4.11. Loaded Q factor. This ring resonator has parameters as follows: diameter 80 μm, gap 440 nm, bus and ring waveguide width 1100 nm.

the fitting determines the accuracy of loss. The spectrum measurement has a fixed resolution of 1 pm, which is often not sufficient for describing the resonance (see Figure.4.9(c)), giving birth to the uncertainty of Lorentzian fitting.

The measured Q factor (also known as the loaded Q factor), defined by Equation 4.6, physically represents the number of round trips required for the stored energy in the ring to decay to $1/e$ (approximately 37%). It depends on both the single-pass amplitude transmission a and the self-coupling coefficient t, as both are considered losses within the ring. The loaded Q factor measured based on Figure.4.9 is shown in Figure.4.11. The loaded Q factor rises from 250,000 to approximately 1,200,000 as the frequency increases. This occurs because, while the single-pass amplitude transmission a remains nearly constant across this spectral range, the self-coupling coefficient t increases with frequency.

Analysing the transmittance spectrum of a ring resonator offers a compact solution for loss characterization. Concerning the accuracy of the measurements, a high-resolution tunable laser needs to be used for low-loss waveguide. An alternative way is to increase the round trip of a ring, decreasing the single-path transmission a, which results in a wider FWHM in the resonance.

4.1.4 . Dispersion characterization

For the targeted supercontinuum application, the dispersion, controlled by waveguide cross-section geometry, needs to be verified with the simulation results. Here, measurements of dispersion based on ring resonators are carried out.

Given a waveguide cross-section geometry, the propagation constant β can be expressed as:

$$\beta = \frac{\omega}{c} \cdot n_{eff}(\omega) \tag{4.12}$$

where $n_{eff}(\omega)$ as a function of frequency shows the dispersion, yet can't be measured directly. On the other hand, the first derivative of the propagation constant β_1 (Equation.3.12) can be characterized by measuring the group index n_g as presented in Equation.4.13:

$$\beta_1 = \frac{d\beta}{d\omega} \equiv \frac{1}{v_g} = \frac{n_g}{c} \tag{4.13}$$

where n_g as a function of frequency can be calculated from FSR in a ring resonator which shares the same waveguide cross-section, expressed as in Equation.4.3:

$$n_g(\omega) = \frac{c}{\Delta\nu_{FSR} \cdot L} \tag{4.14}$$

Therefore, by identifying the free spectrum range of a given ring resonator, the dispersion (i.e. group velocity dispersion, group index variation as a function frequency or wavelength) of the waveguide can be figured out. The transmittance of the ring resonator is the same as shown

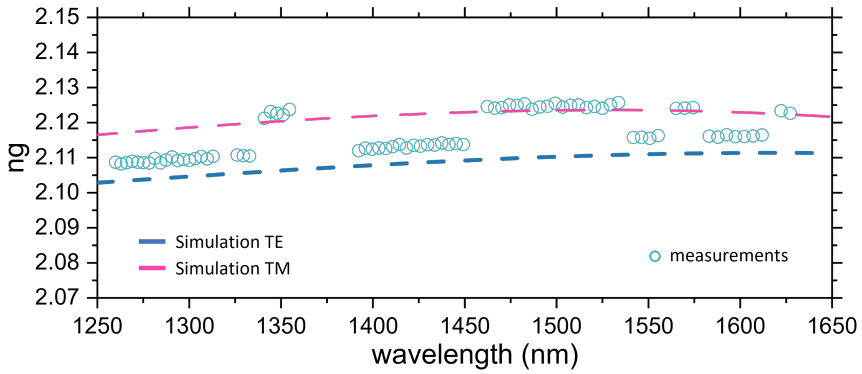

Fig. 4.12. Group index of the 800 nm height 1100 nm wide Si_3N_4 waveguides. Measured n_g, which is based on FSR in the ring resonator, is shown in blue circles. The simulated n_g in TE mode is in a blue dashed curve, and in TM mode, it in a pink dashed curve.

in Figure 4.9(a). In Figure 4.9(b), the resonance frequencies were identified, and the FSR $\Delta\nu_{FSR}$, was determined. We observed both the FSR corresponding to the TE mode and the residual TM mode. The group index n_g, calculated from the FSR using Equation 4.14, is shown in blue circles in Figure 4.12. It is evident that the measured n_g forms two distinct curves, corresponding to the two modes. The simulated n_g values for TE and TM modes are shown as blue and pink dashed lines, respectively. A good agreement between measurements and simulations indicates that the fabricated waveguide maintains an ideal cross-section, as described in [2]. By comparing with simulations, it is verified that the lower measured n_g values correspond to the TE mode, while the higher values correspond to the TM mode.
In conclusion, the measurements of n_g show a perfect fabrication quality in the waveguide geometry, delivering a dispersion almost the same as simulations.

4.2 . Low-loss silicon nitride waveguide fabrication in C2N cleaning room

While the fabrication offered by CEA-LETI ensures an excellent fabrication quality in terms of waveguide geometry and propagation loss, the PDK of the foundry also imposes some unavoidable limitations. First, the foundry PDK gives a minimum feature size of hundreds of nm, which is not small enough for some integrated optical components like Bragg grating. Second, the standard fabrication process that operates in the foundry is obliged to have a thick SiO_2 up-cladding, inevitably forbidding any hybrid integration possibilities. Third, a fixed Si_3N_4 height of 800 nm is offered right now from CEA-LETI, while supercontinuum generation can benefit from another waveguide thickness in the dispersion consideration.
Under the above reasons, it is necessary to be able to fabricate Si_3N_4 in the clean of C2N. Different from other fabrication processes that begin from Si_3N_4 deposition, high-quality Si_3N_4 on insulator wafers by LPCVD deposition has already been offered by Leti. Therefore, the process will start with the definition of waveguide.

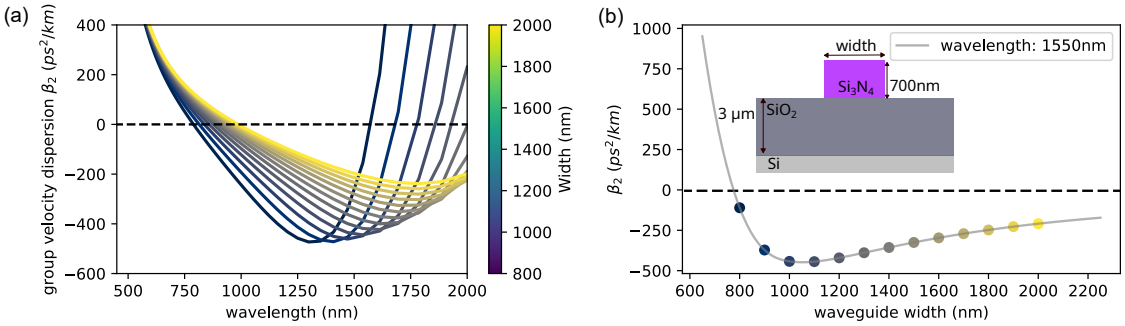

Fig. 4.13. Dispersion engineering for strip 700 Si_3N_4 waveguide. (a) GVD curves in the function of waveguide widths varying from 800 nm to 2000 nm. (b) GVD curve in difference waveguide width at the fixed wavelength 1550 nm. The schematic view of the waveguide cross-section is also shown.

The first targeted Si_3N_4 height is 700 nm because of the high mode confinement, benefiting the nonlinear effect. The GVD curves with different waveguide widths are shown in Figure.4.13(a). Compared with those of 800 nm buried Si_3N_4, strip 700 nm Si_3N_4 shows a deeper anomalous GVD with a steeper slope. The GVD curve at fixed wavelength of 1550 nm as a function of waveguide width is shown in Figure.4.13(b). Given the pump at telecom wavelength of 1550 nm, the short wavelength dispersive wave is approaching the visible spectrum (Figure.4.14). For the waveguide widths from 1400 nm to 1600 nm, the dispersive waves are likely to overlap with wavelength 517 nm, the three harmonic signal of the pump. Therefore, the strip 700 nm Si_3N_4 platform could be ideal for self-reference frequency comb through SCG.

4.2.1 . General fabrication process

The fabrication process for waveguide definition is shown in Figure.4.15. First, a proper thickness of the photoresist is deposited on the wafer. Second, a little sample is diced from the wafer. An electronic beam lithography then follows the design to expose the area, defining the parts that need to be removed afterward. After that, the sample is immersed in the development solution to remove the photoresist exposed to the electronic beam, leaving only the photoresist to protect the design pattern. Later, the sample is dry etched to have an isotropic sidewall

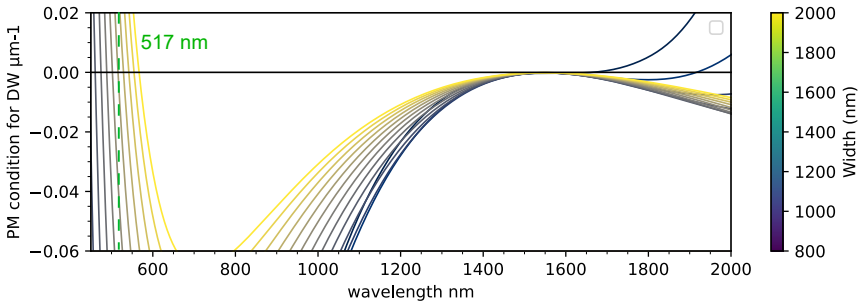

Fig. 4.14. Dispersive wave phase matching (PM) condition for strip 700 nm Si_3N_4 waveguides. Waveguides whose widths are from 1400 nm to 1600 nm are likely to have the dispersive wave generated around 517 nm, the third harmonic signal of the pump at 1550 nm wavelength.

(a sidewall that is close to 90 degrees). Before being ready for characterization. the sample is cleaned to remove any photoresist remaining on the surface. An additional annealing step can be introduced to the fabrication process to smooth the sidewall roughness and N-H bond absorption which will be explained in the next Section.4.2.3.
The whole fabrication process is similar to SOI platform. The strip Si_3N_4 pattern can be ready for upper deposition, and hybrid integration.

4.2.2 . Characterization

A step-by-step quality control has been carried out during the fabrication process. Beginning with surface observation, fissures are found on the die diced from the original wafer (Figure.6.10(a)). These cracks come from the high constraint inside the 700 nm thick Si_3N_4 layer. Different processes have already been developed, enabling high-quality thick Si_3N_4 without fissures. For example, the Damascene process that deposits Si_3N_4 on a reflowed SiO_2 trench[8]. Another way is to define a series of trenches around the edge of the wafer before the deposition of the Si_3N_4 film to prevent crack propagation[9]. However, both ways need to be done before the deposition. According to our current process flow shown in Figure.4.15, fissures are inevitable.
A layer of ZEP photoresist is coated on the single die by spin coating. The speed is set to be at 3500 r/min resulting in a ZEP thickness of around 250 nm. A scanning electron microscope(SEM) image shows the cross-section of the patterned photoresist shown in Figure.4.16(b), revealing the trapezoid shape photoresist after development. The thickness of the photoresist is enough for an 700 nm etching depth because the etch receipt has a selectivity of 1:3 meaning the photoresist can enable an etching depth of Si_3N_4 3 times as its own thickness. After the dry etching and cleaning of the residual photoresist of the waveguide, the sample is put again under SEM to verify the etching quality. To assess how etching quality changes with feature size, we focus on a Bragg waveguide (Figure 4.16(c)). A Bragg waveguide is a type of waveguide with a corrugated sidewall, designed to reflect specific wavelengths. In this case, the sinusoidal corrugation causes the etching feature size to vary from a maximum of 470 nm to 0, as seen in the top view in Figure 4.16(c). From this top view, it is evident that the upper portion of the waveguide is etched more than the bottom, indicating a trapezoidal cross-sectional shape. By measuring these differences and knowing that the waveguide is 700 nm thick, the corresponding etch angles were determined. It was found that the sidewall has a 10° inclination relative to the normal direction in the larger feature sizes, and this angle reduces to 5° for smaller feature sizes (95° with respect to the horizontal plane).

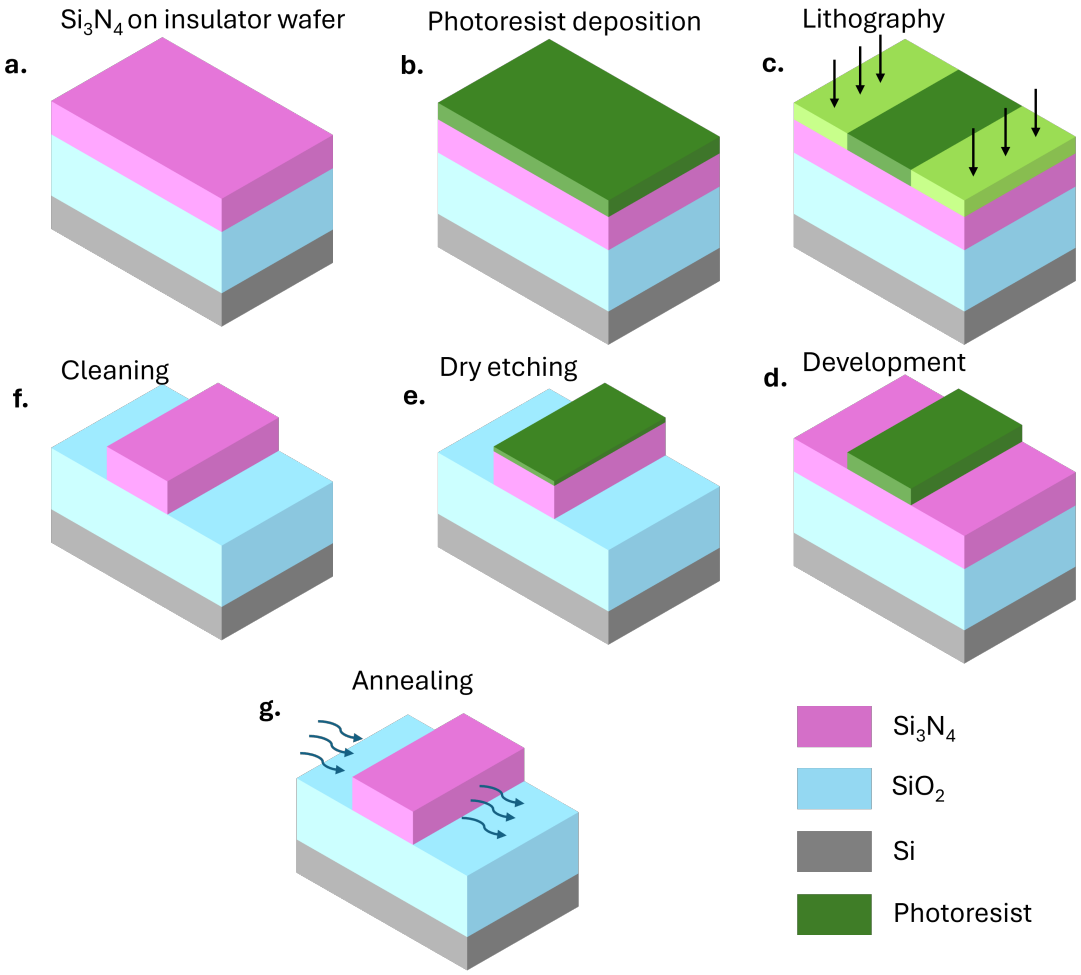

Fig. 4.15. The fabrication process of strip Si_3N_4 waveguide. The sequence of fabrication processes is shown from (a) to (g).

An inspection of the sidewall of a strip Si_3N_4 waveguide is performed to evaluate the roughness, which plays a crucial role in determining propagation loss. As displayed in Figure 4.16(d), the sidewall appears smooth with no significant roughness detected.
After the fabrication process, the sample is cleaved to observe the waveguide cross-section shown in Figure.4.16(e). The waveguide is in the center isolated by two trenches. The SiO_2 insulator layer is 3 μm.
The microscopy shows that many micropillars stand in the trench (Figure.4.16(d)). These micropillars obtain a shape like a Christmas tree. After testing the etching on a clean wafer, these micropillars still exist, proving that they are Si_3N_4 itself. A possible reason for these micropillars is that the dry etching recipe passivates the Si_3N_4 surface serving like a mask preventing the etching.

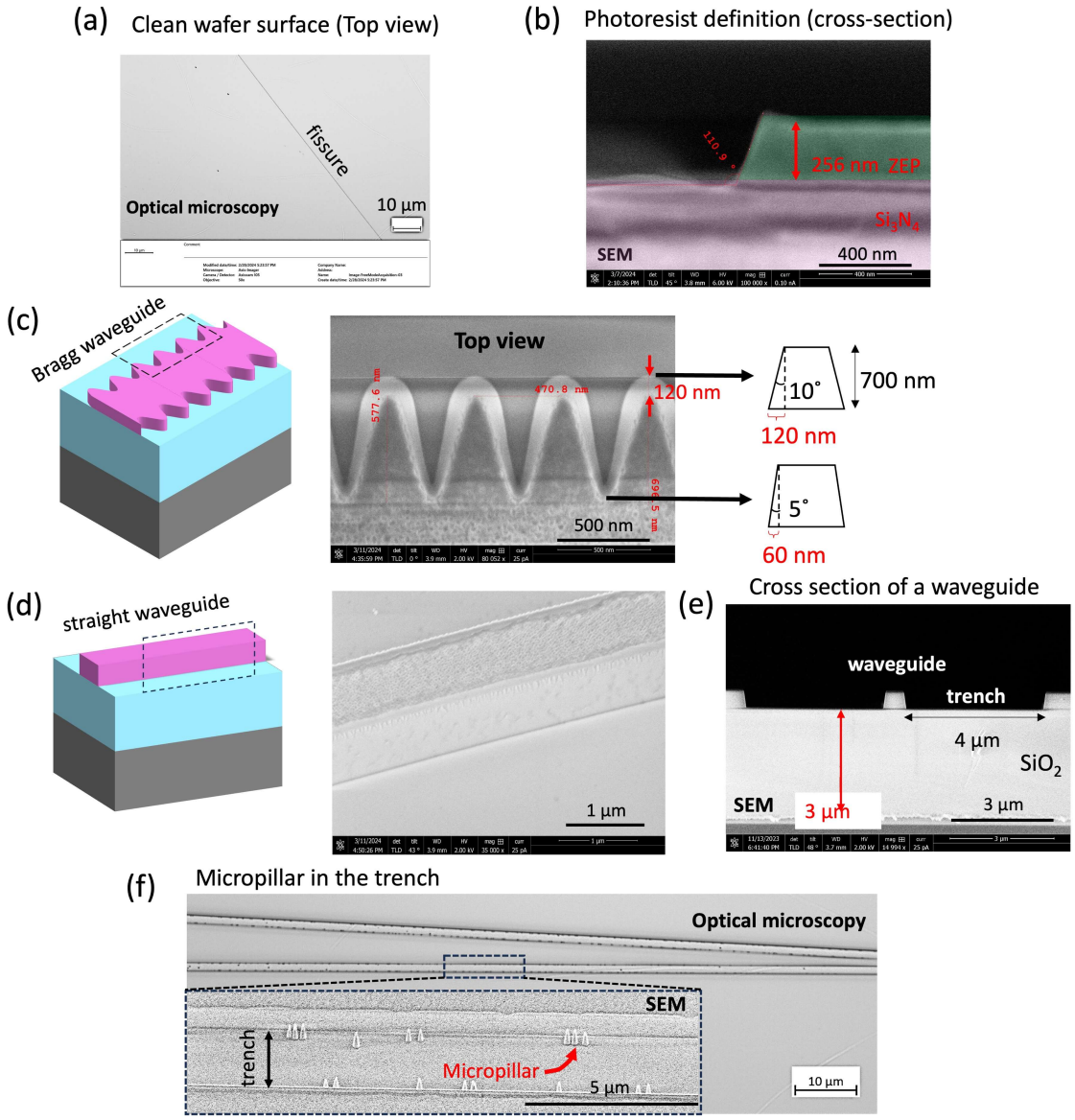

Fig. 4.16. Quality characterization during the fabrication. (a) Fissures are observed on the wafer surface due to the thick Si_3N_4 layer. (b) SEM image of the cross-section of a developed photoresist (ZEP) layer. The angle of inclination of the trapezoid is 110°(20°deviated from an ideal 90°angle). (c) Top view SEM image after dry etching and cleaning on a Bragg waveguide where the side walls have sinusoidal corrugation. The maximum inclination is 10°, decreasing with the feature size to 5 °. (d) SEM image on the side wall of a waveguide. (e) The cross-section SEM image after the fabrication process. (f) Top view on a tapered waveguide, where micropillars are found in the trench. The SEM image of micropillars is presented in the inset.

Apart from characterization during fabrication, loss measurement is also important to determine the quality of the process. Due to the fissures, ring resonators that take a smaller footprint are preferred for characterization among other techniques like the cut-back method and OFDR. The ring resonator is equipped with two integrated grating couplers for input and output as shown in Figure.4.17. A tunable laser source from 1500 nm to 1640 nm is injected into the ring resonator for transmittance measurement. The characterization setup is the same as shown in

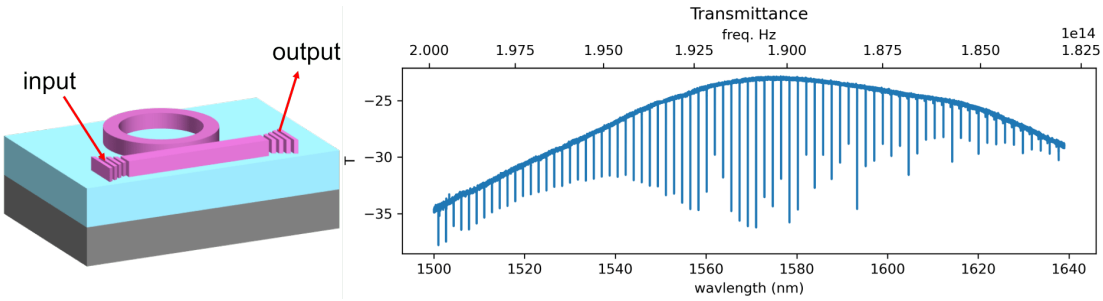

Fig. 4.17. Transmittance measured on a ring resonator with grating couplers for input and output. This ring resonator has parameters as follows: diameter 200 μm, gap 400 nm, bus and ring waveguide width 1100 nm. The grating coupler is design to have its maximum transmission at around the wavelength of 1550 nm.

Figure.4.2 except the coupling is through grating couplers. The waveguide width is 1100 nm, a single-mode propagation condition until 1500 nm wavelength. The gap of the ring resonator is chosen to be 400 nm so that the critical coupling appears around 1570 nm (center of the measurement band). To describe the resonance with enough measuring points (resolution 1 pm), the ring diameter is set to be 200 μm. The original transmittance (Figure.4.17)has been analyzed the same as Section.4.1.3 and the result is shown in Figure.4.18. A clear crossing of

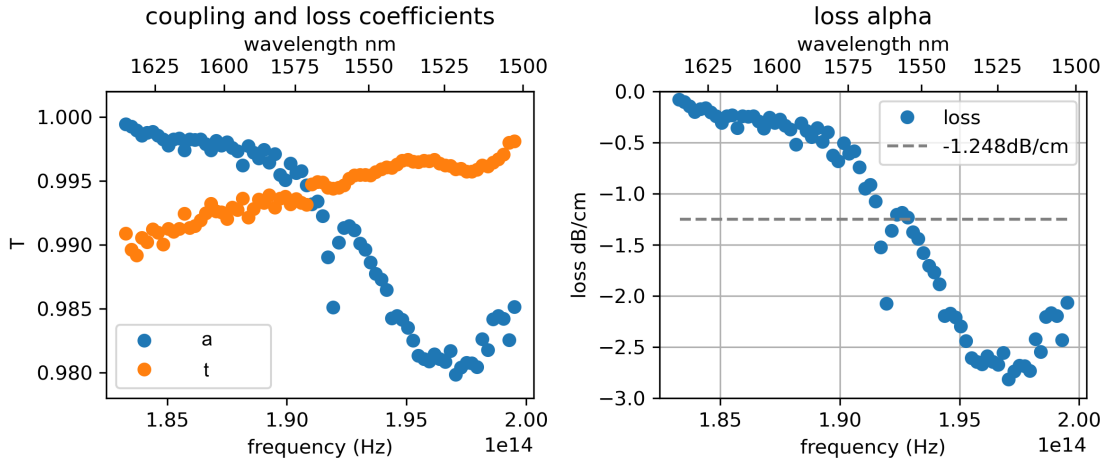

Fig. 4.18. Loss calculation by ring resonator. (a) The self-coupling t (in orange) and single-path amplitude transmission a (in blue) from a ring resonator with a width of 1100 nm, gap of 400 nm, and diameter 200 μm. (b) The loss is deduced from a. An absorption line appears around 1520 nm.

the self-coupling and loss coefficient is found at 1570 nm which is the condition of a critical coupling (Figure.4.18). The loss is about 0.3 dB/cm at 1600 nm wavelength. However, unlike the ring resonator fabricated by CEA-LETI in Figure.4.10, an absorption line appears at around 1520 nm causing a dramatic loss increasing to 3 dB/cm. This absorption line is due to the N-H bond and needs an N_2 annealing to remove it[9], [10].

After the annealing process described later in Section.4.2.3, the measurement carried out on the same ring resonator is shown in Figure.4.19. Only the measurement of wavelength 1500 nm to 1600 nm is shown here because the resonances above 1600 nm are difficult to fit. The curves of self-coupling and loss coefficient are distinguished by comparing with Figure.4.18(a) since the self-coupling coefficient should not change before and after annealing. The critical coupling

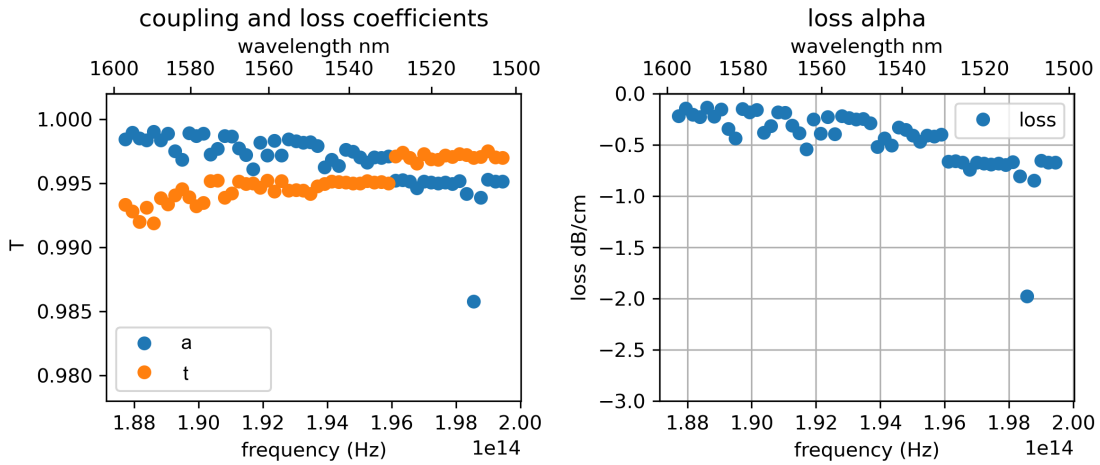

Fig. 4.19. Loss calculation by ring resonator after annealing. (a) The self-coupling t (in orange) and single-path amplitude transmission a (in blue) from the same ring resonator as in Figure.4.18 (b) The loss deduced from a.

wavelength moves to around 1530 nm because of the decrease in the loss. The coefficients a and t appears to be discontinuous between 1530 nm to 1500 nm. It may comes the stray light entering the detector[3]. From Figure.4.19(b), the loss at 1600 nm is about 0.2 dB/cm and the loss at 1500 nm is about 0.7 to 0.8 dB/cm.

4.2.3 . Annealing

One of the differences compared with the standard SOI platform process is the introduction of the annealing step. There are two main stages. First, a flash annealing in H_2 to smooth the side wall roughness[11]. Second, there is longer annealing in N_2 to break the N-H bond, which induces an absorption line at 1520 nm. The sample is first put in an H2 atmosphere at 1100 °C for one minute and then in an 1100 °C N_2 atmosphere for one hour. The characterizations are carried out after each step.

The direct characterization of sidewall roughness is difficult. The SEM can only see the sidewall roughness but cannot measure it. Alternatively, atomic force microscopy (AFM) can measure the roughness but only on a surface. Assuming that H_2 annealing affects both the sidewall and surface similarly, roughness measurements on the surface can indicate the sidewall roughness and its improvement. Before H_2 annealing, the surface is observed shown in Figure.4.20(a), of which the roughness (root mean square, RMS) is measured to be 0.7 nm. A large scan of the waveguide and the trenches is presented in Figure.4.20(b) where the micropillars can be clearly observed too. After the H_2 annealing, the same measurements show that the roughness RMS decreases from 0.7 nm to 0.4 nm, indicating a lower loss.

Q factor measurements (Equation.4.6, higher it is, lower the loss is) are also compared before and after H_2 annealing, shown in Figure.4.21. The sidewall roughness improvement decreases the propagation loss on every spectral bandwidth, thus resulting in a homogeneous improvement of the Q factor (see blue and green dots in Figure.4.21 for before and after). Nevertheless, Q factor still suffers a huge dip at 1520 nm wavelength due to the N-H bond that will be solved by N_2 annealing.

The sample is put in an 1100 °C N_2atmosphere for 1 hour; the Q factor measurement is shown in Figure.4.21 in orange. For the spectral range far away from the absorption line, Q factors

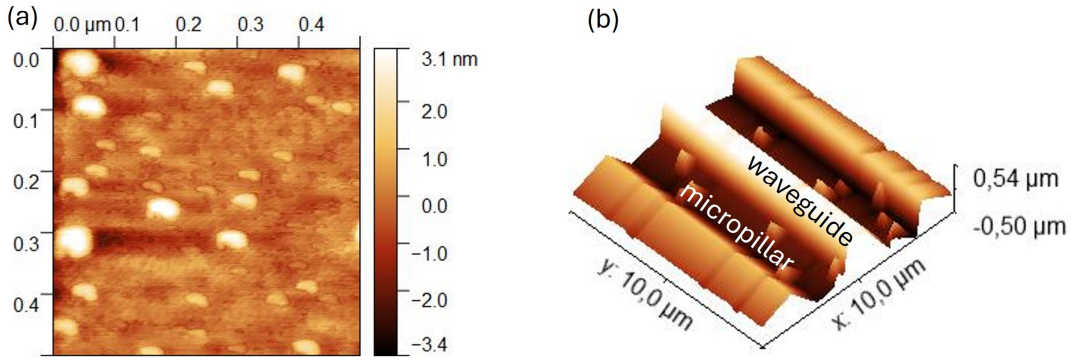

Fig. 4.20. The observation using atomic force microscopy (AFM) before H_2 annealing. (a) The roughness on the surface. (b) A 3D imaging of a waveguide and micropillars in the trench.

don't increase after the annealing (see 1600 nm wavelength). Indeed, the N_2 annealing does not improve the sidewall roughness. On the other hand, the dip at 1520 nm wavelength is filled up, meaning that the N-H absorption is largely removed. Despite the Q factor improvement, a residual absorption can still be seen at 1520 nm. A longer annealing time, like 3 hours, will be applied to remove the N-H bond thoroughly. This process has also been applied to the sample shown in Figure.4.19.

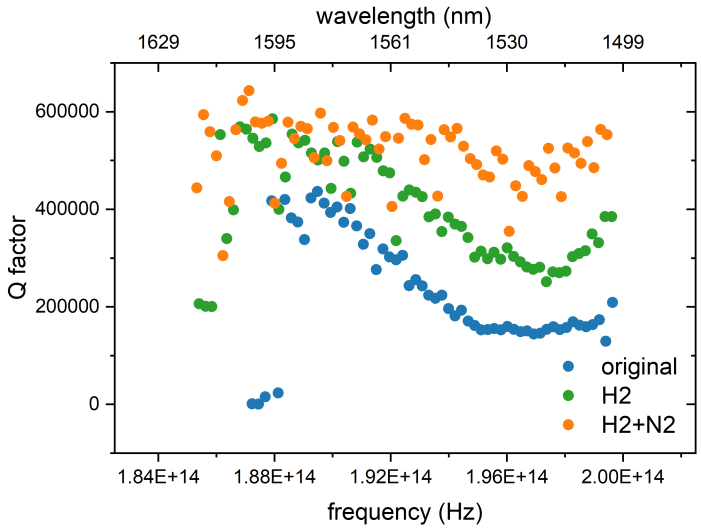

Fig. 4.21. Annealing effect on the Q factor of a ring resonator. The strip 700 nm height Si_3N_4 ring resonator has parameters showing as follows: width 1500 nm, diameter 200 μm, gap 300 nm.

A post-annealing step distinguishes this process from the standard SOI fabrication procedure. Although annealing only slightly enhances sidewall smoothness and eliminates the absorption line near the telecom C-band, further reduction of losses requires improving the etching process to eliminate micropillars, which are responsible for scattering light.

References

[1] B. J. Soller, D. K. Gifford, M. S. Wolfe, and M. E. Froggatt, "High resolution optical frequency domain reflectometry for characterization of components and assemblies", en, *Optics Express*, vol. 13, no. 2, p. 666, 2005, ISSN: 1094-4087. DOI: 10.1364/OPEX.13.000666.

[2] Q. Wilmart, S. Guerber, J. Faugier-Tovar, *et al.*, "A device library for the ultra-low loss Si3N4 platform", in *Silicon Photonics XVII*, G. T. Reed and A. P. Knights, Eds., San Francisco, United States: SPIE, 2022, p. 33, ISBN: 978-1-5106-4883-8 978-1-5106-4884-5. DOI: 10.1117/12.2606853.

[3] W. R. McKinnon, D. X. Xu, C. Storey, *et al.*, "Extracting coupling and loss coefficients from a ring resonator", en, *Optics Express*, vol. 17, no. 21, p. 18 971, 2009, ISSN: 1094-4087. DOI: 10.1364/OE.17.018971.

[4] W. Bogaerts, P. De Heyn, T. Van Vaerenbergh, *et al.*, "Silicon microring resonators", en, *Laser & Photonics Reviews*, vol. 6, no. 1, pp. 47–73, 2012, ISSN: 1863-8880, 1863-8899. DOI: 10.1002/lpor.201100017.

[5] R. Paschotta, *Free spectral range*, RP Photonics Encyclopedia. DOI: 10.61835/fx2"title="Thislinkwillreloadthecurrentpage..

[6] M. Sinclair, K. Gallacher, M. Sorel, *et al.*, "14 million Q factor Si $_3$ N $_4$ micro-ring resonator at 780 nm wavelength for chip-scale atomic systems", en, *Optics Express*, vol. 28, no. 3, p. 4010, 2020, ISSN: 1094-4087. DOI: 10.1364/OE.381224.

[7] D.-X. Xu, S. Janz, and P. Cheben, "Design of polarization-insensitive ring resonators in silicon-on-insulator using MMI couplers and cladding stress engineering", *IEEE Photonics Technology Letters*, vol. 18, no. 2, pp. 343–345, 2006, ISSN: 1041-1135. DOI: 10.1109/LPT.2005.861973.

[8] M. H. P. Pfeiffer, J. Liu, A. S. Raja, T. Morais, B. Ghadiani, and T. J. Kippenberg, "Ultra-smooth silicon nitride waveguides based on the Damascene reflow process: fabrication and loss origins", en, *Optica*, vol. 5, no. 7, p. 884, 2018, ISSN: 2334-2536. DOI: 10.1364/OPTICA.5.000884.

[9] K. Luke, A. Dutt, C. B. Poitras, and M. Lipson, "Overcoming Si_3n_4 film stress limitations for high quality factor ring resonators", en, *Optics Express*, vol. 21, no. 19, p. 22 829, 2013, ISSN: 1094-4087. DOI: 10.1364/OE.21.022829.

[10] S. Kim, K. Han, C. Wang, *et al.*, "Dispersion engineering and frequency comb generation in thin silicon nitride concentric microresonators", en, *Nature Communications*, vol. 8, no. 1, p. 372, 2017, ISSN: 2041-1723. DOI: 10.1038/s41467-017-00491-x.

[11] H. El Dirani, L. Youssef, C. Petit-Etienne, *et al.*, "Ultralow-loss tightly confining Si $_3$ N $_4$ waveguides and high-Q microresonators", en, *Optics Express*, vol. 27, no. 21, p. 30 726, 2019, ISSN: 1094-4087. DOI: 10.1364/OE.27.030726.

5 - Supercontinuum generation in width-invariant waveguides

Summary

5.1 . Waveguide design

As shown in Chapter.3, for SCG, one of the key parameters is the GVD of the waveguide. To correctly calculate the GVD of a given waveguide geometry, the material dispersion has to be first determined. For this purpose, ellipsometry measurements were performed on the Si_3N_4 waferAs a reminder, the wafer configuration is: 700 nm Si_3N_4 on 3 μm SiO_2 on Si substrate. The material dispersion curve of Si_3N_4 is shown in Figure.5.1. The characterization was carried out in the clean-room of C2N[1].

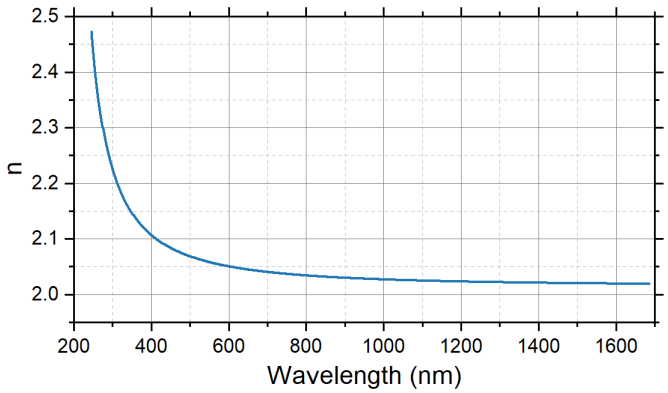

Fig. 5.1. Dispersion of 700 nm thick Si_3N_4. The deposition was performed through LPCVD by CEA LETI.

For the waveguide fabricated in the clean room of C2N, the side wall presents at an angle of 80°, as observed in Figure.4.16 which is represented here in Figure.5.2(a). The waveguide width is then defined as the width at the mid-height. The GVD simulations for the fundamental

[1]The measurement has been performed with the help of Xavier Lafosse, Luca Lovisolo and Sarra Salhi.

TE mode as a function of waveguide width changing from 600 nm to 1400 nm are shown in Figure.5.2(b). A maximum anomalous GVD about -450 $\mathrm{ps}^2/\mathrm{km}$ is obtained. The loss on the 1100 nm wide waveguide is shown in Figure.4.19, which is about 0.2 dB/cm at the wavelength of 1550 nm.
Figure.5.2(c) shows the width-invariant waveguide design. The waveguide has an Euler S bend in the lateral direction with an offset of 150 $\mu\mathrm{m}$. This offset avoids the scattering light from the input directly correctly from the output side. A taper is designed for input/output facets, continuously varying the waveguide width to 3 $\mu\mathrm{m}$. The sample is cleaved to obtain a clean facet for coupling. The waveguide length after cleave is measured to be 6 mm.

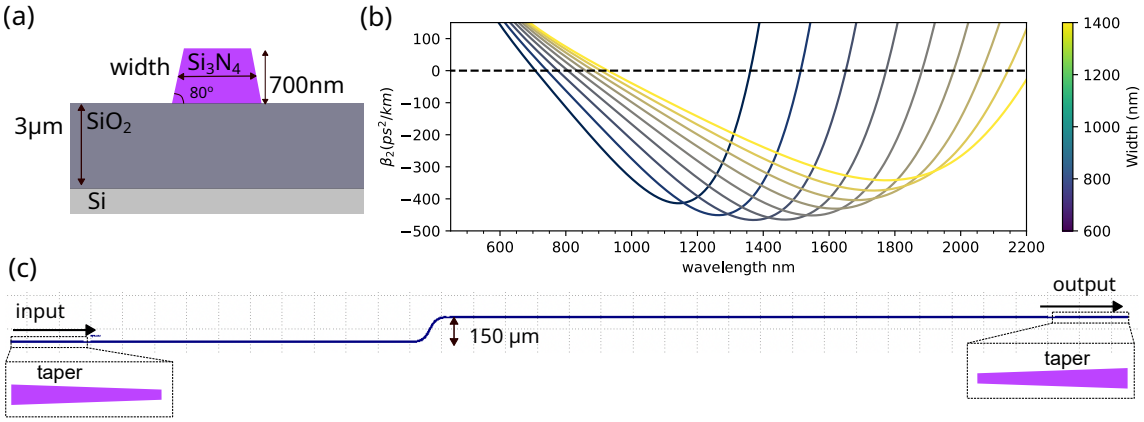

Fig. 5.2. Width-invariant Si_3N_4 waveguide fabricated in C2N clean room. (a) Cross-section the the waveguide. (b) GVD parameter β_2 for different waveguide widths from 600 nm to 1400 nm in fundamental TE mode. (c) The design of the 6-mm long waveguide. An Euler S bend is used to shift output from input.

5.2 . Experimental set-up

The schematic illustration[2]of the set-up for nonlinear spectral broadening is shown in Figure. 5.3. The pump laser (Monaco laser from Coherent)with 190-fs FWHM pulse duration and squared hyperbolic secant temporal shape centered at 1035 nm is followed by an optical parametric amplifier (OPA, OPERA-HP model from Light Conversion), leading to a large tunability from 0.65 $\mu\mathrm{m}$ to 14 $\mu\mathrm{m}$. The original out beam is in P polarisation (the electric field is vertical, equivalent to the TM polarisation in a guiding mode) with a repetition rate of 1 MHz. The laser beam then goes through a set of optical densities, from low to high attenuation coefficient, to decrease the power. The continuously variable neutral density plate is also added to control the power to an exact value. The polarization can be turned to S polarization (the electric field is horizontal, equivalent to TE in a guiding mode) with the polarisation rotator, which is composed of a set of mirrors.
The coupling system is realized by two optical objectives installed on the piezo translation stages. The collection objective can be replaced by a Cassegrain objective, which is made of the mirror to avoid chromatism. On the top, a microscope with a camera helps to observe the sample surface.
After the spectral broadening is collected by the objective, the light beam can be sent to a camera, a spectrometer for visible and NIR, and a monochromator for IR. The camera observes the mode at the output facet of the tested waveguide. For the spectral broadening under 1000

nm wavelength, the light beam is coupled to a fiber and measured by the visible and NIR spectrometer. The fiber can also be connected to a power meter to monitor the transmission. For the spectral broadening above 1000 nm, a parabolic mirror focuses the light beam on a monochromator, from which the spectrum is dispersed and measured. The monochromator works with the lock-in amplifier and the chopper to obtain a high signal-to-noise ratio.

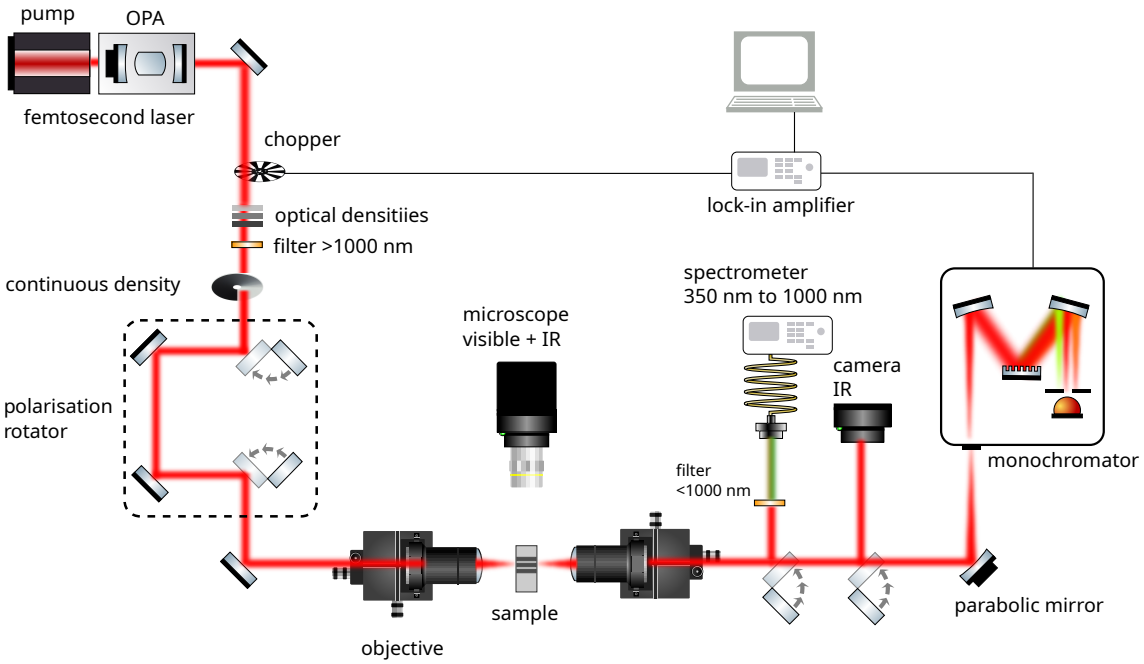

Fig. 5.3. Nonlinear characterization set-up. The laser beam from the tunable 190-fs laser first passes through optical density filters. The polarization of the beam can be selected between S and P polarizations using a mirror polarization rotator. The laser is coupled into and collected from the sample waveguide using optical objectives. The output beam is visible through an IR camera, while two spectrometers measure the spectrum according to their respective wavelength ranges.

Inside the monochromator, a grating disperses light of different wavelengths in different directions. Reflected again by a mirror, the light is focused on an InGaAs (IGA) detector through a slit for wavelength selection. A detailed response of the grating and the detector to different wavelengths is shown in Figure.5.4 offered by the manufacturer (details can be found in Appendix). The monochromator has two apertures. The one at the entry of the monochromator controls the total energy entering into the system, which needs to be controlled not to saturate the detector. The other one is located before the detector, which defines the wavelength resolution of the measurement.

5.3 . Spectral broadening characterization

The nonlinear characterization is implemented on the waveguide, which has a width of 600 nm, which is the only width available for now. The cross-section is shown in Figure.5.2(a) and the GVD curve is re-plotted in Figure.5.7 in the dotted blue line. The pump wavelength is set to 1310 nm, selected for the following reasons: 1310 nm is near the zero-dispersion

[2]The optics components in Figure.5.3 is modified from ComponentLibrary contributed by Alvise Vianello and Alexander Franzen with the 3.0 versions of all CC licenses. https://gitlab.com/amv213/componentlibrary

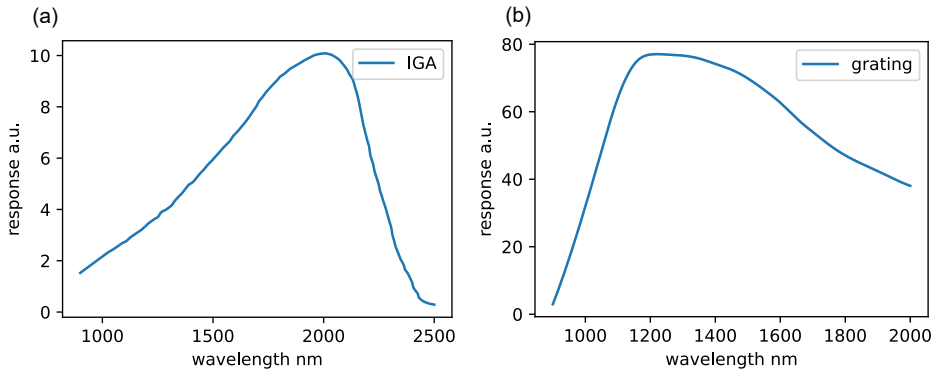

Fig. 5.4. Response function of the InGaAs detector and grating inside the monochromator, respectively. The responses don't have unity.

wavelength (ZDW) at 1360 nm, resulting in $\beta_2 = -200, \mathrm{ps}^2/\mathrm{km}$ and $\beta_3 = -2.8, \mathrm{ps}^3/\mathrm{km}$, assuming the fabricated sample has the same cross-section as designed. The significant value of β_3 at this wavelength promotes soliton fission and DW generation at longer wavelengths. As will be demonstrated later, the DW is generated far from the pump wavelength, approaching the limit of the guided mode. For SC measurements, the first step is finding the coupling loss to estimate the coupled power inside the waveguide correctly.

5.3.1 . Coupling efficiency estimation

For the samples fabricated in CEA-LETI, the input/output facets are usually equipped with inverse tapers with a good length and width variation definition, resulting in an equivalent high coupling efficiency for both facets (4 dB/facet). However, for the samples made in the C2N clean room, the waveguide facets are cleaved and the taper is not inversed (see Figure.5.2(c). Thus, the facet quality can differ for input and output, making the coupling efficiency estimation more challenging. Therefore, we consider the mode overlap between the objective focus and input facet mode. The waveguide width at the cleaving is estimated to be 900 nm. The fundamental TE mode field amplitude is shown in Figure.5.5(a). For the spatial Gaussian mode, the beam waist (radius) at the focus for a given numerical aperture (NA) is expressed as Equation.5.1.

$$\omega_0 = \frac{\lambda}{2\pi \cdot NA} \tag{5.1}$$

NA is calculated as $NA = \frac{1}{2}\frac{D}{f} = 0.13$, where the initial beam diameter D is measured as 2 mm, and the objective focal length is 7.6 mm. The Gaussian mode field amplitude distribution with a given beam waist $\omega_0 = 1.6\,\mu\mathrm{m}$ is shown in Equation.5.2

$$G(x, y) = \exp(-\frac{x^2 + y^2}{\omega_0^2}) \tag{5.2}$$

At the beam waist ω_0, the optical field amplitude decreases to e^{-1} of its value in the center, while the intensity decreases to e^{-2} compared to the center. The corresponding field amplitude distribution is shown in Figure.5.5(b). The coupling efficiency concerning the optical power is shown in Equation.5.3:

$$\eta = \frac{|\int E_1^* E_2 \cdot dS|^2}{\int |E_1|^2 \cdot dS \int |E_2|^2 \cdot dS} \tag{5.3}$$

where E_1 and E_2 are the complex electric fields, referring to the mode in the waveguide and the mode at the optical objective focus.

Fresnel reflection also serves as an extra loss to the coupling efficiency. The reflection can be expressed as Equation.5.4

$$R = |\frac{1 - n_{eff}}{1 + n_{eff}}|^2 \tag{5.4}$$

where n_{eff} corresponds to the effective index of the mode at the waveguide input facet. The n_{eff} here equals to 1.8.
Therefore, the coupling coefficient is estimated to be -7.4 dB (20%), taking into account the Fresnel reflection and mode overlap between the fundamental TE mode at 1310 nm wavelength and the Gaussian mode at the objective focus.

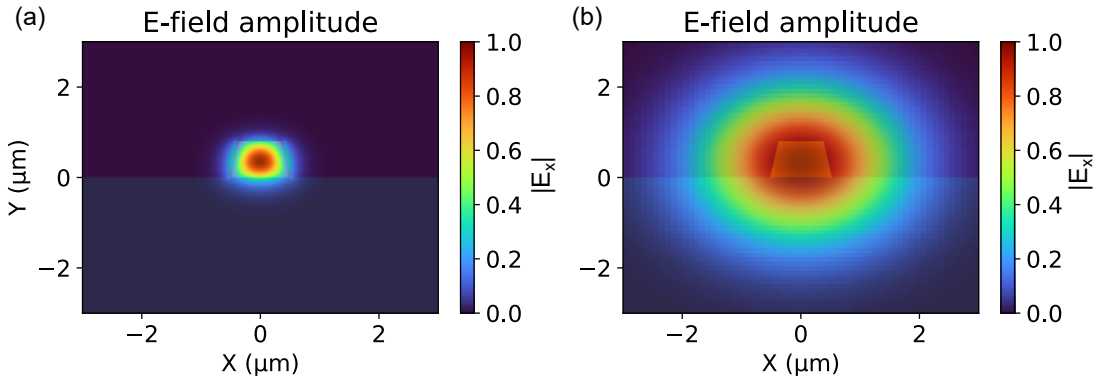

Fig. 5.5. Optical field amplitude distribution of TE mode. The waveguide geometry is also overlapped with the mode distribution. (a) The $|E_x|$ of the mode at the end of the taper which has a cross-section of 900 nm $\times$ 700 nm. (b) The $|E_x|$ of the Gaussian distribution mode in the focal plane of the optical objective, the beam waist w_0 of which is equal to 1.6 μm.

5.3.2 . Spectral broadening

The spectral broadening is measured by a monochromator from 1000 nm to 2000 nm. The originally measured spectra are corrected and normalized by the grating and detector response functions shown in Figure.5.4. Average powers are measured before the optical objective, presented with the measured spectral broadening shown in Figure.5.8(a). From 0.5 mW, 1 mW, to 2 mW, the pump power is doubled each time. Compared to the input pump spectrum, the initial spectral broadening is primarily due to SPM, as the broadening occurs around the pump wavelength (see Figure 5.8(a), green curve at 0.5 mW). Although not immediately obvious, signs of DW generation appear near 1650 nm in the waveguide. As the average power increases to 1 mW, a significant energy transfer to the DW is observed, with the wavelength also red-shifting. With further increases in average power, even stronger DW generation occurs, where the spectral density is only about 10 dB lower than the pump. This non-homogeneous spectral broadening, with a preference for specific wavelengths, is typical in waveguides where the GVD curve exhibits significant higher-order dispersion (HOD), such as β_3.

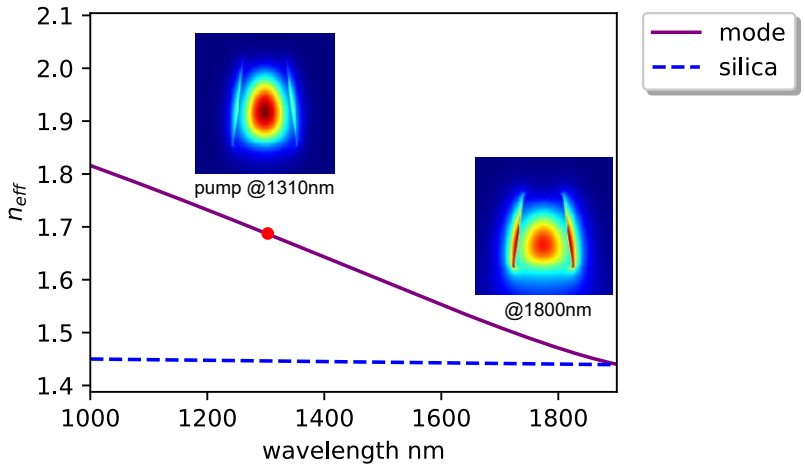

Fig. 5.6. Effective index n_{eff} of the fundamental TE mode in a 650 nm $\times$ 700 nm Si_3N_4 waveguide (purple curve). The dashed blue line represents the refractive index of silica. Additionally, the mode intensity distribution is shown for the pump wavelength of 1310 nm and at the limit of the propagation wavelength, which is 1800 nm.

The long side of the spectral broadening has reached the wavelength of 1800 nm. From mode simulation using Lumerical FDE (Figure.5.8(a)), the mode is no longer tightly confined inside the waveguide compared with the mode at 1310 nm. Instead, the highest field intensity appears on the side wall. In Figure 5.6, the effective refractive index (n_{eff}) of the guided fundamental TE mode is compared with the refractive index of silica, which serves as the cladding. It can be observed that for wavelengths above 1800 nm, the mode tends to leak in this waveguide geometry. The GVD at 1800 nm is in a strong normal region which has its β_2 equals to $11500\,\mathrm{ps}^2/\mathrm{km}$. The absolute value is about two orders of magnitude of that at the pump.
Simulations of NLSE explained in Section.3.3 have also been carried out to compare with the experimental measurements. Although the waveguide is designed with its width of 600 nm (see Figure.5.2), the best GVD curve that is found to agree with the measured spectral broadening is that from a waveguide width 650 nm. The difference may come from the fabrication variation. Therefore, the simulation results are based on the waveguide with a width of 650 nm. The

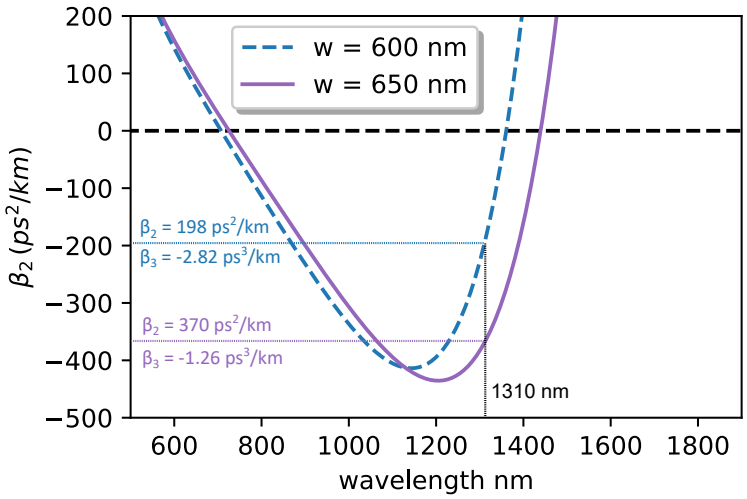

Fig. 5.7. GVD curve of the tested waveguide. The designed waveguide cross-section of 600 nm × 700 nm is represented by the dashed blue curve. The waveguide cross-section that yields simulation results consistent with the spectral broadening measurements is shown in the purple curve, with a width of 650 nm. The values of β_2 and β_3 at the pump wavelength of 1310 nm for both waveguide geometries are also indicated.

nonlinear index of Si_3N_4 is set to be $n_{2,Si_3N_4} = 2.4 \times 10^{-19}\,\mathrm{m^2/W}$. The waveguide fabrication process follows the same as what is described in Section.4.2 from Chapter.4. According to the loss measured in Section.4.2, the total propagation loss in this 6-mm long waveguide is estimated to be lower than 0.5 dB. Therefore, the propagation loss is neglected in NLSE simulations. The NLSE simulation results are shown in Figure.5.8(b). The best pump peak power to align the simulation results with measurements are 150 W, 300 W, and 600 W. The DW generation in SCG aligns well with experimental measurements, except for the lower energy conversion efficiency. However, the broadening in the blue range of the spectrum in simulation is wider than measurements. One possible reason is the lower response for both the grating and the detector when the wavelength approaches 1000 nm. From Figure.5.4, a drastic drop of response can be found around 1000 nm wavelength, thus not detecting the generated continuum.
The DW phase matching conditions are shown in Figure.5.8(c). The nonlinear term $\frac{\gamma P_s}{2}$ is also considered in Equation.3.23, thus resulting in a difference in phase-matching wavelength according to the pump peak power. It can be found that the phase-matched DW wavelength is only slightly red shifting when increasing the pump power, revealing that the phase-matching condition is still dominated by waveguide dispersion.

In experimental measurements, only the average power is measured, while simulations require the peak power. The average and peak power are related by considering the laser repetition rate. The temporal pulse shape also needs to be considered, as different pulse shapes contribute differently over time. Based on the laser manufacturer's specifications, we assume a squared hyperbolic secant pulse shape (Equation 3.10) with a repetition rate of 1 MHz. By comparing the measured average powers and the peak powers used in simulations, the coupling efficiency estimated is -11.9 dB. It is higher than the -7.4 dB estimated by mode overlap. Possible reasons for the higher observed loss include: the pump laser beam may not be perfectly aligned with the optical objective's axis, leading to aberrations at the focus and an increase in mode size; the sample might be tilted with respect to the horizontal plane, resulting in an inclined incident angle; and light may be scattered at the coupling facet, reducing the coupling efficiency.

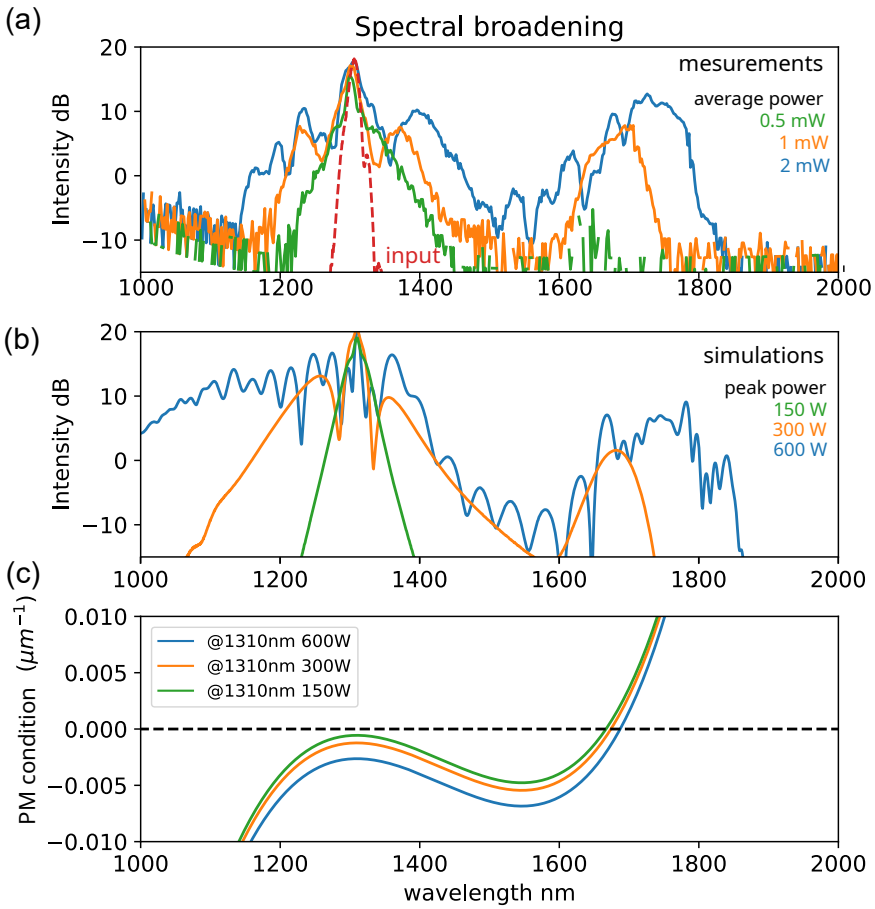

Fig. 5.8. Spectral broadening and DW phase-matching condition in a 6mm-long Si_3N_4 waveguide. (a) Experimental measurements with the measured average pump power. The red dashed line shows in the initial pump spectrum. (b) Simulation results with the estimated pump peak power. (c) Phase-matching conditions (Equation.3.23) for DW generation with nonlinear phase term $\gamma P_s/2$ included. The pump is located at 1310 nm wavelength.

5.4 . Temporal coherence

An analysis of temporal coherence has also been carried out. The parameters used in the simulation is shown in Table.5.1, where the variance that characterizes the RIN is given as 0.97% according the the laser manufacturer. By simulating the spectral broadening by adding RIN and OPPM noise as described in Section.3.6, 20 independent simulations are used for mutual coherence $|g_{12}|$ calculation, shown in Figure.5.9. In Figure.5.9(a), the black curve shows the

Table 5.1. Simulation parameters for temporal coherence analysis.

center wavelength	simulation window	sampling points	RIN variance
$\lambda_0 = 1310\,nm$	$T_{width} = 12.5\,ps$	m = 2^{14}	$r = 0.97\%$

averaged spectral broadening from these 20 simulations with pump peak power 300 W (the curve is also used in Figure.5.8(b)). Behind the black curve, each spectral simulation is presented in different colors, mostly well-overlapped. This indicates that the pulse goes through a similar nonlinear process regardless of the existence of noise. As a result, the temporal coherence

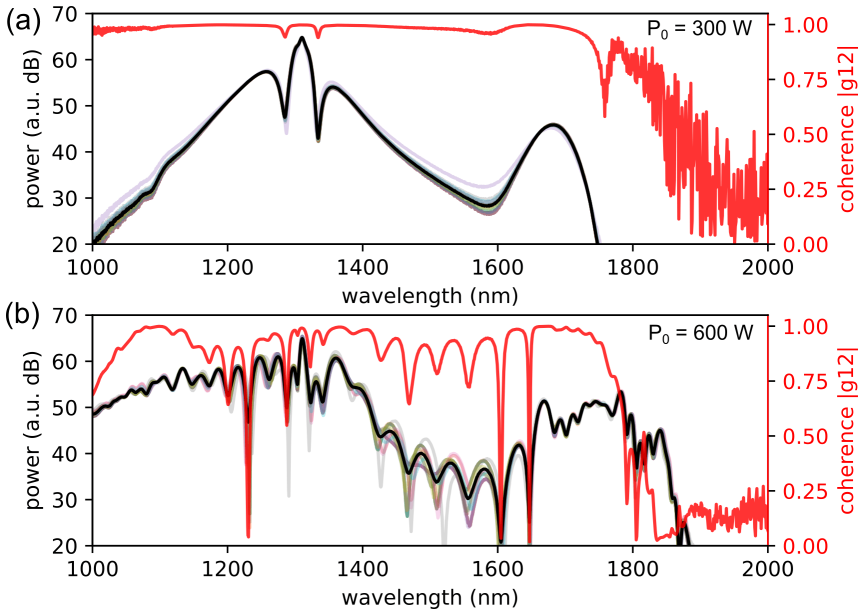

Fig. 5.9. Temporal coherence based on simulations added with noise. (a) Black curve: averaged spectral broadening on 20 independent simulations. Each simulation result is also superposed with different colors. Red curve: the mutual coherence $|g_{12}|$. The pump peak power is 300 W. (b) The same as in (a) except that the peak power is 600 W.

remains very high from the pump to the DW. On the other hand, for a stronger pump power of 600 W shown in Figure.5.9, the temporal coherence decreases. The highest coherence remains at the pump and DW wavelength. The soliton number for the pump of 300 W and 600 W are $N = 5$ and 7, respectively. For the pump pulses that are limited by OPPM noise (shot noise) with the same pulse duration, the decoherence of the SCG depends largely on the soliton number[1]. A higher soliton number will strengthen noise amplification through modulation instability, strongly disturbing the soliton evolution from pulse to pulse. Therefore, for a pump peak power at 300 W, the lower soliton number ensures a better coherence.
A general guideline for good coherence is to limit soliton number $N < 10$[1], which explains why our spectrum coherences remain generally high. Furthermore, good coherence of SC over 1 octave is more practical with a shorter pulse $< 100\,fs$. For the 190-fs laser in our setup, an on-chip pulse compressor is then required to obtain the sub-100-fs pulse.

5.5 . Conclusion

In this chapter, a comprehensive study of supercontinuum generation (SCG) in a width-invariant waveguide has been conducted. The waveguide was fabricated in the cleanroom of C2N using a Si_3N_4 wafer provided by CEA-LETI.
We began by characterizing the material dispersion curve of 700-nm thick Si_3N_4 through ellipsometry. Following this, the waveguide dispersions were simulated based on the measured waveguide cross-sectional geometry and material dispersion. The setup used for nonlinear spectral broadening characterization was then presented, including the coupling mechanism from optical objectives to integrated waveguides, along with an estimation of the coupling efficiency. Finally, the spectrum broadening was both measured and simulated as a function of pump power, with an investigation into the temporal coherence.

While supercontinuum generation in width-invariant waveguides has been extensively studied, from waveguide design and spectral broadening to temporal coherence, this chapter lays the groundwork for understanding more complex SCG processes in width-variant waveguides.

References

[1] J. M. Dudley, G. Genty, and S. Coen, "Supercontinuum generation in photonic crystal fiber", en, *Reviews of Modern Physics*, vol. 78, no. 4, pp. 1135–1184, 2006, ISSN: 0034-6861, 1539-0756. DOI: 10.1103/RevModPhys.78.1135.

6 - Quasi-phase-matched supercontinuum generation

Summary

In the previous Chapter.5, the DW generation in a width-invariant waveguide is based on its phase-matching (PM) condition. Because the PM condition is tightly bound with the waveguide dispersion, the spectral position of the DW is defined by each waveguide cross-section. The lack of DW wavelength tunability is a drawback for applications that need relatively high spectral intensity in selective spectral ranges (ex., multi-color imaging[1] and stimulated emission depletion (STED) microscopy[2]). Furthermore, the phase-matching wavelength may locate too far away unreachable from soliton or even the material's transparent windows, which limits the spectrum broadening[3], [4].

Numerous methods have been proposed to overcome these problems including actively tuning DW by introducing pressure gradient[5], temperature variation[6], and create new phase-matching wavelengths by leveraging gas ionization[7] and phase-matching to higher order transverse mode[8] . However, these methods either require specific fabrication techniques that only works for gas-filed or liquid-cored photonic crystal fiber, or harm the spatial coherence.

Meanwhile, the implementation of the quasi phase-matching (QPM) approach, achieved through the modulation of dispersion along the waveguide propagation, facilitates the generation of multiple DWs[9]. Diverging from the established QPM scheme in $\chi^{(2)}$ material, which typically involves periodic changes in nonlinear polarizability for efficient harmonic generation[10], the QPM employed for DW generation introduces a significantly longer periodicity. This extended periodicity serves to reconcile the phase mismatch between solitons and DWs. We define the quasi-phase-matched supercontinuum generation (QPM-SCG) as the supercontinuum with DWs generation based on their QPM conditions (QPM-DWs). The waveguide that enables QPM-SCG is later called QPM waveguide.

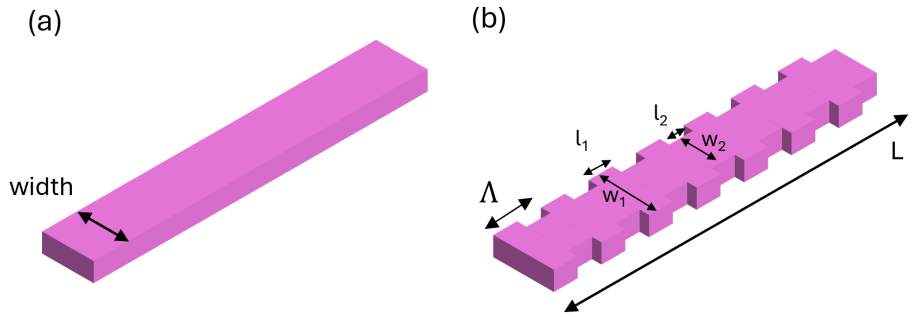

Fig. 6.1. Illustration for QPM waveguide. For simplicity, only the waveguide cores are presented. (a) The width-variant waveguide. (b) The QPM waveguide.

6.1 . Quasi-phase-matching condition

If a waveguide has periodical altering waveguide width w_1 and w_2 along the propagation direction as shown in Figure.6.1(b), it introduces GVD modulation for a propagating pulse. The GVD modulation introduces an extra term to the PM condition for DW in Equation.3.23, giving the following QPM condition.

$$\beta_{eff}(\omega) - \beta_{eff}(\omega_s) - v_{g,eff}^{-1}(\omega - \omega_s) - \frac{\gamma P_s}{2} = \frac{2\pi}{\Lambda} m \tag{6.1}$$

The right side of Equation.6.1 shows the additional momentum where Λ is the GVD modulation period and m is the order number. Although GVD variation is not necessarily a monotonic function with width variation, their modulations usually share the same period.
Because of the modulation, the waveguide dispersion β is no longer uniform along the propagation as the width-invariant waveguide. Therefore, an effective effect has to be considered using β_{eff} and $v_{g,eff}$ in Equation.6.1. For a perfectly periodical waveguide, β_{eff}, $v_{g,eff}$ and $\beta_{2,eff}$ can be defined as:

$$\beta_{eff} = \frac{l_1 \cdot \beta_{w_1} + l_2 \cdot \beta_{w_2}}{l_1 + l_2} \tag{6.2}$$

$$v_{g,eff} = \frac{l_1 \cdot v_{g,w_1} + l_2 \cdot v_{g,w_2}}{l_1 + l_2} \tag{6.3}$$

$$\beta_{2,eff} = \frac{l_1 \cdot \beta_{2,w_1} + l_2 \cdot \beta_{2,w_2}}{l_1 + l_2} \tag{6.4}$$

l_1 and l_2 are the lengths of waveguide width w_1 and w_2 in one period Λ, respectively. The normal and anomalous dispersion ranges are also defined by effective GVD $\beta_{2,eff}$.
At low pump power, similar to the width-invariant waveguide, the nonlinear terms $k_{nl} = \frac{\gamma P_s}{2}$ can be neglected; thus, the QPM condition is determined by the waveguide dispersion and its period.
A schematic view of the QPM-SCG generation is shown in Figure.6.2, which can be described as follows. Once the pump laser pulse is sent into the anomalous GVD region of the QPM waveguide defined by $\beta_{2,eff}$, it undergoes pulse evolution under the effective condition of β_{eff}, resulting in a soliton formation. When the soliton is perturbed by HOD, multiple QPM-DWs are generated where QPM conditions are fulfilled, creating the QPM-SCG. For simplicity, the QPM waveguide is firstly considered as brute periodic concatenation of two different waveguide widths. It has to been noticed that in real QPM waveguide, smooth transition has to be applied

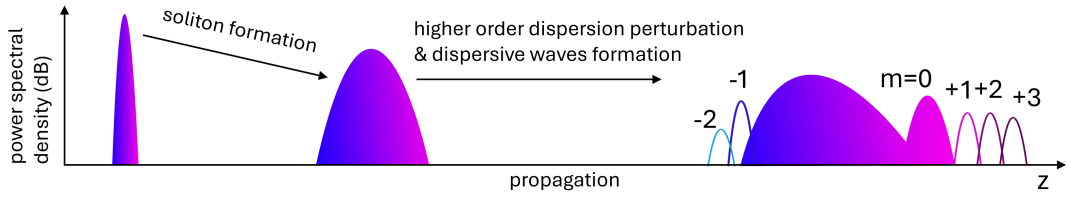

Fig. 6.2. Concept of quasi-phase-matched dispersive waves generation in Si_3N_4 waveguide with group velocity dispersion modulation. QPM-DWs formation process: A pump creates a soliton which generates QPM-DWs at wavelengths defined by QPM conditions after HOD perturbation. QPM-DWs are denoted by their orders m.

in between to avoid loss from mode overlap.

6.2 . Waveguide design principle

6.2.1 . Periodicity

The periodicity induced in a waveguide is important for QPM-DW, which is different for different fiber and integrated platforms. The first demonstration in dispersion oscillating fiber uses a meter scale periodicity. The periodicity also determines the QPM process is intermodal or intramodal. Hickstein et al. have involved DWs in higher-order transverse optical modes[11] in a photonic waveguide.

We focus specifically on the periodicity for intramodal QPM, meaning that QPM-DWs and the pump propagate in fundamental mode. The reasons are as follows. First, the fundamental mode is the broadest guiding mode for a waveguide, thus ensuring the largest bandwidth that QPM can be applied. Second, all fundamental mode keeps good spatial coherence, which is important for many applications and is also easy to do off-chip coupling. Third, intramodal QPM doesn't need extra mode conversion consideration, which facilitates nonlinear simulation modeling.

In one period $\Lambda = l_1 + l_2$, we define duty cycle as the percentage of the length of the wider width segment to Λ as Equation.6.5

$$DC = \frac{l_1}{\Lambda} \tag{6.5}$$

For a given waveguide width w_1 and w_2, changing the DC defines the effective propagation constant β_{eff} and the second-order dispersion $\beta_{2,\text{eff}}$. However, β_{eff} and $\beta_{2,\text{eff}}$ cannot be determined without knowing the exact values of w_1, w_2, the wavelength λ, and the duty cycle. Nevertheless, it is always possible to find a waveguide cross-sectional geometry that results in a similar shape for β and β_2 as those of β_{eff} and $\beta_{2,\text{eff}}$. For clarity, we choose a waveguide width of 1700 nm for the following explanations, applying both to the buried Si_3N_4 waveguide fabricated by CEA-LETI and the strip Si_3N_4 waveguide fabricated at C2N. The β_2 of these waveguides on both platforms is shown in Figure 6.3 (a, b). Notably, the strip Si_3N_4 platform shows a much wider and deeper anomalous dispersion (AD) region. Their intrinsic PM wavelengths are indicated by dark blue dots, based on their specific PM conditions.

If a QPM term $\frac{2\pi}{\Lambda}m$ is introduced, with a period $\Lambda = 0.628$ mm, additional dashed lines are included in Figure 6.3(c). Each dashed line represents a different order m. The graphic solu-

tion for QPM is the intersection of the phase-mismatch curve with the QPM terms, which are denoted by vertical green lines in Figure 6.3(c). This figure illustrates the QPM solutions for the buried Si_3N_4 platform.

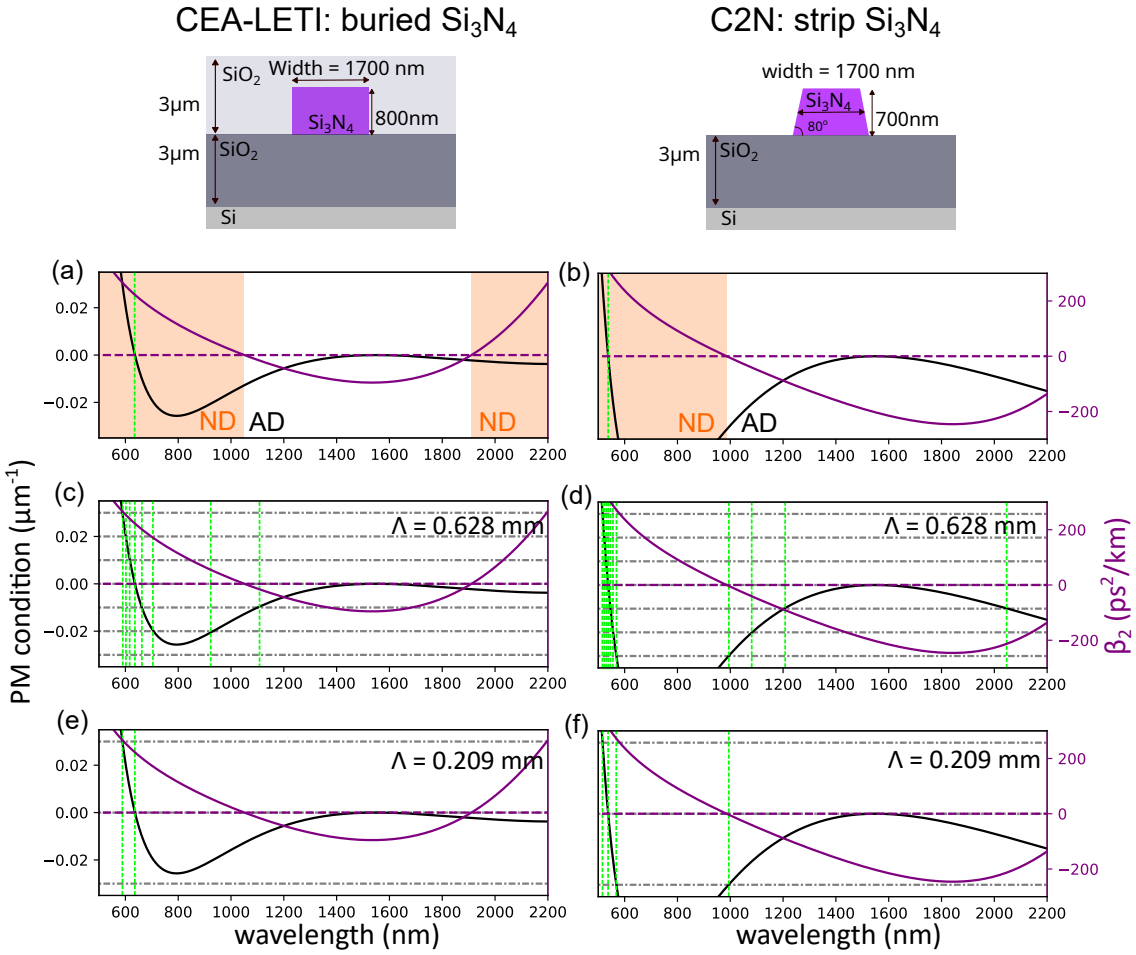

Fig. 6.3. QPM periodicity design in Si_3N_4 platform. Left column: 800 nm thickness with thick up-cladding. Right column: 700 nm thick strip waveguide. (a) GVD and DW phase mismatch at waveguide width 1700 nm. Pump wavelength is at 1550 nm. ND and AD are for normal dispersion and anomalous dispersion, respectively. (b) QPM graphic solutions when QPM term $\frac{2\pi}{\Lambda} = 0.01\,\mu m^{-1}$, where $\Lambda = 0.628\,mm$. (c) QPM graphic solutions when QPM term $\frac{2\pi}{\Lambda} = 0.03\,\mu m^{-1}$, where $\Lambda = 0.209\,mm$.

As the period Λ decreases, the spacing between the QPM terms increases. This means that the possible QPM solutions are located farther apart. Figure 6.3(e) demonstrates the QPM solution in the buried Si_3N_4 waveguide when the period $\Lambda = 0.209\,\text{mm}$. Significantly fewer QPM solutions are found. If the period becomes small enough, the QPM terms will be so far apart that no graphical solution can be found within a reasonable spectral range. In this case, the QPM waveguide behaves like a standard waveguide, only supporting intrinsic DW phase-matching wavelengths.

The QPM term $\frac{2\pi}{\Lambda}m$ is also introduced for the strip Si_3N_4 platform, with periods $\Lambda = 0.628\,\text{mm}$ and $0.209\,\text{mm}$, respectively, shown in Figure 6.3(d, f). Compared to the buried Si_3N_4 platform, the strip Si_3N_4 platform supports more QPM solutions. This is because its group velocity dispersion (GVD) curve has a deeper anomalous dispersion region, resulting in a steeper phase

mismatch curve, which allows for more QPM solutions.
Therefore, the appropriate periodicity Λ needed to enable a reasonable number of QPM solutions varies between platforms, depending on the shape of the GVD curve. For a GVD curve close to zero, Λ should be larger. For a GVD curve with deep anomalous dispersion, Λ should be smaller. As Λ continues to decrease, QPM solutions for fundamental DWs will eventually disappear, although higher-order DWs can still be coupled [11]. Additionally, to ensure a smooth mode transition between different cross-sectional geometries without being affected by Bragg reflection or scattering loss, the period Λ must be significantly larger than the wavelength scale.

In conclusion, the periodicity Λ that is suitable for QPM solution depends on waveguide dispersion. A practical value in the Si_3N_4 platform is from hundreds of micrometers to millimeter scale. This millimeter scale periodicity is much larger than other periodical structure (e.g. Bragg grating[12] and periodical poling crystal[13]) in integrated platform. Therefore, this QPM is technologically addressable in the modern semiconductor fabrication.

6.2.2 . Effective dispersion validation

The utilisation of β_{eff} is an intuitive way to describe the effective dispersion effective to the soliton dynamics. Indeed, it is noteworthy that it provides an accurate representation of the average dispersion property of the QPM waveguide, concerning nonlinear effects, particularly when the nonlinear phase change within one period of dispersion modulation is relatively small ($L_{NL} > \Lambda$). Because L_{NL} is inversely proportional to peak power as shown in Equation.3.9, the pump peak power needs to be limited according to Λ. When L_{NL} is approaching Λ or even beyond Λ during the propagation (ex. when the pump undergoes SSC), the effective dispersion defined by Equation.6.1 suffers a gradual deterioration in its representation of average dispersion. In this case, QPM-DWs still exist but the true wavelength position of QPM-DWs may diverge from prediction based on effective dispersion, necessitating a complete GNLSE simulation.

6.3 . Characterization in one ZDW system

We first consider the QPM-SCG in a one zero-dipersion wavelength (ZDW) system, meaning that the pump wavelength is close to one ZDW and the pump power is not high enough to make the spectral broadening reach the second ZDW. In one ZDW system, the soliton number N required for DW generation is lower, resulting in a narrower broadening but with a clearly nonlinear dynamics.

6.3.1 . Waveguide design

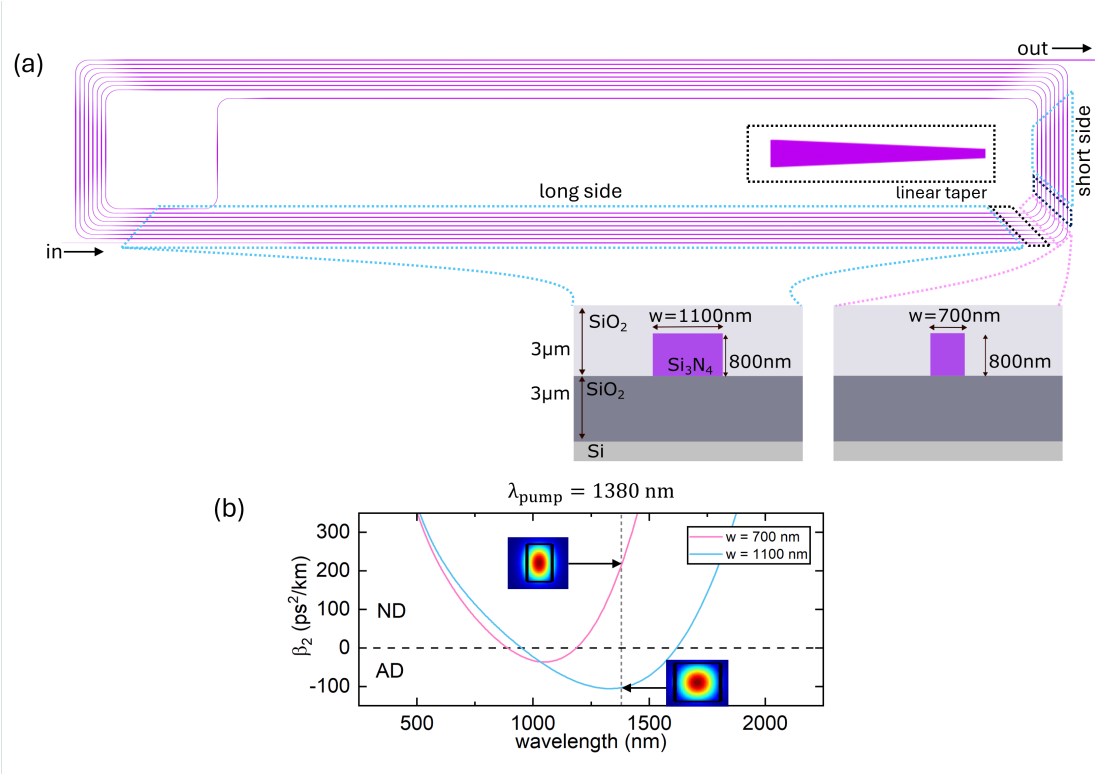

Fig. 6.4. QPM spiral waveguide. (a) Straight waveguides at short and long sides have a width of w = 1100 nm, while waveguide in the bend has a width of w = 700 nm. Linear tapers allow optical mode transition between both waveguide widths. The waveguide's cross sections are shown in the bottom-right corner. (b) GVD curve for both waveguide geometries w = 1100 nm and 700 nm. The corresponding TE mode intensity distributions are also shown at pump wavelength 1380 nm.

A schematic view of the QPM Si_3N_4 waveguide is reported in Figure.6.4. The 800-nm-thick and 4.3-cm-long spiral waveguide was fabricated at CEA LETI, France, using twist-and-grow LPCVD deposition technique[14], [15]. Linear and nonlinear refractive indices are 1.98 at a wavelength of 1380 nm measured by ellipsometry and 2.4×10^{-19} m^2/W according to literature[16], respectively. The waveguide consists of a periodic alteration in width, ranging from 1100 nm to 700 nm along the direction of propagation (longitudinal direction). This configuration, illustrated in Figure.6.4(a), incorporates linear tapers to facilitate mode transitions between varying widths. The 4.3 cm long waveguide is configured in a spiral pattern to minimize the device footprint, resulting in a compact size of 4 mm $\times$ 0.5 mm. The width of the waveguide is set at 1100 nm in the straight sections (short and long sides reported in Figure 1. b), tapering to 700 nm in the bending regions. The propagation loss is as low as 0.3 dB/cm

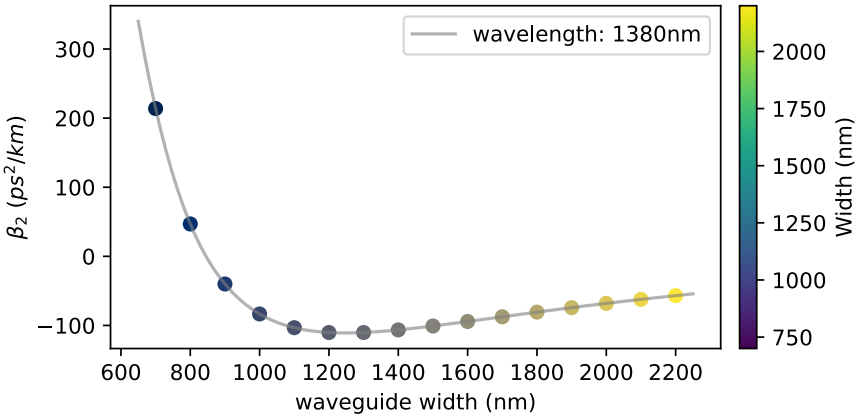

Fig. 6.5. GVD in the function of waveguide width at wavelength 1380 nm. The Si_3N_4 waveguide height is 800 nm buried in 3 μm SiO_2 layer.

measured by optical frequency domain reflectometry[17] (see Chapter.4).
The geometry of the waveguide exhibits a substantial GVD modulation depth of 300 ps^2km^{-1} from anomalous GVD ($w = 1100$ nm) to normal GVD ($w = 700$ nm) (Figure.6.4(b)), thereby instigating a strong QPM effect at a pump wavelength of 1380 nm. The GVD in the function of waveguide width is shown in Figure.6.5, where the GVD is found to be monotonically decreasing with waveguide width, from which the GVD modulation can be calculated from width modulation. The reported GVD modulation is two orders of magnitude higher than typically obtained in single mode fiber adjusting the core diameter[18]. Indeed, given the strong optical mode confinement in the 800-nm-thick Si_3N_4 waveguide, a variation of its width induces a significant change in the mode field distribution, leading to a substantial modification of the waveguide dispersion (Figure.6.6). Noticeably, this GVD modulation depth has surpassed the maximum dispersion in AD and inevitably enters ND. Therefore, to keep the average dispersion anomalous for soliton formation, a high duty cycle in AD is needed. The spiral structure with alternating fixed width sections induces a high duty cycle GVD profile in longitudinal direction with a lightly chirped spatial frequency centered at 393 m^{-1} ($\Lambda = 2.54$ mm).

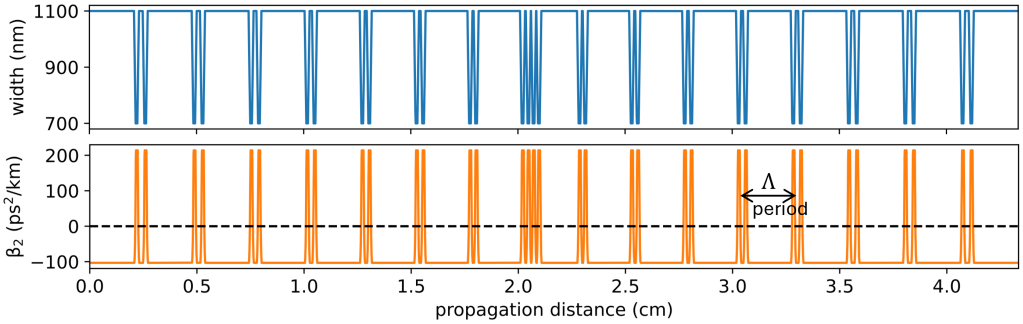

Fig. 6.6. Longitudinal evolutions of waveguide width and GVD. Pump wavelength 1380nm. The GVD period is centered to $\Lambda = 2.54$ mm.

6.3.2 . Spectral broadening measurements and simulations

The spectral broadening is characterized by a femtosecond laser setup of which the details can be found in Figure.5.3 in Chapter.5. TE-polarized 190 fs (T_{FWHM}) pump laser centered at the wavelength of 1380 nm is used for the generation of QPM-DWs and supercontinuum

(repetition rate f_{rep} 1 MHz). The input pump pulse laser is then coupled into the Si_3N_4 waveguide using an optical objective with coupling efficiency η of 10±0.2%. The spectral output is measured by spectrometers.
To maintain stable coupling efficiency between the input pulse and the waveguide, the following coupling strategies were implemented: Since both facets feature identical inverse tapers, it is assumed that the coupling efficiency is equal at both the input and output sides using the same optical objective. Initially, an optical objective with a numerical aperture (NA) of 0.35 was tested for both input and output coupling. The maximum experimentally measured coupling efficiency was -3.5 dB, while mode overlap simulations predicted a theoretical coupling efficiency of -0.8 dB. Subsequently, to eliminate chromatic aberration during spectral measurements, a reflective microscope objective (RMO, Thorlabs model: LMM40XF-P01, NA = 0.5) was used in place of the optical objective at the output side. The experimentally measured coupling efficiency of this reflective microscope objective with the inverse taper was also -3.5 dB. Finally, the optical objective on the input side was intentionally defocused. Although this adjustment enlarged the input beam spot and reduced the coupling efficiency, it significantly improved long-term stability against mechanical vibrations. The coupling efficiency at the input side was set to 10±0.2%. It is worth noting that the -3.5 dB coupling efficiency obtained with the RMO (NA = 0.5) on the output inverse taper is coincidentally the same as that achieved with the optical objective (NA = 0.35) on the input inverse taper. This is because the RMO, which suffers from central obscuration, requires a higher NA to achieve the same coupling efficiency.
The coupled on-chip pulse peak power P_0 is calculated by considering the average input power P_{ave}, coupling efficiency η, repetition rate f_{rep}, and the full-width half-maximum (FWHM) of the squared hyperbolic secant pulse T_{FWHM}:

$$P_0 = P_{ave} \cdot \eta \cdot \frac{1}{f_{rep}} \cdot \frac{1}{T_{FWHM}} \cdot 0.88 \tag{6.6}$$

Figure.6.7(a) shows the normalized power spectral density (PSD) for the experimental spectral broadening under an on-chip pump peak power of 110 W (black curve). The simulated result obtained using the Generalized Nonlinear Schrodinger Equation (GNLSE) for the same peak power is shown in red. A good agreement is observed between simulation and measurement with the observation of multiple peaks at wavelengths of about 1104 nm, 1180 nm, 1800 nm, 1930 nm, 2000 nm and 206 5nm. These peaks, induced by the QPM occurring along the waveguide, extend the spectrum from 1050nm to 2100nm, covering an octave broadening at -40 dB transmission range within the detection limit.
The analysis of each peak induced by the QPM condition requires to take into account the effective waveguide dispersion β_{eff} from its periodic width modulation. Different from Equation.6.2 in a perfect periodic waveguide, β_{eff} is defined as:

$$\beta_{eff} = \frac{1}{L} \sum_n \beta(n) \Delta L_n \tag{6.7}$$

because of its slightly chirped periodicity. In Equation.6.7, the waveguide is composed of n segments of different widths and ΔL_n is the length of each segment, including the taper. The total propagation length in the waveguide is hence $L = \sum_n \Delta L_n$. The β_{eff} is used in Equation.6.1 for phase mismatch calculation. The graphically determined wavelength positions of QPM-DWs are shown in Figure6.7(b) in green lines. The effective GVD parameter $\beta_{2,eff}$ is also deduced from β_{eff}, which defines the AD and ND regions for QPM waveguide. Apart

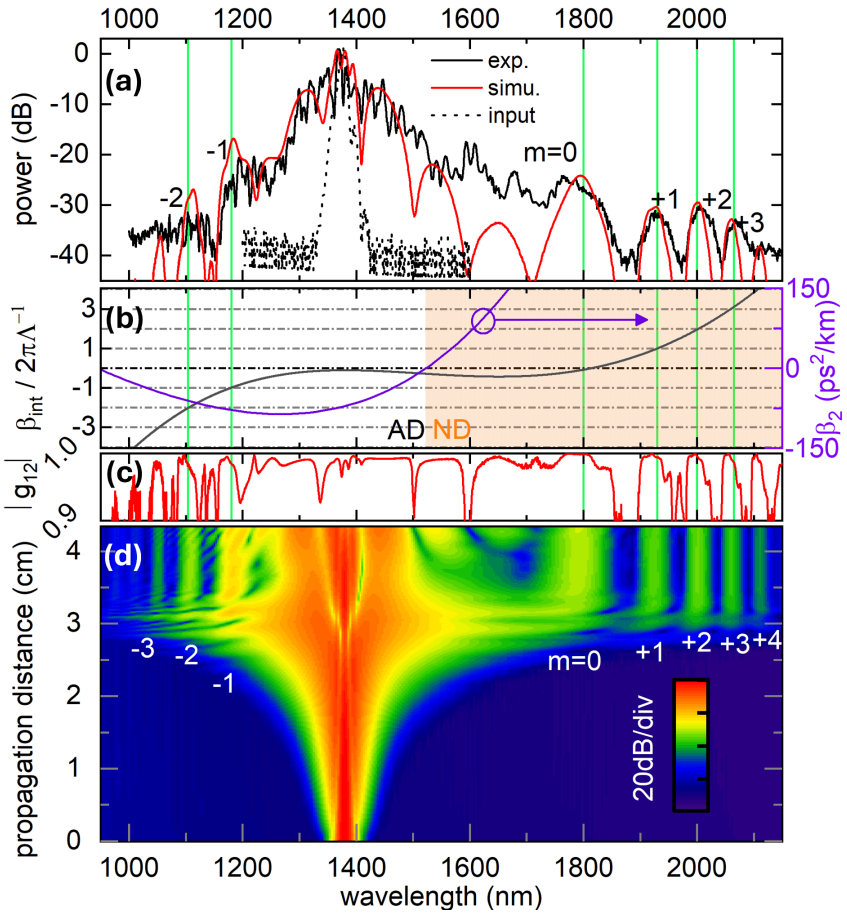

Fig. 6.7. Spectral broadening of the QPM waveguide at pump wavelength of 1380 nm and peak power of 110W. (a) Normalized power spectral density of experimental and simulated spectra from the QPM spiral waveguide. The input pump pulse spectrum is also included. (b) Left axis: phase mismatch parameter in black. Different orders of the QPM term are noted by horizontal gray dashed lines. Graphic solutions of QPM conditions are reported by vertical green lines. Right axis: GVD parameter is shown in purple, including the normal dispersion (ND, in yellow background) and anomalous dispersion (AD, in white background) regions. (c) Temporal coherence obtained by means of 30 simulated spectra of the QPM spiral waveguide. (d) Evolution of the spectrum along the propagation distance by solving GNLSE. QPM-DWs are denoted by order m.

from the 0 order, QPM-DWs orders from -2 to +3 are identified, existing in both ND and AD regions.

The QPM-DWs are easily identifiable, indicating a noteworthy energy transition through the QPM effect. Indeed, QPM effect strongly depends on GVD modulation depth $\Delta\beta_2$. In Figure.6.8, simulations illustrate spectral broadenings in waveguides that share similar β_{eff} as QPM waveguide but different $\Delta\beta_2$. It is shown that for weak $\Delta\beta_2 = 6\ \mathrm{ps}^2/\mathrm{km}$, which is already beyond most GVD dispersion depth realized in fiber[9], [18], no DW can be found except for the 0 order. As $\Delta\beta_2$ increases, the QPM-DWs grow, indicative of a stronger QPM effect. An empiric modulation depth for a significant QPM effect is $100\,\mathrm{ps}^2/\mathrm{km}$.

From simulations, we have also estimated the first-order degree of mutual coherence $|g_{12}|$ to characterize the temporal coherence given by Equation.3.25. Temporal coherence is shown in Figure.6.7(c). For clarity, only coherence$|g_{12}|$ above 0.9 is reported. An overall good temporal coherence property is demonstrated. More particularly, at wavelengths where QPM-DWs take

place, the coherence remains very high ($|g_{12}|$ very close to 1). The high coherence comes from the fact that QPM-DWs are generated directly from the soliton (soliton number $N = 5.07$, given $\gamma = 1.43\,\mathrm{W^{-1}m^{-1}}$), inheriting the good coherence.

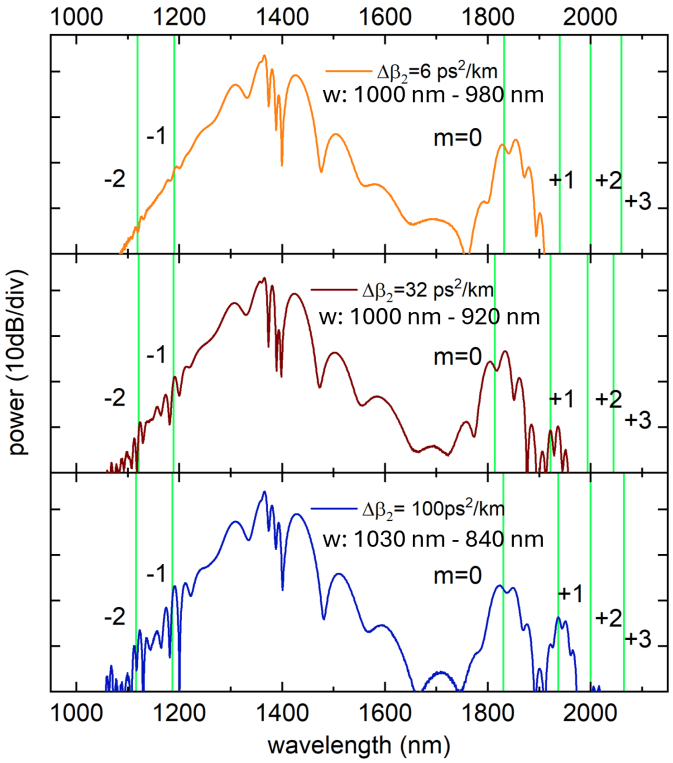

Fig. 6.8. Effect of GVD modulation depth $\Delta\beta_2$ over QPM-DWs generation. Their corresponding width variations are noted in insets. Modulation depths of GVD are $6\,\mathrm{ps^2/km}$, $32\,\mathrm{ps^2/km}$ and $100\,\mathrm{ps^2/km}$ from top to bottom, respectively.

6.3.3 . Nonlinear dynamics

The nonlinear dynamic of spectral broadening in the QPM waveguide is also analyzed by simulation, reporting the evolution of the spectral broadening as a function of the propagation distance (Figure.6.7(d)). The initial spectral broadening for a propagation distance L < 3 cm is due to soliton self-compression (SSC), which corresponds to a pulse compression in time domain. After approximately 3 cm of propagation, the soliton spectrum reaches its maximum, becoming spectrally overlapped with multiple solutions of QPM conditions. Furthermore, multiple QPM-DWs are simultaneously generated after the same propagation distance, which demonstrates a permanent conversion of energy from soliton to the spectral range defined by QPM conditions. While an infinite number of solutions can be derived from QPM conditions, only those orders that exhibit substantial spectral overlap with the soliton are generated with higher conversion efficiency. This criterion aligns with the typical prerequisite for DW generation in a longitudinally invariant waveguide[19], [20].

6.3.4 . Spectral broadening evolution with pump power

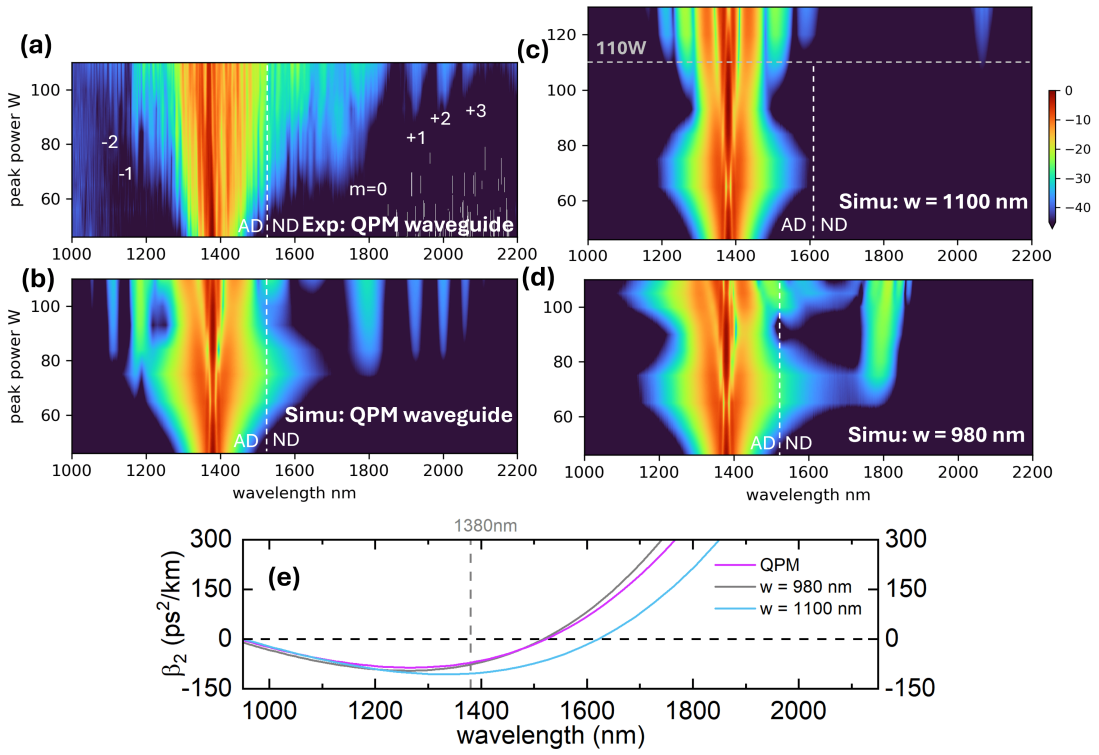

Fig. 6.9. Spectral evolution comparisons. The spectral evolution of SCG (powermap) as a function of the input peak power for experimental measurements (a) and simulations (b). QPM-DWs are denoted by their order m. The White dashed line shows the ZDW location. (c, d) Simulated powermap for waveguide width = 1100 nm, 980 nm, respectively. (e) GVD parameter β_2 for QPM, width = 980 nm, 1100 nm waveguides as a function of wavelength.

The QPM waveguide allows independent control of the DW phase matching condition, distinct from the waveguide dispersion through the QPM term $2\pi m\Lambda^{-1}$. As a result, the generation of DWs is significantly expanded to the spectral range reached by the soliton. In Figure.6.9(a, b), the spectrum evolution as a function of the pump power (powermap) is reported for both measurements and simulations, respectively. Starting from spectral broadening induced by SSC, DW_{-1} and DW_0 are initially generated at a pump peak power of 74 W after the soliton spectrum reaches the zero-dispersion wavelength (ZDW) at around 1523 nm. As the pump power increases, a growing number of higher-order QPM-DWs (m = -2, +1, +2, +3) emerge, consistently broadening the spectra. The power-dependent behavior can be briefly explained as follows: as the pump power increases, the final spectrum that the soliton can reach expands, giving rise to an increased number of QPM-DWs through spectral overlap.

6.3.5 . Spectral broadening efficiency

The efficiency of QPM waveguide is determined comparing its experimental spectral broadening with those obtained through simulations in longitudinal invariant reference waveguides under the same pumping conditions. Two reference waveguides are used, both having the same height, top cladding and propagation length as the QPM waveguide, except for the invariant widths, which are chosen to be 980 nm and 1100 nm. The comparison of the spectral broadening from QPM with these two reference waveguides is reported in Figure.6.10.
We first compare the QPM waveguide with the 980 nm wide waveguide. Although it is not pos-

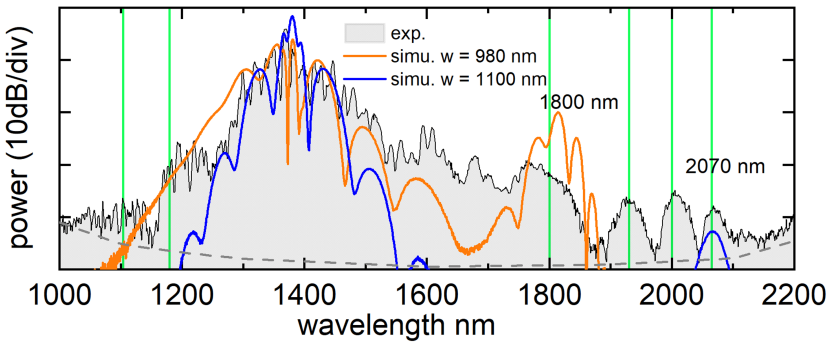

Fig. 6.10. The spectral broadening comparison. At a peak power of 110W, the QPM waveguide is compared with that of a longitudinally invariant waveguide width w = 980 nm (orange) and 1100 nm (blue). The dashed curve is the noise floor.

sible to find a real waveguide geometry that shares the same GVD curve as the effective GVD, a similar GVD curve can still be found (i.e. GVD of w = 980 nm, Figure.6.9(e)). Its DW can then be generated at the same wavelength as DW0 of the QPM waveguide (at a wavelength of 1800 nm). As it can be seen in Figure.6.10, the QPM waveguide exhibits a significantly broader spectral extension across both shorter and longer wavelength ranges compared to the spectrum obtained with w = 980 nm. As both waveguides share similar GVD, the spectral broadenings during SSC are also similar (Figure.6.9(b,d)). However, due to the introduction of QPM behavior in the waveguide, QPM-DWs are generated in the full soliton spectrum. Indeed, the soliton energy extending beyond DW_0 is effectively harnessed by higher-order DWs, surpassing the behavior observed in the w = 980 nm waveguide.
A second reference waveguide, w = 1100 nm (depicted in blue in Figure.6.10), has also been considered. This waveguide possesses its QPM conditions for the DW at a wavelength of 2065 nm, corresponding to DW_{+3} of the QPM waveguide. QPM waveguide demonstrates a 5 dB stronger conversion efficiency at this wavelength, even though the conversion is through higher-order QPM-DW. From the powermap reported in Figure.6.9(c), most of the spectrum of 1100 nm width waveguide is localized between 1200 nm and 1600 nm in AD region in the form of higher-order soliton[21]. Although its geometry allows its DW phase matching condition at 2065 nm, the efficient energy conversion from soliton to DW is weak because it is pumped at a wavelength where the HOD is faint (the slope of GVD curve is almost zero, see Figure.6.9(e)). In comparison, the QPM waveguide offers smaller GVD and stronger HOD, which have a benefit for both SSC and soliton fission at the pump wavelength, inducing stronger frequency conversion even for DW+3 at a wavelength of 2065 nm.

6.4 . Characterization in two ZDW system

For a more general case in an integrated platform where broadening of the pump can reach both ZDW, QPM-DWs still exist. A shorter QPM waveguide with a reduced period is presented to illustrate QPM-SCG in a two-ZDW system.
This two ZDW QPM waveguide has a length of 2.1 cm with spatial frequency centred at 817 m^{-1} ($\Lambda = 1.22\,\mathrm{mm}$), of which its width variation over propagation can be found in Figure.6.11(e). Experimental measurement and simulation under a pump at a wavelength of 1380 nm of 290 W peak power reveal that the spectrum covers both DW_0 in short and long wavelength sides. The QPM-DWs at long wavelength side show good agreement with locations prediction from QPM

conditions (Figure.6.11(b)). Although from GNLSE simulation in Figure.6.11(d), QPM-DWs can still be generated beyond 2.2 μm, they cannot be found in experimental measurements because mode becomes extremely leaky when going through the rapid bend (width = 700 nm, bend radius 30 μm).

In order to reach the DW_0 at short wavelength region, the pump peak power rises to 290 W which gives soliton number $N = 11$. Although the condition $L_{NL} > \Lambda$ is respected, this condition for accurate QPM-DWs prediction using effective dispersion is no longer true before soliton fission since soliton peak power largely increased after SSC in this soliton number. It may explain why at short wavelength region (from 550 nm to 1050 nm), while multi-peaks structure can still be found, individual QPM-DWs peak can no longer be clearly identified.

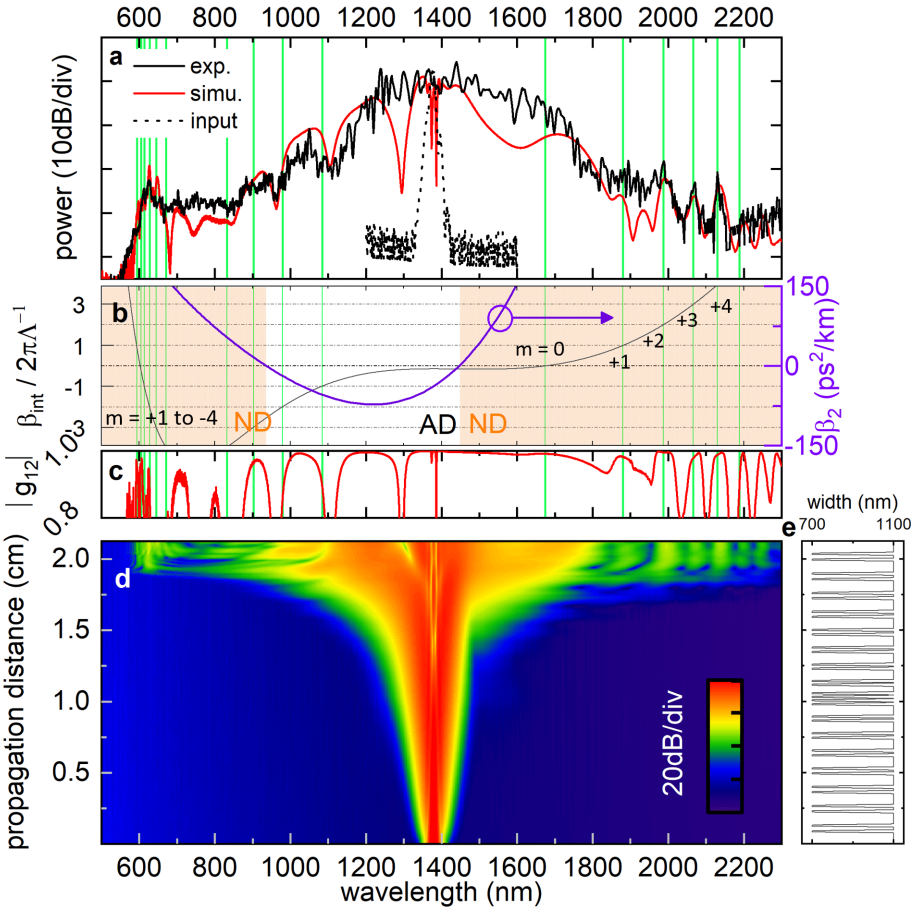

Fig. 6.11. Spectral broadening of a two ZDW QPM waveguide at a wavelength of 1380nm and for a pump peak power of 290W. (a) power spectral density (PSD) of experimental and simulated spectra. (b) Left axis: phase mismatch in black. Different orders of QPM term are noted by horizontal gray dashed lines. Graphic solutions of QPM condition are noted by vertical green lines. Right axis: GVD parameter is shown in purple. (c) Temporal coherence obtained by means of 30 simulated spectra. (d) Evolution of the spectrum along the propagation distance by solving GNLSE. (e) Waveguide width variation along the propagation.

6.5 . QPM SCG pumped in normal dispersion region

Although DW generation is typically associated with soliton dynamics, requiring the pump to be at a wavelength within the anomalous dispersion regime, DWs can also be produced when the pump is in the normal dispersion regime. In such cases, the shock front replaces the soliton[9], [22].

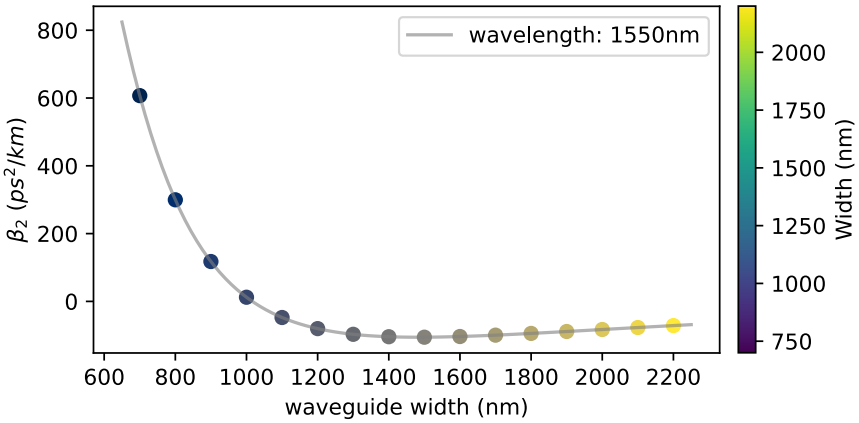

Fig. 6.12. GVD in the function of waveguide width at wavelength 1550 nm. The Si_3N_4 waveguide height is 800 nm buried in 3 μm SiO_2 layer.

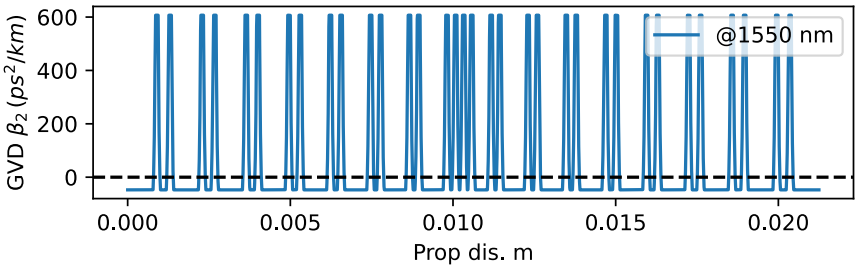

Fig. 6.13. GVD modulation of the QPM waveguide pumped at 1550 nm. The waveguide geometry is the same as in the Section.6.4 shown in Figure.6.11(e).

We pump the same waveguide reported in the Section.6.4, the width as a function of propagation distance of which is presented in Figure.6.11(e). The pump wavelength is at 1550 nm in TE mode. The GVD as a function of waveguide width at 1550 nm wavelength is shown in Figure.6.12. The modulation of GVD is thus calculated which varies from slight anomalous to normal area (Figure.6.13) with strong GVD modulation depth of over 600 $\mathrm{ps}^2/\mathrm{km}$. Although the pulse propagates mostly in anomalous dispersion, the strong normal dispersion segments still make the effective GVD slightly normal as $\beta_2 = 93\,\mathrm{ps}^2/\mathrm{km}$ with $\beta_3 = -1.41\,\mathrm{ps}^3/\mathrm{km}$. From the simulation given the pump peak power of 1802 W (190 fs), the pulse temporal evolution in this QPM waveguide is presented in Figure.6.14. The pulse temporal profile is not compressed, which is clear evidence that the pulse undergoes a normal, effective GVD. Through the propagation, a flat top background and the shock wave front appear due to the β_2 and β_3. This shock wave front (working similarly to the soliton self-compression (SSC) in anomalous GVD regions) produces different frequency components that convert to DWs after the pulse breaking. The temporal profile before DW generation is also shown in Figure.6.14.
To calculate the PM condition for DW generation in normal GVD region, some modifications

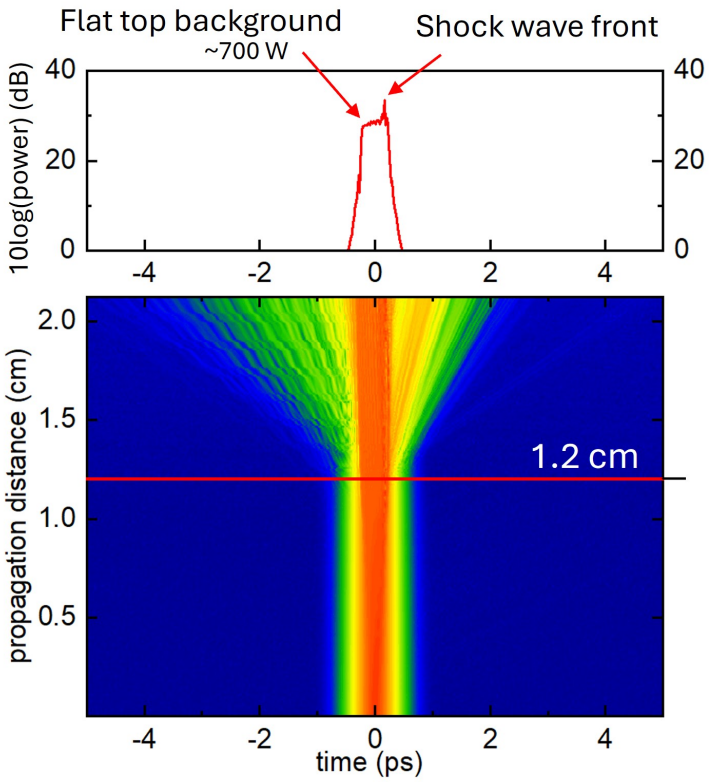

Fig. 6.14. Pulse temporal evolution when the pump is at 1550 nm in normal GVD region. The pump peak power is 1802 W. The pulse width variation as a function of propagation distance. The pulse temporal profile before the DW generation at the red line position is shown in the top figure.

have to be made from Equation.6.1[9]

$$\beta_{eff}(\omega) - \beta_{eff}(\omega_s) - v_{g,eff}^{-1}(\omega - \omega_s) - k_{nl} = \frac{2\pi}{\Lambda}m \tag{6.8}$$

where $k_{nl} = -\gamma P_b$, being P_b the power of the background field over which the DW propagates[23], [24]. Here $P_b = 700\,\mathrm{W}$ shown in Figure.6.14.
Experimental measurements were carried out by pumping with three different powers at 1550 nm using the 190-fs laser pulse. The average incident powers were measured, and the peak powers coupled to the waveguide were estimated, taking into account the coupler loss. Both measurement and simulation spectral broadening results are shown in Figure.6.15.

Since the effective GVD is normal ($\beta_{2,eff} > 0$), the shock front here takes the place of soliton in anomalous GVD ($\beta_{2,eff} < 0$). At low pump power, only the spectrum broadening from self-phase modulation (SPM) and third harmonic generation (THG) is observed. When increasing peak power, QPM-DW peaks begin to appear (Figure.6.15(b)). The QPM-DWs longer than $2\,\mu\mathrm{m}$ appears even before DW_0 in visible range. At peak power of 1802 W, the multi QPM-DWs of order from 0 up to +5 can be found shown in Figure.6.15 (c). The phase matching condition based on Equation.6.8 is presented and DWs are well determined by QPM terms. Here, we also show the simulations of effective GVD. By comparing results with and without GVD modulation, it is clear to see that the spectrum is broadened by QPM-DWs.
Clear THG appears from measurements but is not simulated because it is not included in the GNLSE model. In an integrated platform, the THG is usually realized by phase-matching of the

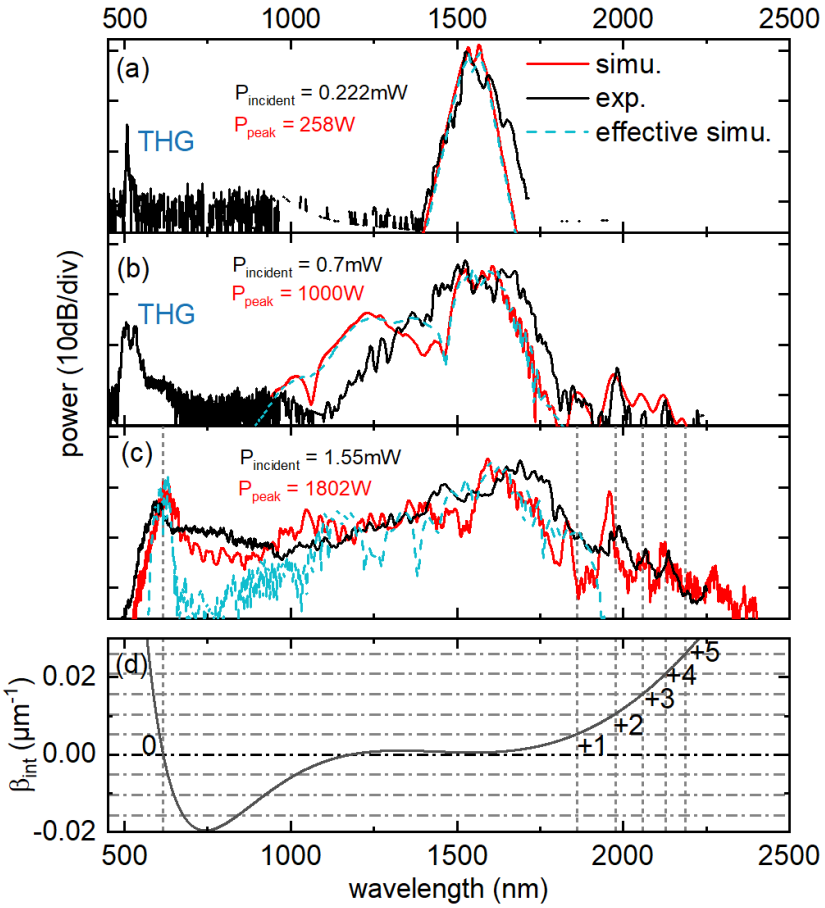

Fig. 6.15. Experiment and simulation results under a pump at a wavelength of 1550nm. Measurements and simulations based on the QPM waveguide are shown in black and red, respectively. Simulations based on effective GVD are shown in light blue. (a) shows SPM and THG in low pump peak power. (b) shows that the rising of QPM-DWs around 2 μm. Please note that the THG signal and IR signal should not be compared in intensity since they are detected by two sensors with different noise floors. (c) shows different orders of QPM-DWs and compares with the prediction from a graphic solution of phase matching condition.

fundamental mode pump with higher-order modes third harmonic[25]. Figure.6.16 shows the effective index of the fundamental TE mode around pump wavelength (in back) and four higher order TE modes in the third harmonic range (in colored lines). These simulated effective indices are based on Si_3N_4 waveguide geometry 1100×800 nm because most of the QPM waveguide has a width of 1100 nm. Two crossings of TE_0 mode with the 20^{th} and 21^{th} modes shown in blue and red line are found, indicating the effective index matching cover the THG range around 500 nm wavelength. Two other modes, mode 17^{th} and 24^{th}, are also plotted in blue and red dashed lines. Although they are not perfectly phase-matched with TE_0, the effective indices are close. Possible THG may also happen to these modes if the periodicity of the QPM waveguide is considered, knowing as quasi-phase-matched THG[26].

We can expect that by an adequate design, a waveguide with high duty cycle of normal GVD over anomalous GVD while still keeping effective GVD below zero is feasible. This is interesting in terms of coherence for SC generation pumped in anomalous GVD because the length for

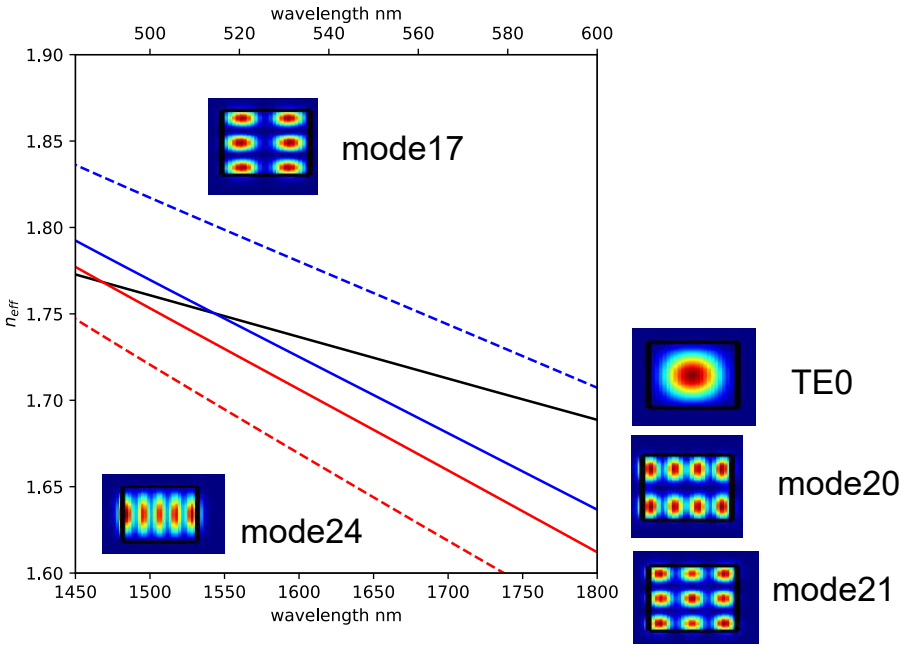

Fig. 6.16. Simulated effective refractive indices of the TE modes for the fundamental and third harmonic in a buried Si_3N_4 waveguide with a cross-section of 1100 $\times$ 800 nm. The black curve corresponds to the effective index of the TE_0 mode around the pump wavelength. The blue and red curves correspond to two modes phase-matched for THG. The two dashed lines are two modes close to phase match. The mode distributions and mode orders are showed in insets.

modulation instability to build up is then very limited.

6.6 . Conclusions and perspectives

In this chapter, we explored supercontinuum generation (SCG) with the generation of multiple dispersive waves (DWs) through quasi-phase matching (QPM). The main focus was on controlling significant dispersion variations within the integrated waveguide. We discussed both single and dual zero-dispersion wavelength (ZDW) systems when the pump was located in the anomalous group velocity dispersion (GVD) region. Additionally, we examined QPM-SCG when the pump was in the normal GVD region. The QPM process shows its robustness in different cases and can open a new way for DW control on the integrated platform.
By comparing the spectral broadening between the QPM waveguide and the width-invariant waveguide, we find that the QPM waveguide enables more efficient spectral broadening under the same pump conditions. This is because the QPM conditions extend the dispersive wave (DW) generation across the entire spectral range accessible to the soliton.
For compactness, the spiral is designed with a rectangular shape, leading to a subtle variation in the period Λ. However, this variation is minor and does not impact the favorable characteristics of the QPM terms and the well-defined spectral locations of QPM-DWs. Furthermore, our non-sinusoidal GVD modulation shape suggests that the QPM method can be applied to a broader range of periodic structures. In particular, the absence of fabrication barriers in integrated photonic platform allows for versatile width variations, enabling the design of multiple longitudinal spatial frequencies. This, in turn, offers the potential for user-defined spectral

shapes of higher-order QPM-DWs in the future.
The DW generation discussed in this chapter generally exhibits moderate energy conversion efficiency. The primary reason for this is that the pump pulse duration of 190 fs is not sufficiently short. A pump in the tens-of-femtoseconds range could significantly enhance the conversion efficiency. In the future, we expect an on-chip pulse compression plays a crucial role as a preparatory step before SCG.

References

[1] A. Arrigo, M. Teussink, E. Aragona, F. Bandello, and M. Battaglia Parodi, "MultiColor imaging to detect different subtypes of retinal microaneurysms in diabetic retinopathy", en, *Eye*, vol. 35, no. 1, pp. 277–281, 2021, ISSN: 0950-222X, 1476-5454. DOI: 10.1038/s41433-020-0811-6.

[2] M. D. Lesoine, S. Bose, J. W. Petrich, and E. A. Smith, "Supercontinuum Stimulated Emission Depletion Fluorescence Lifetime Imaging", en, *The Journal of Physical Chemistry B*, vol. 116, no. 27, pp. 7821–7826, 2012, ISSN: 1520-6106, 1520-5207. DOI: 10.1021/jp303912p.

[3] M. Montesinos-Ballester, C. Lafforgue, J. Frigerio, *et al.*, "On-Chip Mid-Infrared Supercontinuum Generation from 3 to 13 m Wavelength", en, *ACS Photonics*, vol. 7, no. 12, pp. 3423–3429, 2020, ISSN: 2330-4022, 2330-4022. DOI: 10.1021/acsphotonics.0c01232.

[4] Z. Zhao, B. Wu, X. Wang, *et al.*, "Mid-infrared supercontinuum covering 2.0–16 m in a low-loss telluride single-mode fiber", en, *Laser & Photonics Reviews*, vol. 11, no. 2, p. 1 700 005, 2017, ISSN: 1863-8880, 1863-8899. DOI: 10.1002/lpor.201700005.

[5] C. Brahms, F. Belli, and J. C. Travers, "Resonant dispersive wave emission in hollow capillary fibers filled with pressure gradients", en, *Optics Letters*, vol. 45, no. 16, p. 4456, 2020, ISSN: 0146-9592, 1539-4794. DOI: 10.1364/OL.398343.

[6] R. Scheibinger, J. Hofmann, K. Schaarschmidt, M. Chemnitz, and M. A. Schmidt, "Temperature-Sensitive Dual Dispersive Wave Generation of Higher-Order Modes in Liquid-Core Fibers", en, *Laser & Photonics Reviews*, vol. 17, no. 1, p. 2 100 598, 2023, ISSN: 1863-8880, 1863-8899. DOI: 10.1002/lpor.202100598.

[7] F. Köttig, D. Novoa, F. Tani, *et al.*, "Mid-infrared dispersive wave generation in gas-filled photonic crystal fibre by transient ionization-driven changes in dispersion", en, *Nature Communications*, vol. 8, no. 1, p. 813, 2017, ISSN: 2041-1723. DOI: 10.1038/s41467-017-00943-4.

[8] R. Scheibinger, N. M. Lüpken, M. Chemnitz, *et al.*, "Higher-order mode supercontinuum generation in dispersion-engineered liquid-core fibers", en, *Scientific Reports*, vol. 11, no. 1, p. 5270, 2021, ISSN: 2045-2322. DOI: 10.1038/s41598-021-84397-1.

[9] M. Conforti, S. Trillo, A. Mussot, and A. Kudlinski, "Parametric excitation of multiple resonant radiations from localized wavepackets", en, *Scientific Reports*, vol. 5, no. 1, p. 9433, 2015, ISSN: 2045-2322. DOI: 10.1038/srep09433.

[10] J. Lin, N. Yao, Z. Hao, *et al.*, "Broadband Quasi-Phase-Matched Harmonic Generation in an On-Chip Monocrystalline Lithium Niobate Microdisk Resonator", en, *Physical Review Letters*, vol. 122, no. 17, p. 173 903, 2019, ISSN: 0031-9007, 1079-7114. DOI: 10.1103/PhysRevLett.122.173903.

[11] D. D. Hickstein, G. C. Kerber, D. R. Carlson, *et al.*, "Quasi-Phase-Matched Supercontinuum Generation in Photonic Waveguides", en, *Physical Review Letters*, vol. 120, no. 5, p. 053 903, 2018, ISSN: 0031-9007, 1079-7114. DOI: 10.1103/PhysRevLett.120.053903.

[12] D. T. H. Tan and B. J. Eggleton, "Bragg Solitons – Historical and Future Perspectives", en, *Laser & Photonics Reviews*, p. 2 300 373, 2023, ISSN: 1863-8880, 1863-8899. DOI: 10.1002/lpor.202300373.

[13] D. Sun, Y. Zhang, D. Wang, *et al.*, "Microstructure and domain engineering of lithium niobate crystal films for integrated photonic applications", en, *Light: Science & Applications*, vol. 9, no. 1, p. 197, 2020, ISSN: 2047-7538. DOI: 10.1038/s41377-020-00434-0.

[14] H. El Dirani, L. Youssef, C. Petit-Etienne, *et al.*, "Ultralow-loss tightly confining Si $_3$ N $_4$ waveguides and high-Q microresonators", en, *Optics Express*, vol. 27, no. 21, p. 30 726, 2019, ISSN: 1094-4087. DOI: 10.1364/OE.27.030726.

[15] Q. Wilmart, S. Guerber, J. Faugier-Tovar, *et al.*, "A device library for the ultra-low loss Si3N4 platform", in *Silicon Photonics XVII*, G. T. Reed and A. P. Knights, Eds., San Francisco, United States: SPIE, 2022, p. 33, ISBN: 978-1-5106-4883-8 978-1-5106-4884-5. DOI: 10.1117/12.2606853.

[16] K. Ikeda, R. E. Saperstein, N. Alic, and Y. Fainman, "Thermal and Kerr nonlinear properties of plasma-deposited silicon nitride/ silicon dioxide waveguides", en, *Optics Express*, vol. 16, no. 17, p. 12 987, 2008, ISSN: 1094-4087. DOI: 10.1364/OE.16.012987.

[17] B. J. Soller, D. K. Gifford, M. S. Wolfe, and M. E. Froggatt, "High resolution optical frequency domain reflectometry for characterization of components and assemblies", en, *Optics Express*, vol. 13, no. 2, p. 666, 2005, ISSN: 1094-4087. DOI: 10.1364/OPEX.13.000666.

[18] A. Mussot, M. Conforti, S. Trillo, F. Copie, and A. Kudlinski, "Modulation instability in dispersion oscillating fibers", en, *Advances in Optics and Photonics*, vol. 10, no. 1, p. 1, 2018, ISSN: 1943-8206. DOI: 10.1364/AOP.10.000001.

[19] S. Roy, S. K. Bhadra, and G. P. Agrawal, "Effects of higher-order dispersion on resonant dispersive waves emitted by solitons", en, *Optics Letters*, vol. 34, no. 13, p. 2072, 2009, ISSN: 0146-9592, 1539-4794. DOI: 10.1364/OL.34.002072.

[20] N. Akhmediev and M. Karlsson, "Cherenkov radiation emitted by solitons in optical fibers", en, *Physical Review A*, vol. 51, no. 3, pp. 2602–2607, 1995, ISSN: 1050-2947, 1094-1622. DOI: 10.1103/PhysRevA.51.2602.

[21] *Nonlinear Fiber Optics*, en. Elsevier, 2013, ISBN: 978-0-12-397023-7. DOI: 10.1016/C2011-0-00045-5.

[22] Y. Okawachi, M. Yu, J. Cardenas, X. Ji, M. Lipson, and A. L. Gaeta, "Coherent, directional supercontinuum generation", en, *Optics Letters*, vol. 42, no. 21, p. 4466, 2017, ISSN: 0146-9592, 1539-4794. DOI: 10.1364/OL.42.004466.

[23] M. Conforti, F. Baronio, and S. Trillo, "Resonant radiation shed by dispersive shock waves", en, *Physical Review A*, vol. 89, no. 1, p. 013 807, 2014, ISSN: 1050-2947, 1094-1622. DOI: 10.1103/PhysRevA.89.013807.

[24] M. Conforti and S. Trillo, "Dispersive wave emission from wave breaking", en, *Optics Letters*, vol. 38, no. 19, p. 3815, 2013, ISSN: 0146-9592, 1539-4794. DOI: 10.1364/OL.38.003815.

[25] Y. Okawachi, M. Yu, J. Cardenas, *et al.*, "Carrier envelope offset detection via simultaneous supercontinuum and second-harmonic generation in a silicon nitride waveguide", en, *Optics Letters*, vol. 43, no. 19, p. 4627, 2018, ISSN: 0146-9592, 1539-4794. DOI: 10.1364/OL.43.004627.

[26] K. Tarnowski, B. Kibler, C. Finot, and W. Urbanczyk, "Quasi-Phase-Matched Third Harmonic Generation in Optical Fibers Using Refractive-Index Gratings", en, *IEEE Journal of Quantum Electronics*, vol. 47, no. 5, pp. 622–629, 2011, ISSN: 0018-9197, 1558-1713. DOI: 10.1109/JQE.2011.2107888.

7 - Towards an on-chip pulse compression

Summary

An ideal on-chip supercontinuum generation (SCG) system can be realized by integrating an on-chip laser source directly with the waveguide that triggers SCG. For efficient and coherent SCG, which aims to achieve both broad spectral coverage and high temporal coherence, the pump laser pulse duration should ideally be shorter than 200 fs. In practice, to efficiently generate dispersive waves (DWs) with a high conversion efficiency of around 10% into the targeted wavelength range, a pump pulse duration on the order of tens of femtoseconds is highly preferred. Current state-of-the-art on-chip laser sources typically achieve pulse durations in the picosecond or sub-picosecond range (see Chapter.2 for more details). Thus, pulse compression is a crucial building block for achieving on-chip SCG. A common method to achieve on-chip pulse compression is through soliton self-compression (SSC), as discussed in Chapter 5 and Chapter 6. SSC is also the primary mechanism responsible for spectral broadening in the initial stages of SCG. However, because SSC occurs as part of the evolution of higher-order solitons, the pulse shape after compression is not ideal for use as a pump source for SCG.

Alternatively, pulse compression to achieve a good pulse shape with a low pedestal, suitable for SCG, can be realized through a two-stage method. The schematic illustration is shown in Figure.7.1. Firstly, self-phase modulation (SPM) is employed to introduce a frequency chirp, the time-dependent instantaneous frequency shift to the carrier frequency, to the newly generated frequency components (see Section.3.1 for details). Secondly, an anomalous group velocity dispersion (GVD) grating can be utilized to temporally shift the SPM-generated frequencies towards the center of the pulse (see Section.3.2 for details), thereby facilitating temporal compression.

However, there are three main challenges towards on-chip pulse compression. Firstly, the on-chip laser source is not powerful enough in term of peak power to benefit from SPM. Second, the chirp generated by SPM close to zero GVD has a S shape, which is not ideal for dispersive grating to compensate who introduces linear frequency down chirp. Thirdly, up to now, the on-chirp dispersive grating is still quite narrow band, not supporting a pulse duration shorter

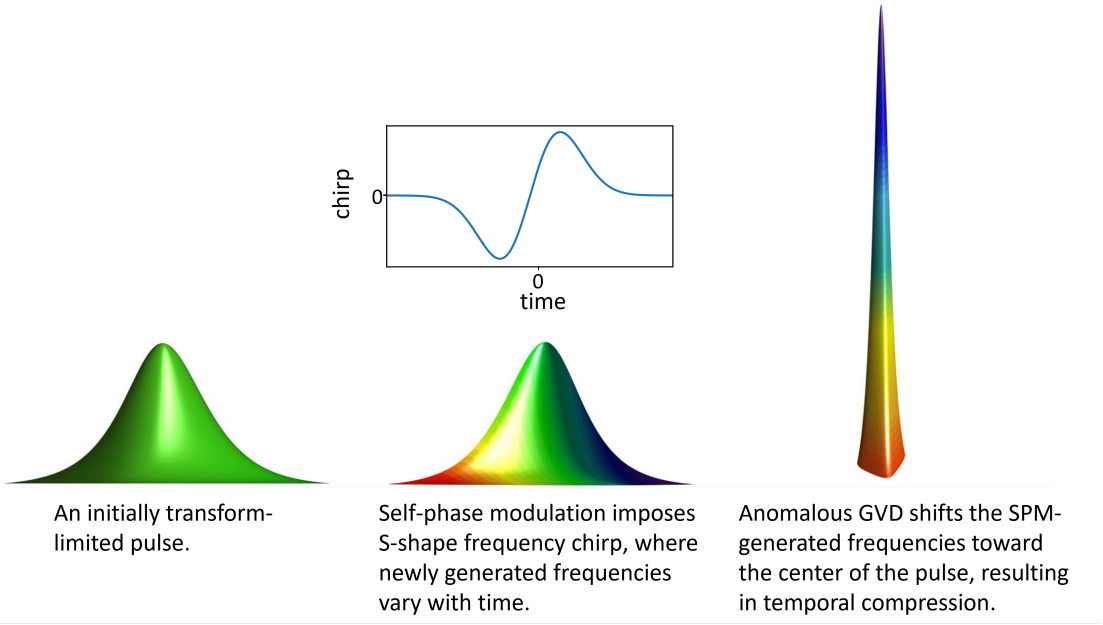

Fig. 7.1. Principle of the two-stage pulse compression. The first stage involves the generation of new frequencies. These new frequencies have a temporal distribution within the pulse, leading to a chirped pulse. The second stage requires adequate anomalous GVD so that the newly generated frequencies are realigned, resulting in pulse compression. The figure is modified from [1].

than 500 fs.

In this context, the work presented in this manuscript aims to adapt the self-similar compression scheme, which has been extensively studied in fiber optics [2], to the integrated Si_3N_4 platform. An illustration is provided in Figure.7.2. The scheme consists of two stages. In the first stage, the initial pulse propagates in a gain medium with normal dispersion, resulting in an amplified parabolic-shaped pulse. In the second stage, a broadband pulse compressor is used to compress the pulse. This chapter is organized as follows: A theoretical investigation, including simulations, is conducted to explore the implementation of amplification within a waveguide exhibiting normal GVD. The objective is to leverage self-similar propagation phenomena to generate linearly chirped pulses with sufficient power. Then, a novel configuration of a dispersive grating is proposed to achieve the bandwidth necessary for compressing pulse duration to below 200 fs. This design holds promise for applications in coherent supercontinuum generation using picosecond pulse pump lasers.

7.1 . Self-similar propagation in Si_3N_4 waveguide

Pulses propagate in a waveguide that exhibits normal GVD and undergo a phenomenon called optical wave breaking (OWB), which linearised frequency chirp. Moreover, when distributed gain is introduced during propagation, the form of the input pulse gradually converges asymptotically to a parabolic pulse exhibiting self-similar characteristics, irrespective of the initial pulse shape[2]. The pulse in self-similar propagation exhibits fascinating characteristics with respect to frequency chirp: a linear chirp that only depends on dispersion and gain[3]. The asymptotic solution of the electric field Ψ can be expressed by amplitude A and phase Φ

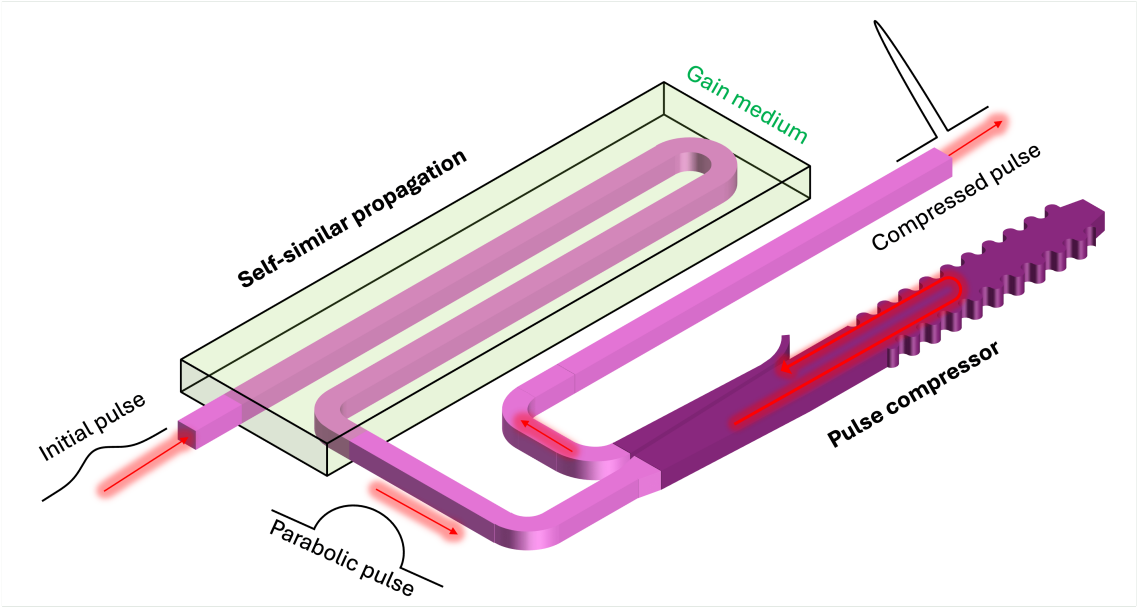

Fig. 7.2. Illustration of an on-chip self-similar pulse compression. The initial pulse propagates first in a waveguide with gain, undergoing a self-similar propagation. Then, a pulse compressor realigns the chirp to compress the pulse.

evolution with propagation z and time T[2], respectively as:

$$\Psi(z,T) = A(z,T)\exp\left(i\Phi(z,T)\right) \tag{7.1}$$

$$A(z,T) = A_0\exp\left(\frac{g}{3}z\right)\sqrt{1-\frac{T^2}{T_p^2(z)}} \tag{7.2}$$

$$\Phi(z,T) = \phi_0 + \frac{3\gamma A_0^2}{2g}\exp\left(\frac{2}{3}gz\right) - \frac{g}{6\beta_2}T^2 \tag{7.3}$$

where γ is the nonlinear coefficient, g is the gain in m^{-1}, β_2 the GVD parameter, ϕ_0 is an arbitrary constant, and T_p and A_0 characterize the parabolic pulse width and amplitude, respectively:

$$A_0 = \frac{1}{2}\left(\frac{gU_{in}}{\sqrt{\gamma\beta_2/2}}\right)^{1/3} \tag{7.4}$$

$$T_p(z) = \frac{6\sqrt{\gamma\beta_2/2}}{g}A_0\exp\left(\frac{g}{3}z\right) \tag{7.5}$$

where U_{in} is the input pulse energy According to Equation.7.6, rewritten here:

$$\Omega(z,T) = -\frac{d\Phi(z,T)}{dT} \tag{7.6}$$

the instant frequency chirp in Hz is:

$$\Delta f = \frac{\Omega(T)}{2\pi} = \frac{1}{2\pi}\frac{g}{3\beta_2}\cdot T \tag{7.7}$$

Simulations of the pulse propagation is carried out using GNLSE that only taking SPM and

GVD in the first place. A benchmark is first made to the parameter used in reference paper [3] with an input parabolic pulse of 190 fs and peak power of 53 W. The simulation result is shown in Figure.7.3. A clear parabolic pulse shape can be found at the end of the propagation with linear chirp over the pulse perfectly agreed by analytic calculation. Although self-similar

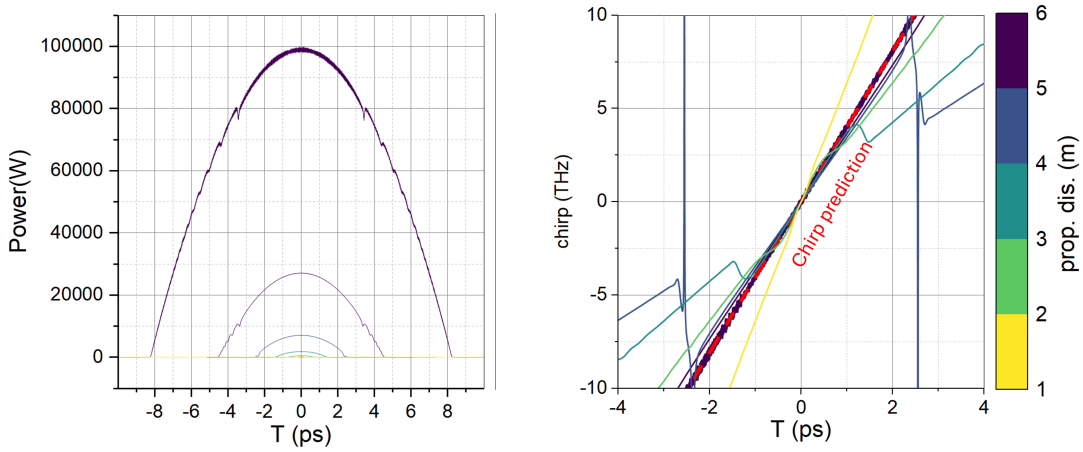

Fig. 7.3. Evolution of a hyperbolic secant 190-fs pulse toward a parabolic pulse in a 6-m normal-GVD fiber amplifier. Parameters from reference paper[3]: $g = 1.9\,\mathrm{m}^{-1}$, $\beta_2 = 25\,\mathrm{ps}^2\mathrm{m}^{-1}$, $\gamma = 5.8 \cdot 10^{-3}\,\mathrm{W}^{-1}\mathrm{m}^{-1}$ (a) Temporal pulse evolution. (b) Chirp evolution and chirp predicted by Equation.7.7 in red dash line.

propagation in normal-GVD fiber has been studied for pulse compression by using free-space grating sets[2], [4], it has not been applied to an integrated platform. Hence, initial parameters must be selected within a practical range achievable on the silicon nitride platform. Later, HOD like β_3 will be taken into account because β_3 in integrated platform is usually much higher than fiber. Finally, the initial input pulse condition like pulse shape and pulse duration will be also investigated.

7.1.1 . Principle parameters

Considering a 700 nm height strip Si_3N_4 waveguide, a gain of $g = 46\,\mathrm{m}^{-1}$ (equivalent to 2 dB/cm) is a feasible value for an integrated platform. This gain can be achieved through heterogeneous integration with erbium-doped or thulium-doped oxide materials [5]–[7]. The waveguide width is set to approximately 700 nm, allowing it to exhibit normal GVD with $\beta_2 = 700\,\mathrm{ps}^2/\mathrm{km}$ at a wavelength of 1550 nm and a nonlinear coefficient of $\gamma = 1\,\mathrm{W}^{-1}\mathrm{m}^{-1}$. No higher-order dispersion (HOD) terms are considered, i.e., $\beta_n = 0$ for $n > 2$. A hyperbolic secant pulse with a 1 ps (FWHM) duration and a peak power of 100 W (corresponding to a pulse energy of 113 pJ) is injected into the waveguide. The wavelength is centered at 1550 nm, which lies within the amplification range of Er-doped materials. Based on these parameters, the amplitude $A(z, T = 0)$ and pulse width $T_p(z)$ during the asymptotic parabolic pulse evolution are calculated according to Equation 7.4 and Equation 7.5, as shown in Figure.7.4.
The propagation distance that allows the pulse to approach the asymptotic solution is characterized by Z_c[3], which is written as:

$$Z_c(N) = \frac{3}{2g} \ln\left(\frac{N \cdot g}{6|\gamma|A_0^2}\right) \tag{7.8}$$

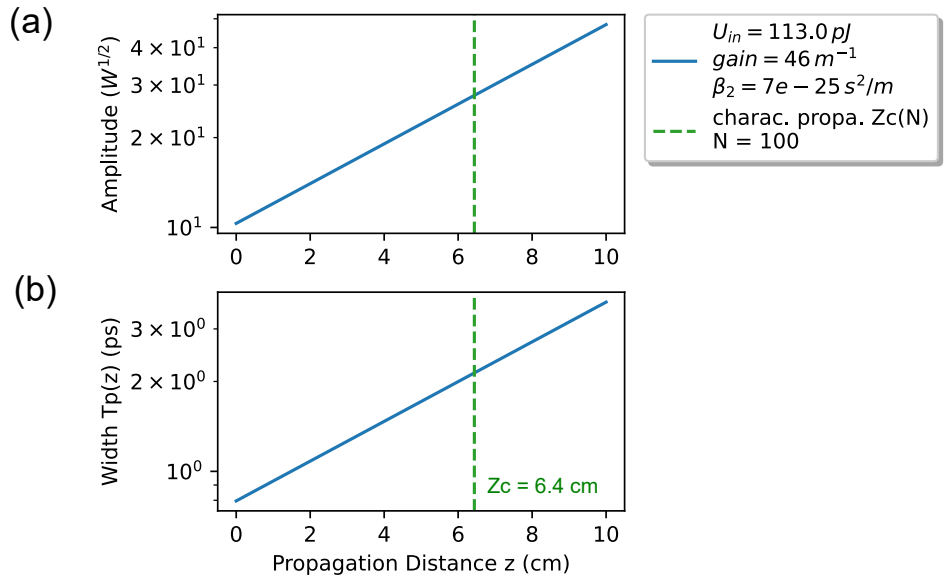

Fig. 7.4. The theoretical prediction for the asymptotic parabolic pulse evolution. The amplitude and temporal width are shown in (a) and (b). The characteristic propagation distance Z_c of 6.4 cm is marked in the green line.

N is some large value usually taken as 100. $Z_c(N = 100) = 6.4\,\mathrm{cm}$ marked in green line in Figure.7.4. The total propagation distance is then set to be close to Z_c as 5 cm such that an overall 10 dB gain is realized on-chip, considering a gain of 2 dB/cm.

The simulation results by NLSE are shown in Figure.7.5. In Figure.7.5(a), it can be seen that the spectrum of the input pulse broadens through propagation by SPM. In a -20 dB range, the spectral bandwidth braodens from less than 10 nm to around 60 nm. The temporal profile also shows a pulse broadening in Figure.7.5(c) (black curve) related to the propagation in normal GVD.

Upon computing the frequency chirp of the pulse following a 5 cm propagation and comparing it with the chirp computed using Equation 7.7, we observe a close agreement between the pulse chirp and the linear chirp prediction, especially in the center. This alignment suggests that the pulse has entered the asymptotic regime although it is not as good as the result in fiber shown in Figure.7.3(b). By further propagation in this waveguide amplifier, the pulse will eventually run into a perfect self-similar regime. However, a longer propagation distance entails a greater net gain. While an on-chip net gain of 18 dB has been demonstrated[5], achieving a net gain exceeding 10 dB is typically a challenging task due to the doping concentration limit.

The biggest difference of the chirp compared to the prediction occurs outside the 1.5 ps pulse duration range, where the power decreases rapidly with time (see in the inset of Figure.7.5(c)). The temporal profile presents a general parabolic envelope, except the edge is not steeping enough.

With this pulse, which is linearly chirped around the pulse center, a suitable constant anomalous GVD can be designed for pulse compression. The dispersion introduced by a grating can be considered as a pulse compressor, where it imparts different phase delays $\phi_D(\omega)$ to different frequency components. When the instantaneous frequency of a pulse is linearly chirped from $f_0 - k \cdot T/2$ to $f_0 + k \cdot T/2$, where T is the pulse duration and k is a constant, the delay characteristic of a pulse compressor that realigns different frequency components can be expressed

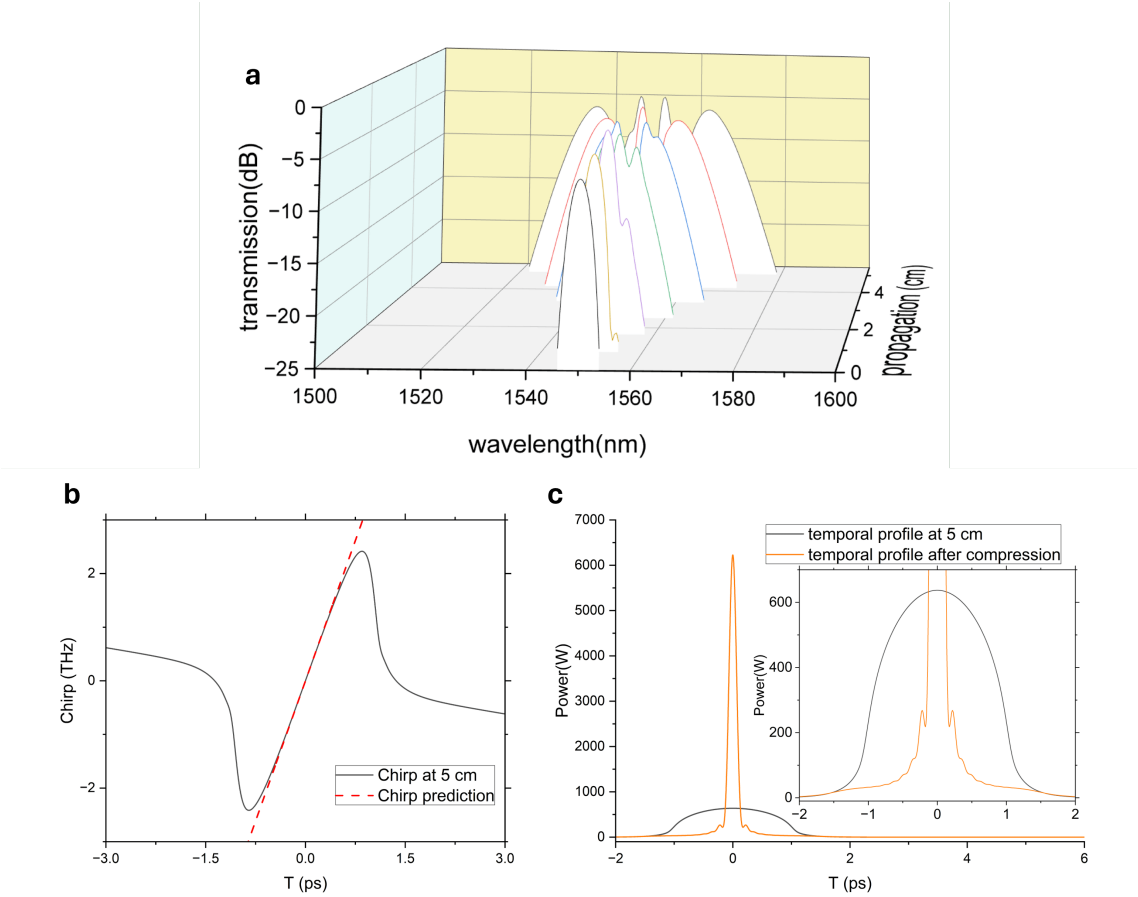

Fig. 7.5. Pulse evolution towards an asymptotic self-similar solution in a 5-cm Si_3N_4 waveguide. The initial pulse FWHM duration is 1 ps (100 W peak power), gain g is 46 m^{-1}, GVD parameter β_2 is 700 ps^2/km. (a) Spectral evolution of input pulse with function of propagation. (b) Chirp of the pulse after 5 cm propagation (in black) and the analytic chirp predicted by Equation.7.7 (in red). (c) The temporal profile after 5 cm propagation is shown in black. The orange curve shows the temporal profile after the pulse being compressed by an anomalous GVD corresponding to the slope of predicted chirp shown in (b). The FWHM pulse duration after compression is 150 fs.

as:

$$\phi_D(\omega) = -\pi \cdot (\frac{\omega - \omega_0}{2\pi})^2 \cdot \frac{1}{k} \tag{7.9}$$

Here, because the pulse propagates towards its asymptotic solution, k is considered as the chirp rate shown in Equation.7.7 as $k = \frac{1}{2\pi}\frac{g}{3\beta_2}$. The response of this compressor to the pulse in the frequency domain is then $\exp(i\phi_D(\omega))$. In this way, the complex field Ψ_c after compression can be expressed as:

$$\Psi_c(z_0, T) = \mathcal{F}^{-1}(\mathcal{F}(\Psi(z_0, T)) \cdot \exp(i\phi_D(\omega))) \tag{7.10}$$

The temporal profile of intensity is $I_c = |\Psi_c|^2$. The temporal profile of the compressed pulse is depicted in Figure 7.5(c) in orange, revealing a full width at half maximum (FWHM) duration of 150 fs, indicating a compression factor of 6.7 times. The compressed pulse predominantly contains its energy within the main peak, with only a minor pedestal observed around it. This pedestal arises from the residual chirp following the non-ideal chirp compensation. Due to the linearization of chirp towards the asymptotic solution as perdicted in Equation 7.7, the

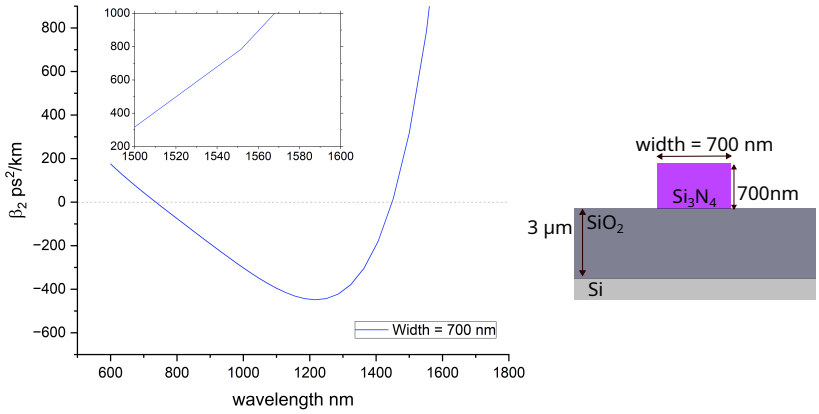

Fig. 7.6. GVD simulation of a strip Si_3N_4 waveguide: 700 nm width and 700 nm height. The third-order dispersion β_3 is the slope of β_2 around 1550 nm.

constant anomalous GVD effectively compensates for most of the pulse duration. The amount of total calculated anomalous dispersion D is expressed as the group delay over the wavelength difference. For this 5-cm Si_3N_4 waveguide, the $D = 0.0716$ ps/nm.

7.1.2 . Influence of higher-order dispersion

The prior examination of SPM and normal GVD has already demonstrated that appropriate parameters can be identified to linearize the chirp as the pulse propagates towards a self-similar regime, thereby indicating the potential for achieving a 150 fs pulse after compression. Nevertheless, given that the bandwidth supporting such short pulses extends to 60 nm around 1550 nm within a -20 dB range, the inclusion of higher-order dispersion (HOD) becomes imperative for integrated waveguides, whereas it is typically negligible in optical fibers[8].
In this analysis, we incorporate third-order dispersion $\beta_3 = -1.44 \cdot 10^{-38}\,\mathrm{s}^3/\mathrm{m}$, derived from β_2 of strip Si_3N_4 waveguide with dimensions of 700×700 nm (Figure.7.6). With the existence of β_3, the GVD varies with wavelengths and thus the pulse undergoes a deviation from self-similar propagation. By taking it into account in NLSE, a simulation result is shown in Figure.7.7 in black dot line (the other curve notations are destined for different initial pulse shapes which will be discussed later). In Figure.7.7(a), it is evident that the overall chirp closely follows the chirp prediction (red curve), with a notable exception at the rising edge side where a more significant misalignment is observed notably at T = -1 ps. Consequently, this results in an asymmetric pulse shape(Figure. 7.7(b)), whereas the pulse shape was perfectly symmetric in the previous case where β_3 was not included. The temporal pulse shape after compression also shows a ripple before the main peak which is also due to the chirp misalignment in Figure 7.7(c). However, the pulse peak power is just slightly lower than the case without β_3 indicating that the perturbation of higher-order dispersion is minor with respective to pulse compression. For later discussions, the simulations are all carried out taking into account β_3.

7.1.3 . Effect of initial pulse condition

As mentioned before, apart from chirp linearization, another advantage to leveraging self-similar propagation in normal GVD is that both the pulse chirp and pulse temporal profile are independent of the initial pulse shape. Here, we investigate three typical temporal pulse profiles: Gaussian shape, Hyperbolic secant shape and filtered Hyperbolic secantshape. The hyperbolic

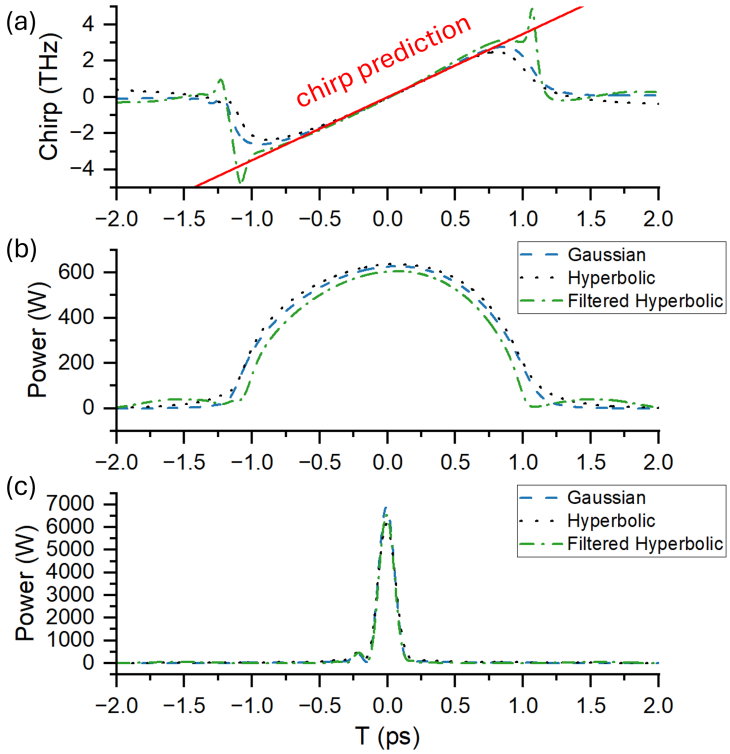

Fig. 7.7. Pulse after 5-cm propagation with different initial pulse shapes The results noted by blue, black, and green are from initial pulse shapes of Gaussian, Hyperbolic secant, filtered Hyperbolic secant, respectively. (a) Pulse chirp and the prediction is shown in red. (b) Pulse temporal profile. (c) Pulse temporal profile after the same anomalous GVD compensation.

secantshape pulse is very common in mode-lock laser. In laboratory settings, a longer pulse is commonly generated by filtering the spectrum of a shorter pulse using a bandpass filter. The filtered hyperbolic secant pulse we utilized to achieve a 1 ps full width at half maximum (FWHM) pulse was obtained by filtering a 190 fs hyperbolic secant pulse through a 7.5 nm bandwidth centered at 1550 nm.

In Figure.7.7, we compare the simulation results of different initial pulse shape with the same parameters as initial peak power of 100 W and pulse duration of 1 ps. Although there are slight differences in details, three different initial pulse shapes present a similar result in terms of pulse chirp, pulse temporal profile which verify the characteristic of self-similar propagation. Pulse temporal profile after compression also shares similar peak power from 6 kW to 7 kW indicating a similar compression factor can be achieved with same anomalous GVD to different initial pulse shape.

Here, the propagation distance is consistently set to 5 cm. A longer propagation distance is typically favored for self-similar propagation, as various initial pulse shapes converge to the asymptotic solution at different distances[3]. Consequently, a longer propagation distance enhances robustness against variations in initial pulse shape[3]. However, it should be noted that when β_3 is taken into account, the convergence to the ideal asymptotic solution is no longer possible. The effect of higher-order dispersion accumulates through the propagation and the pulse chirp will be more misaligned to the linear prediction. The pulse duration T_{FWHM} is about 150 fs after pulse compression, which refers to a 60 nm bandwidth centered at 1550 nm

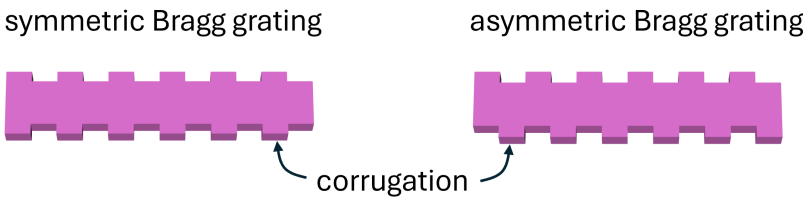

Fig. 7.8. The illustrations of a symmetric Bragg grating and an asymmetric Bragg grating.

at -20 dB range (Figure.7.3(a)). Practically, achieving a grating that introduces anomalous dispersion in this large range is challenging[1]. Therefore, a novel grating designed for short-pulse compression will be introduced in the next section.

7.2 . Pulse compressor

7.2.1 . Principle

To realise pulse compression, a pulse compressor based on dispersive grating is needed. Typically, a dispersive grating works as a reflective device. It achieves a substantial GVD that surpasses the waveguide GVD by up to three orders of magnitude. This is accomplished by reflecting different wavelengths at distinct spatial positions within the grating. The efficient chip-scale integrated of this reflective device commonly requires a circulator [9], which remains a challenge nowadays in silicon phonics. In order to collect the reflected light, one existing solution is using a pair of coupled waveguide grating[10]. Because the coupled mode theory equations are based on two Bragg waveguides, the Bragg detuning, which defines the bandwidth of the pulse compressor, will inevitably be limited by the individual Bragg condition of each Bragg waveguide. To broaden the bandwidth, we disassociate the pulse compressor to a reflective asymmetric Bragg grating and a modal directional coupler. The broad working bandwidths of both components guarantee the expansive bandwidth of the device.
In order to inspect the behavior of the dispersive grating, simulations need to be carried out. The Finite-Difference Time-Domain (FDTD) method is a rigorous and powerful tool for modeling nano-scale optical devices. However, regarding to the length of the device (hundreds of micrometers), 3D FDTD will consume a significant long time, not suitable for device design. Alternatively, varFDTD (or 2.5D FDTD) gives an approximation simulation that simplifies the vertical direction by the effective index of the corresponding slab mode. VarFDTD is suitable for modeling devices that maintain their height.

7.2.2 . Asymmetric Bragg grating

A traditional Bragg grating is a waveguide with corrugation on both sides, in phase (Figure.7.8(a)). If the corrugation on one side are longitudinally offset by half a period compared to those on the other side, this results in an asymmetric Bragg grating shown in Figure.7.8(b). Unlike a symmetric Bragg grating, which reflects fundamental mode (i.e. TE_0) at Bragg wavelength, an asymmetric Bragg grating reflects in higher order mode (i.e. TE_1 mode). This is due to the overlap integral of mode conversion between forward and backward TE_0 is zero for asymmetric index modulation[11]. For a forward propagating TE_0 mode with effective index n_0 and a backward TE_1 in the grating, the Bragg condition is expressed as[12]:

$$\lambda = (n_0(\lambda) + n_1(\lambda)) \cdot \Lambda \tag{7.11}$$

where λ is the Bragg wavelength and Λ is the grating period. The shape of the corrugation is chosen to be sinusoidal in the first place because it is easier to define mask, the illustration of which is shown in Figure.7.9(a).

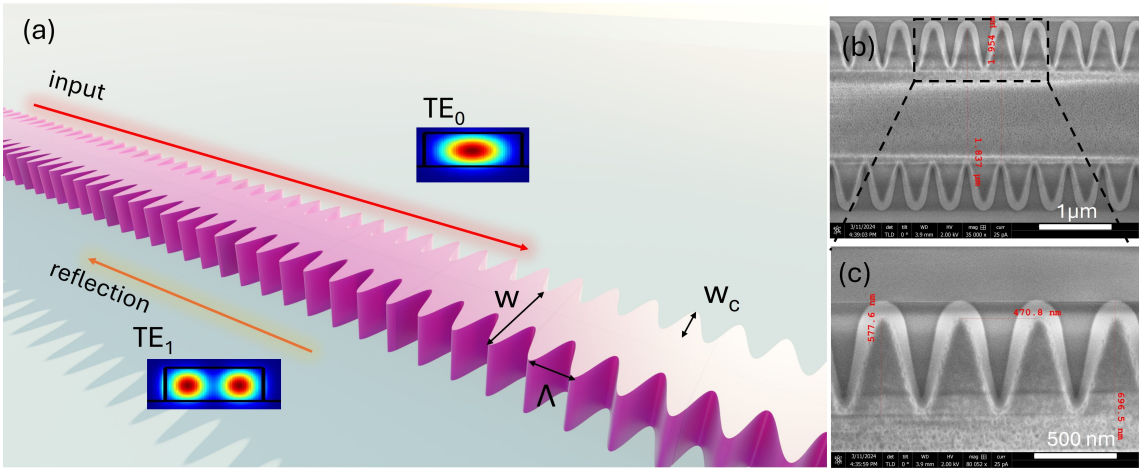

Fig. 7.9. View of asymmetric Bragg grating. (a) The schematic view of the grating. (b) Images by SEM over the corrugation and grating waveguide.

From Equation 7.11, it is evident that both waveguide width w and the grating period Λ can influence the Bragg wavelength λ. However, considering fabrication tolerances, adjusting the waveguide width is preferred, as width variations have a three orders of magnitude smaller impact on the reflection bandwidth compared to variations in Λ [13]. For the two target Bragg wavelengths, $\lambda = 1.6\,\mu\mathrm{m}$ and $1.54\,\mu\mathrm{m}$, the corresponding Bragg waveguide widths w are $1.9\,\mu\mathrm{m}$ and $1.4\,\mu\mathrm{m}$, respectively, as listed in Table 7.1, with a constant period $\Lambda = 470\,\mathrm{nm}$. These wavelengths were chosen to be near $1550\,\mathrm{nm}$ arbitrarily and can be adjusted as needed. The geometric parameters can be fabricated in the C2N cleanroom, and SEM images of the gratings are provided in Figure 7.9(b,c).

Table 7.1. Preliminary design of the asymmetric Bragg grating working for wavelength at 1.6 μm and 1.54 μm.

$\lambda\,(\mu\mathrm{m})$	$w\,(\mu\mathrm{m})$	n_0	n_1
1.6	1.9	1.774	1.635
1.54	1.4	1.754	1.523

To introduce an appropriate group delay between the wavelengths $\lambda = 1.6\,\mu\mathrm{m}$ and $1.54\,\mu\mathrm{m}$, the Bragg wavelength must vary along the asymmetric Bragg grating, resulting in what is known as a chirped Bragg grating. Since we apply a variation in the waveguide width w rather than in the period Λ to modify the Bragg wavelength, the chirped Bragg grating will also be realized through width variations. This causes different wavelengths to be reflected at different locations, thereby introducing a significant group delay. Details can be found later in Section.7.2.5.

7.2.3 . Modal directional coupler

When the forward fundamental mode is reflected to a higher-order mode, a modal directional coupler can convert the higher-order mode back to the fundamental mode through phase

matching of the effective indices n_{eff} of these two modes. For a given wavelength, the effective index of a higher-order mode propagating in a multi-mode waveguide can be equivalent to the effective index of the fundamental mode in a much smaller single-mode waveguide. This effective index phase matching is sensitive to waveguide width, thus resulting in a low fabrication tolerance. Instead, by employing a taper design for both the multi-mode and single-mode waveguides, this phase matching can be maintained over a broad wavelength bandwidth at various positions, robust to fabrication uncertainty. A general guideline can be found in [14].

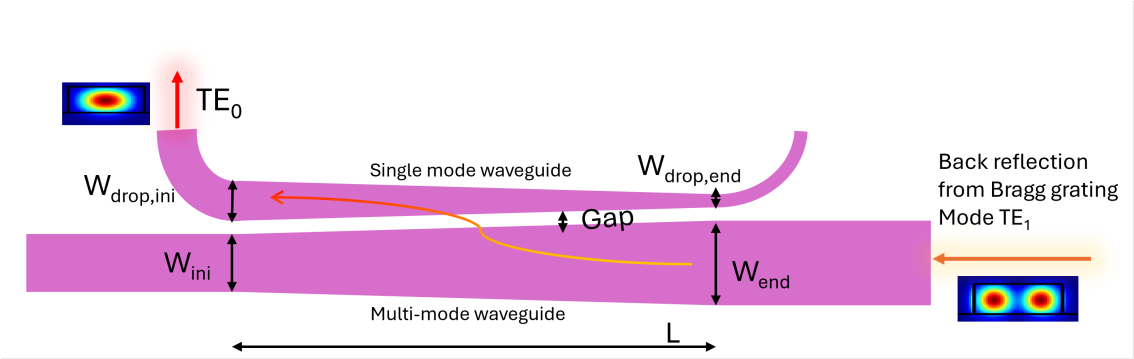

Fig. 7.10. Schematic view of modal directional coupler. The higher order mode is reflected by grating and enters the coupler from the right side. Both the multi-mode and single-mode waveguide are tapered. Important parameters that define the coupler are noted on the figure. Their exact values are shown in Table.7.2

Table 7.2. The geometry of the designed modal directional coupler.

Gap (nm)	L (nm)	W_{ini} (nm)	W_{end} (nm)	$W_{\text{drop,ini}}$ (nm)	$W_{\text{drop,end}}$ (nm)
245	175	1850	2020	995	830

A schematic view of the coupler we designed is shown in Figure.7.10. From the propagation direction of the TE_1 mode, the taper of the multi-mode waveguide decreases in width, while the single-mode waveguide increases in width. The design process and optimization steps to achieve a broadband modal directional coupler are described as follows. First, the center wavelength is set to 1550 nm. The effective refractive index, n_{eff}, as a function of waveguide widths for both the TE_0 and TE_1 modes at 1550 nm is shown in Figure.7.11, where a phase-matching point is identified at the intersection of these two curves, with a width of 920 nm for the TE_0 mode waveguide and 1925 nm for the TE_1 mode waveguide. Taking this phase-matching point as a starting point, a tapered modal directional coupler can be designed. The task is to determine the Gap, L, $W_{\text{drop,ini}}$, $W_{\text{drop,end}}$, W_{ini}, and W_{end}. To achieve this, the particle swarm optimization algorithm has been employed to optimize the transmittance between wavelengths of 1500 nm and 1600 nm. The coupler length L is constrained to be less than 200 $\mu\mathrm{m}$ to minimize the device footprint, and the gap is maintained around 300 nm to ensure sufficient interaction between the two waveguides. The final optimized geometry parameters are shown in Table.7.2.

We examine the performance of this coupler using Lumerical varFDTD. The propagation field profile of power is presented in Figure.7.12(a) showing the mode conversion from TE_1 to TE_0. Although the optimization has been carried out targeting wavelength from 1500 nm to 1600 nm, simulation has been made from wavelength of 1300 nm to 1900 nm to observe its behavior in an

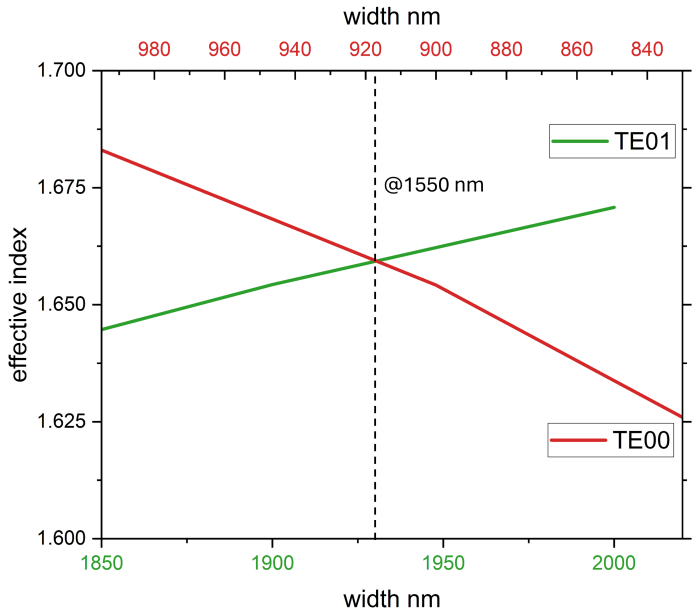

Fig. 7.11. Effective index n_{eff} of TE_0 and TE_1 mode at wavelength 1550 nm. Red curve: n_{eff} of the TE_0 mode as a function of width in the single mode waveguide. Green curve: n_{eff} of the TE_1 mode as a function of width in the multi-mode waveguide. The phase-matching point is noted in the dashed back line.

extensive spectral range. The transmittance in the wavelength range from 1500 nm to 1600 nm reveals a high rate of 98% in Figure.7.12(b). The spectral range that promise a 80% (-1 dB) transmittance is from wavelength of 1400 nm to 1800 nm covering 400 nm bandwidth.

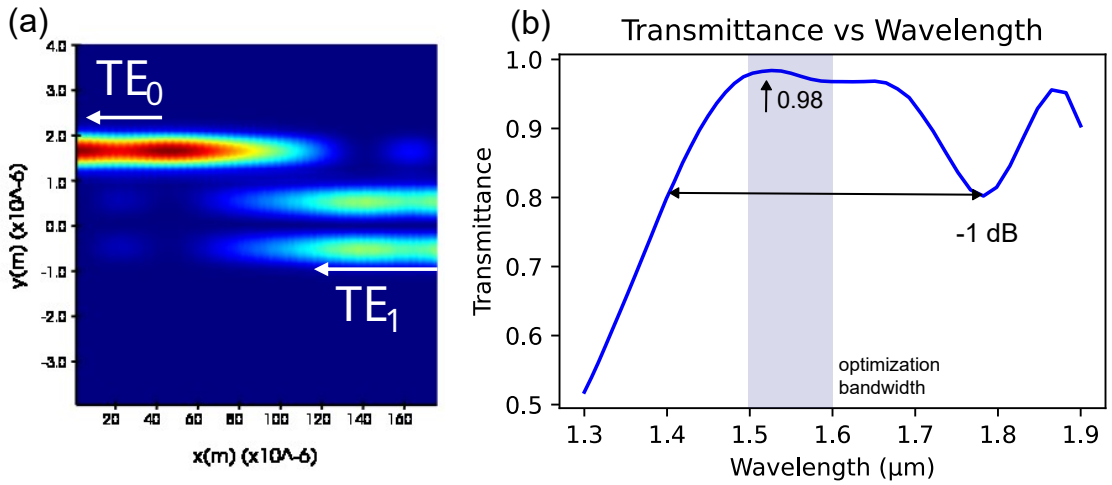

Fig. 7.12. Transmittance of the modal directional coupler. (a) The simulation result of the propagation field profile of power P. (b) The transmittance of the modal direction coupler from wavelength 1300 nm to 1900 nm. The optimisation bandwidth is from 1500 nm to 1600 nm.

7.2.4 . Bragg wavelength and loss

The performance of the compressor is characterized by experimental measurements. Firstly, we monitor the Bragg wavelength of the compressor as well as its insertion loss. The input

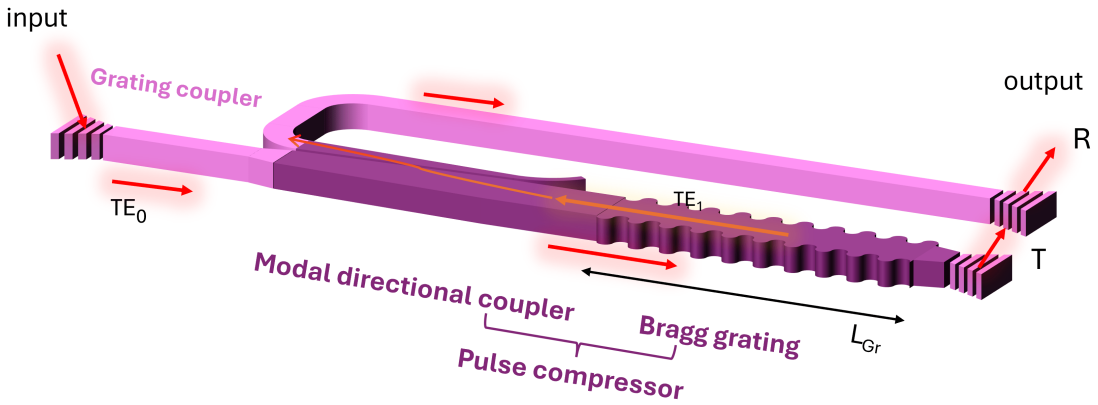

Fig. 7.13. Schematic view of the device to measure Bragg wavelength and loss of the pulse compressor. Grating couplers are equipped to the input and output ports. The R is for reflection and the T is for transmittance. The Bragg grating length L_{Gr} is 100μm. The parameters of the modal coupler can be found in Table.7.2.

mode is fundamental mode TE_0.

A device design, shown in Figure.7.13, is employed for the characterization of a non-chirped pulse compressor. In the input port, the fundamental TE_0 mode is coupled into the device. The laser wavelength that satisfies the Bragg condition (Equation.7.11) will be reflected into the TE_1 mode and then converted back to the TE_0 mode. The signal is finally collected through port R as the reflected signal. For laser wavelengths outside of the Bragg condition, the transmittance T is also measured. The input and output coupling from the chip to the fiber is achieved using a grating coupler.

The choice of the Bragg grating length L_{Gr} is crucial because the corrugation depth w_c will have to adapt to this length to keep a high rejection rate at the Bragg wavelength. The Bragg grating length L_{Gr} is intentionally kept small. This is because the group delay required for pulse compression is $D = 0.0716\,\mathrm{ps/nm}$ (see Section.7.1.1 for more details), resulting in a total chirped Bragg grating length of only a few hundred micrometers. Therefore, the Bragg grating length L_{Gr} for a single wavelength must be sufficiently short. In this design, it is fixed at $L_{Gr} = 100\,\mu\mathrm{m}$.

First, we measured the Bragg wavelength. Three different width of Bragg waveguide widths are fabricated as 1400 nm, 1650 nm, and 1900 nm. For each width, corrugation depth w_c varies from $200\,\mathrm{nm}$ to $600\,\mathrm{nm}$ to investigate its influence on the Bragg wavelength. The measurements were carried out from the transmission side T. The grating coupler response was measured from a reference waveguide and removed from T. The results are shown in Figure.7.14. Multiple notch peaks can be found, corresponding to the Bragg wavelength in TE_1 and TE_0 as marked in Figure.7.14. Knowing TE_0 reflection is totally forbidden in a perfect anti-symmetric Bragg grating[11]; the unexpected TE_0 reflection comes from the fabrication error. The corrugation on one side is not perfectly π shifted from the other because of the stitching error, enabling the reflection. Future investigations will be conducted to determine how to decrease this error. The variation of corrugation depth w_c changes the coupling strength. Therefore, a stronger w_c introduces a higher reflection and broadens reflection bandwidth. Although the Bragg wavelength of TE_1 suffers from a shifting with w_c, they are still not far from the prediction in Table.7.1. The optimal corrugation for different Bragg waveguide widths should be selected

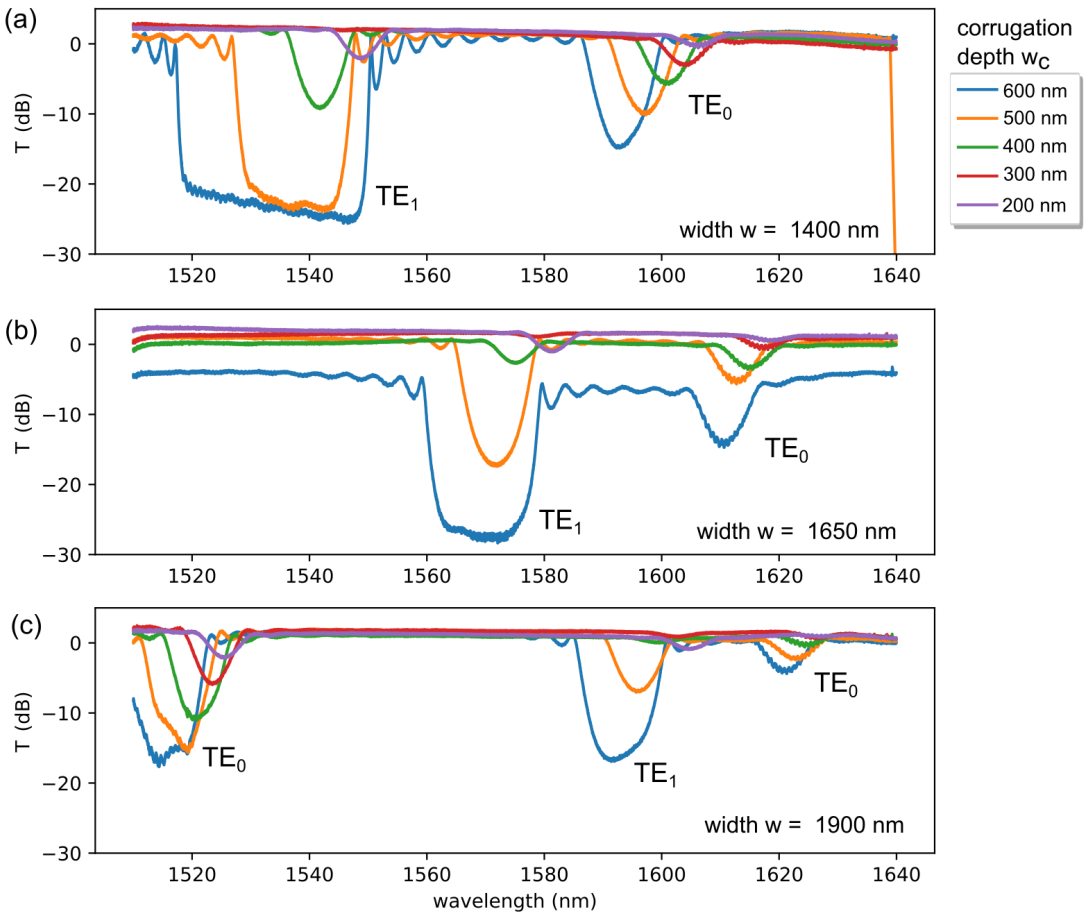

Fig. 7.14. Normalized transmittance of the Bragg gratings in the function of corrugation depth w_c**.** The grating length is fixed at $L_{Gr} = 100\,\mu\mathrm{m}$. The results for Bragg waveguide width $w =$ 1400 nm, 1650 nm and 1900 nm are shown in (a, b, c), respectively.

based on the following criteria: the reflection band must be sufficiently narrow and deep. With these considerations in mind, the preliminary w_c values are chosen to be: $w_c = 400\,\mathrm{nm}$ for width of 1400 nm, $w_c = 500\,\mathrm{nm}$ for width of 1650 nm, and $w_c = 500\,\mathrm{nm}$ for width of 1900 nm.

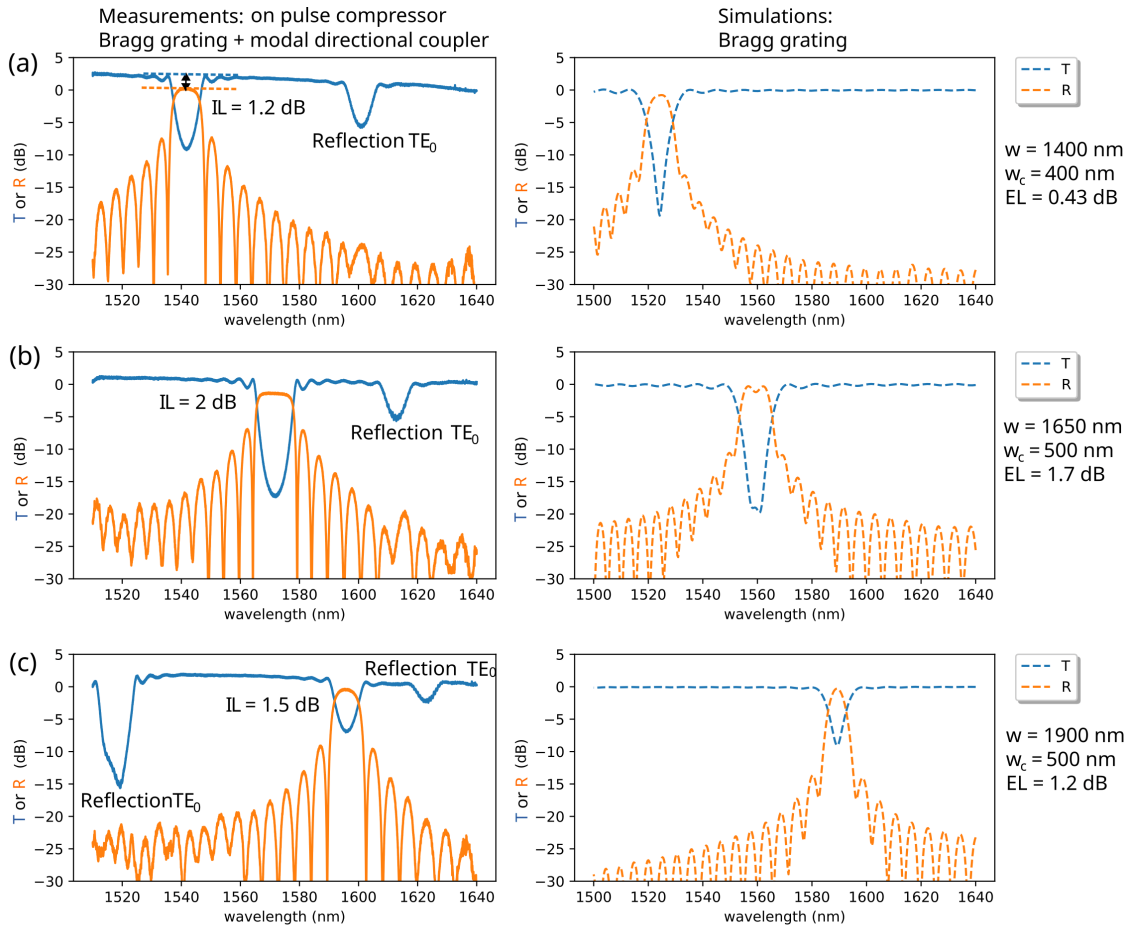

Fig. 7.15. Measurements and simulations of Bragg wavelength and loss. (a) $w = 1400\,\mathrm{nm}$, $w_c = 400\,\mathrm{nm}$ (b) $w = 1650\,\mathrm{nm}$, $w_c = 500\,\mathrm{nm}$ (c) $w = 1900\,\mathrm{nm}$, $w_c = 500\,\mathrm{nm}$. The grating length $L_{Gr} = 100\,\mathrm{nm}$ for all. IL: insertion loss. EL: exceed loss due to the fabrication.

The reflection R (in orange) and the transmittance T (in blue) of the three mentioned pulse compressors are shown in Figure.7.15. The insertion loss (IL) comes from the reflection of the Bragg grating and the transmittance of the modal directional coupler. Experimentally, it is measured by reflection at the Bragg wavelength. Because the normalization using the grating coupler response inevitably causes a little offset to zero level, the IL here is measured by comparing the reflection to this little offset (see Figure.7.15(a)). Among all the measurements, the maximum IL is 2 dB. 2.5D FDTD simulations were carried out on the same geometry only with the Bragg gratings, giving the theoretical transmittance and reflection (Figure.7.15 right column). The simulated Bragg wavelengths are shifted from the measurements. An exceed loss (EL) can be defined by comparing the simulated with measured reflections shown in the inset on the right of Figure.7.15, which indicates the loss due to the fabrication process and the modal directional coupler. The maximum EL is only 1.7 dB. Considering the gratings are patterned on the wafer with fissures as indicated in Figure.4.16 of Chapter.4, a negligible exceed loss can

be expected if we avoid fissure area.
It is also noticeable that the notch peaks in the measured transmittance don't appear as the reflection peaks. This confirms that the notch peaks are associated with the Bragg wavelength in the fundamental mode, as the TE_0 mode cannot pass through the modal directional coupler to the output R port. Apparently, the back reflection of the fundamental mode due to the stitching error limits the bandwidth reachable for the pulse compressor. Before future work to limit this error, the usable bandwidth is from 1540 nm to 1600 nm, covering 60 nm according to Figure.7.15(a) and (b).

7.2.5 . Chirped pulse compressors

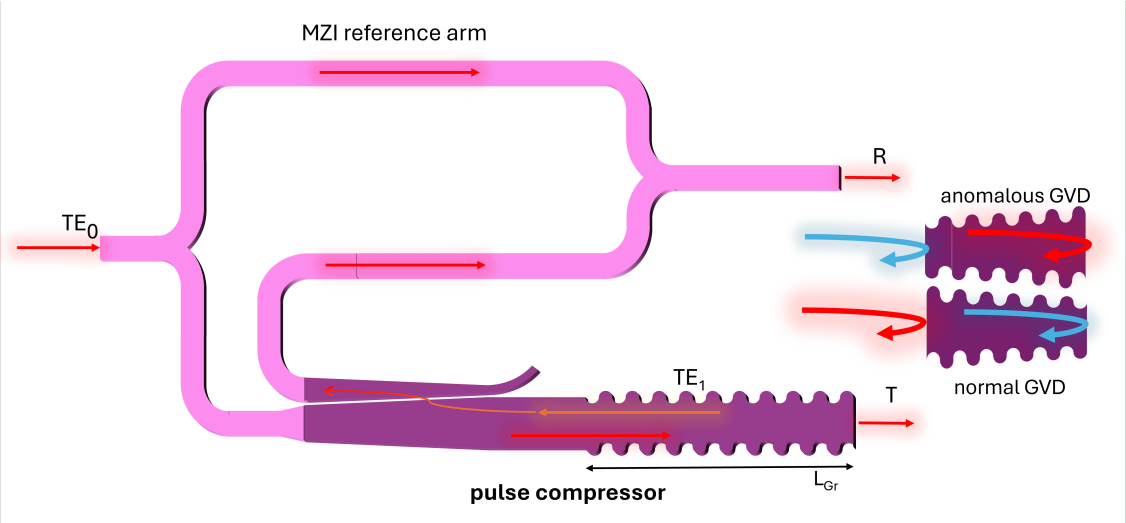

Fig. 7.16. MZI designed for characterization of pulse compressor. The compressor is colored in dark purple. The chirped Bragg grating configurations for normal and anomalous GVD are also shown. The gratings for fiber-to-chip coupling are not shown in the figure.

The Bragg grating must be chirped to introduce the appropriate group delay for pulse compression. As described in Section.7.2.2, the chirping will be achieved through width variation. In the initial design, the width of the Bragg grating w was linearly increased. In this configuration, the shorter wavelength component travels a shorter path, as it is reflected earlier than the longer wavelength component. Consequently, this configuration introduces an anomalous group delay (Figure.7.16). Based on the same principle, if the Bragg grating width w is decreased, it introduces a normal group delay.
The characterization of the group delay is realized by a Mach-Zehnder interferometer (MZI), of which one arm is replaced by the compressor as shown in Figure.7.16. In the input port, the fundamental TE_0 mode is coupled into the MZI which is immediately separated to two arms: one is the reference, and the other goes into the pulse compressor. The laser wavelength that fulfills the Bragg condition in Equation.7.11 will be reflected into TE_1 and converted back to TE_0, interfering with the reference. The final interference will be measured at the R port. The transmittance at T port is also measured. The input and output from the chip to the fiber are realized by the grating coupler, which is not shown here.
The first design is a pulse compressor equipped with a Bragg grating with its width w chirping from 1.4 μm to 1.9 μm. The corrugation depth is fixed at $w_c = 600\,\mathrm{nm}$. The grating length L_{Gr} varies from 500 μm to 100 μm to introduce different group delays. No apodization is

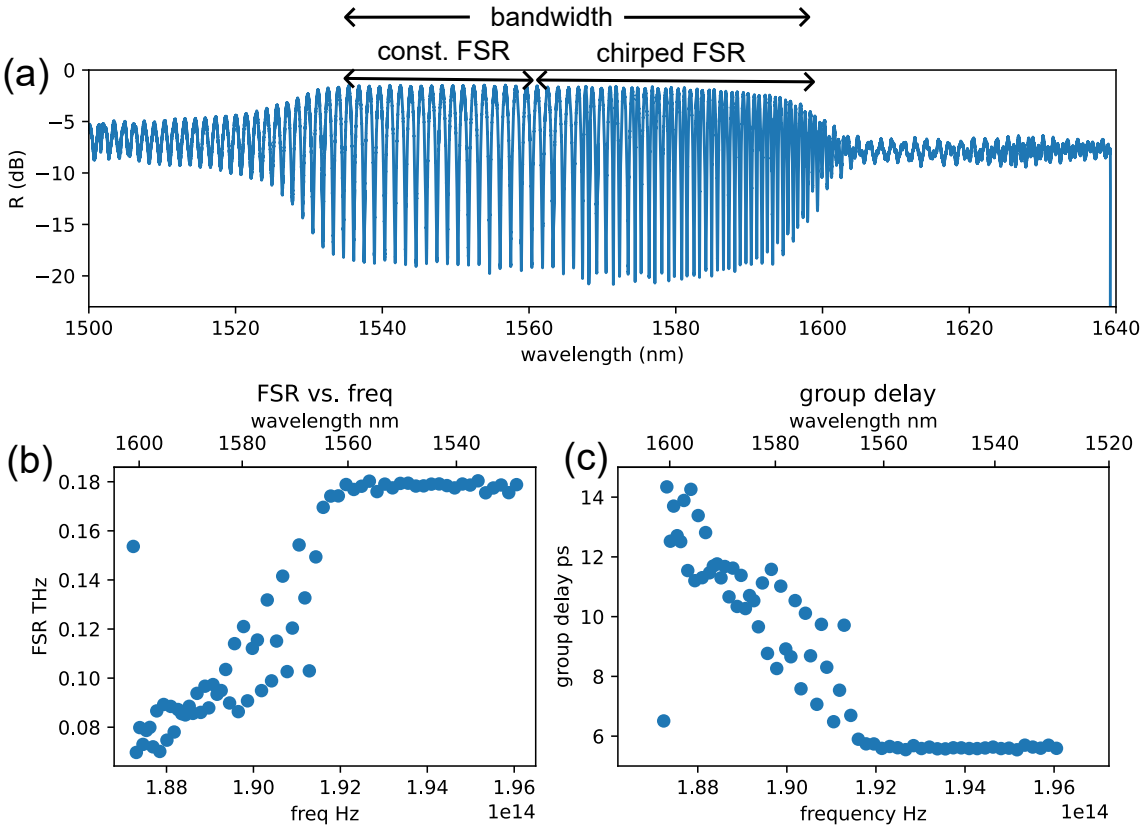

Fig. 7.17. Group delay measurement for the pulse compressor. The pulse compressor has parameters follows: w linear varies from 1.4 μm to 1.9 μm. $w_c = 600\,\mu$m. L_{Gr} = 500 μm. (a) Measurement from the R port the MZI. (b) FSR in frequency. (c) The group delay calculated from Equation.7.14.

introduced between the Bragg grating and the waveguide.

The measurements from the R port of the $L_{Gr} = 500\,\mu$m is shown in Figure.7.17(a). The response of the grating coupler has been removed. Indeed, a large working bandwidth is experimentally observed, which covers from 1530 nm to 1600 nm. The bandwidth coverage has the potential to compress the pulse to 150 fs duration (see details in Section.7.1.1). A clear chirped free spectrum range (FSR) can also be observed. To measure the pulse compressor's group delay, an FSR analysis from has to be carried out[15]. The path length difference between the two arms of MZI can be written as:

$$L(\lambda) = \frac{\lambda^2}{\Delta\lambda \cdot n_g(\lambda)} \tag{7.12}$$

where $\Delta\lambda$ is the oscillation period (thus the FSR in wavelength) and $n_g(\lambda)$ is the waveguide group index. The group delay introduced by the arm of pulse compressor $\tau(\lambda)$ is calculated using:

$$\tau(\lambda) = -\frac{L(\lambda) \cdot n_g(\lambda)}{c} \tag{7.13}$$

where c is the speed of light in the vacuum. Given the relation that $\frac{1}{\Delta\nu} = -\frac{\lambda^2}{c \cdot \Delta\lambda}$, which transfers the FSR in wavelength to FSR in frequency $\Delta\nu$, the group delay can finally be expressed as:

$$\tau(\lambda) = \frac{1}{\Delta\nu} \tag{7.14}$$

The FSR in frequency and the group delay derived are shown in Figure.7.17(b) and (c). While expecting the group delay linearly changing from 1530 nm to 1600 nm, we observed that a significant group delay difference is only present within 1560 nm to 1600 nm. This can be attributed to the excessive corrugation depth, which means that wavelengths from 1530 nm to 1560 nm do not effectively see the 'chirped' grating (see Figure.7.14(a), blue curve). To address this issue, future designs will adjust the corrugation depth w_c alongside the width w, allowing different wavelengths to be reflected at distinct locations within the Bragg grating, thus ensuring a continuous group delay variation across the entire bandwidth.

The group delay dispersion exhibits a predominantly linear behavior, however, with noticeable oscillations. This phenomenon arises due to the absence of apodization in the gratings, a factor that will be investigated in future studies.

Using the gradient of the group delay (the slope regardless of the oscillation), the total calculated dispersions are noted in orange. It can be found that the longer the grating is, the higher the total dispersion it introduced. This is because the path difference between short and long wavelengths increases with L_{Gr}. Their variation as a function of L_{Gr} is also shown in Figure.7.18(f), which presents a linear characteristic as predicted.

Regarding the dispersion that is needed for pulse compression after self-similar propagation given the conditions in Section.7.1.1, the best choice of pulse compressor is the one with grating length $200\,\mu\mathrm{m}$.

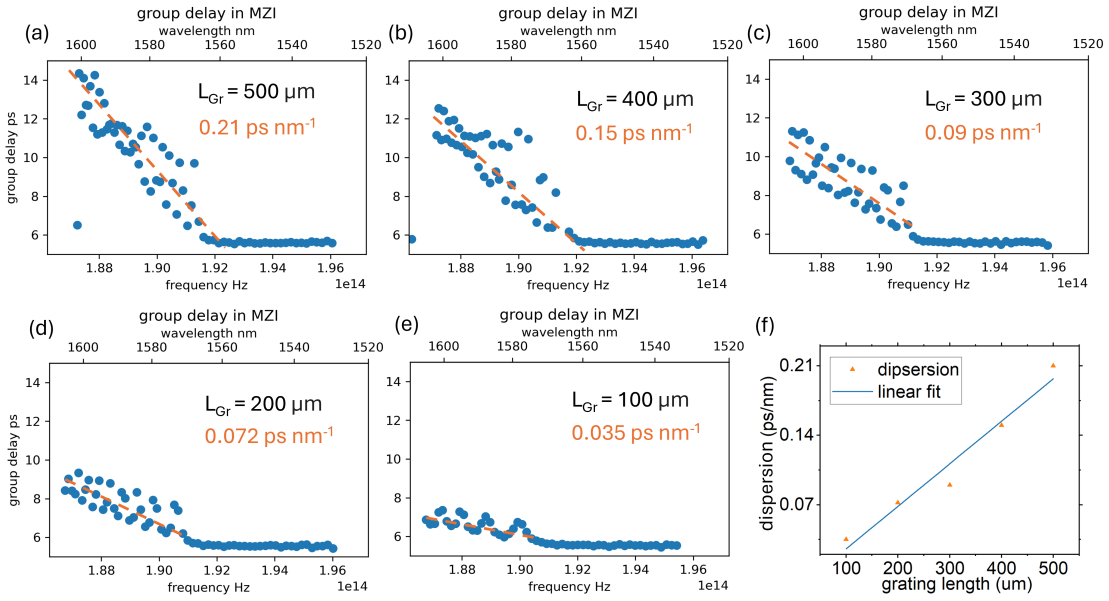

Fig. 7.18. Group delay introduced by pulse compressors of which chirped grating length L_{Gr} vary from $500\,\mu\mathrm{m}$ to $100\,\mu\mathrm{m}$ are shown in (a-e). Their total calculated GVD are noted in orange. (f) Total calculated GVD in the function of L_{Gr}. Linear fitting is shown in blue line.

7.3 . Conclusions and perspectives

In this chapter, we investigated the parameters necessary for on-chip pulse compression with the configuration of a nonlinear stage and a pulse compressor. For the nonlinear stage, self-similar propagation is studied, providing an asymptotic linear frequency chirp. In particular, the gain, GVD, and initial pulse condition within the feasible range are found and discussed. Future work will be emphasized to fabricate the proper waveguide with gain. A possible method could be a hybrid integrated waveguide with amplifier material.
Regarding the pulse compressor, a chirped Bragg grating, and a modal directional coupler are proposed to realize large band dispersion compensation. The bandwidth of the Bragg grating is theoretically unlimited. Therefore, the bandwidth of the pulse compressor is only limited by the modal directional coupler which is at least 100 nm around 1550 nm. A spectral range from 1530 nm to 1600 nm is realised experimentally limited by the stitching error. Suitable corrugation depth and Bragg grating length are also discussed and adapted to the nonlinear stage. Future work will focus on decreasing the stitching error, chirping the corrugation depth, and introducing the apodization[16].

References

[1] J. W. Choi, E. Sahin, B.-U. Sohn, *et al.*, "High spectro-temporal compression on a nonlinear CMOS-chip", en, *Light: Science & Applications*, vol. 10, no. 1, p. 130, 2021, ISSN: 2047-7538. DOI: 10.1038/s41377-021-00572-z.

[2] J. M. Dudley, C. Finot, D. J. Richardson, and G. Millot, "Self-similarity in ultrafast nonlinear optics", en, *Nature Physics*, vol. 3, no. 9, pp. 597–603, 2007, ISSN: 1745-2473, 1745-2481. DOI: 10.1038/nphys705.

[3] V. I. Kruglov, A. C. Peacock, J. D. Harvey, and J. M. Dudley, "Self-similar propagation of parabolic pulses in normal-dispersion fiber amplifiers", en, *Journal of the Optical Society of America B*, vol. 19, no. 3, p. 461, 2002, ISSN: 0740-3224, 1520-8540. DOI: 10.1364/JOSAB.19.000461.

[4] C. Billet, J. M. Dudley, N. Joly, and J. C. Knight, "Intermediate asymptotic evolution and photonic bandgap fiber compression of optical similaritons around 1550 nm", en, *Optics Express*, vol. 13, no. 9, p. 3236, 2005, ISSN: 1094-4087. DOI: 10.1364/OPEX.13.003236.

[5] J. Mu, M. Dijkstra, J. Korterik, H. Offerhaus, and S. M. García-Blanco, "High-gain waveguide amplifiers in Si $_3$ N $_4$ technology via double-layer monolithic integration", en, *Photonics Research*, vol. 8, no. 10, p. 1634, 2020, ISSN: 2327-9125. DOI: 10.1364/PRJ.401055.

[6] K. M. Kiani, H. C. Frankis, H. M. Mbonde, *et al.*, "Thulium-doped tellurium oxide waveguide amplifier with 76 dB net gain on a silicon nitride chip", en, *Optics Letters*, vol. 44, no. 23, p. 5788, 2019, ISSN: 0146-9592, 1539-4794. DOI: 10.1364/OL.44.005788.

[7] H. C. Frankis, H. M. Mbonde, D. B. Bonneville, *et al.*, "Erbium-doped TeO $_2$ -coated Si $_3$ N $_4$ waveguide amplifiers with 5 dB net gain", en, *Photonics Research*, vol. 8, no. 2, p. 127, 2020, ISSN: 2327-9125. DOI: 10.1364/PRJ.8.000127.

[8] "Numerical and experimental study of parabolic pulses generated via Raman amplification in standard optical fibers", en, *IEEE Journal of Selected Topics in Quantum Electronics*, vol. 10, no. 5, pp. 1211–1218, 2004, ISSN: 1077-260X, 1558-4542. DOI: 10.1109/JSTQE.2004.837214.

[9] K. O. Hill, F. Bilodeau, B. Malo, *et al.*, "Chirped in-fiber Bragg gratings for compensation of optical-fiber dispersion", *Opt. Lett.*, vol. 19, no. 17, pp. 1314–1316, 1994, Publisher: Optica Publishing Group. DOI: 10.1364/OL.19.001314.

[10] D. T. H. Tan, K. Ikeda, and Y. Fainman, "Coupled chirped vertical gratings for on-chip group velocity dispersion engineering", en, *Applied Physics Letters*, vol. 95, no. 14, p. 141 109, 2009, ISSN: 0003-6951, 1077-3118. DOI: 10.1063/1.3242028.

[11] J. Castro, A. Sato, and D. Geraghty, "Waveguide mode conversion using anti-symmetric gratings", en, in *OFC/NFOEC Technical Digest. Optical Fiber Communication Conference, 2005.*, Anaheim, CA, USA: IEEE, 2005, 3 pp. Vol. 1, ISBN: 978-1-55752-783-7. DOI: 10.1109/OFC.2005.192522.

[12] H. Qiu, J. Jiang, P. Yu, *et al.*, "Silicon band-rejection and band-pass filter based on asymmetric Bragg sidewall gratings in a multimode waveguide", en, *Optics Letters*, vol. 41, no. 11, p. 2450, 2016, ISSN: 0146-9592, 1539-4794. DOI: 10.1364/OL.41.002450.

[13] F. Zhang, J. Dong, Y. Zhu, X. Gao, and X. Zhang, "Integrated Optical True Time Delay Network Based on Grating-Assisted Contradirectional Couplers for Phased Array Antennas", *IEEE Journal of Selected Topics in Quantum Electronics*, vol. 26, no. 5, pp. 1–7, 2020, ISSN: 1077-260X, 1558-4542. DOI: 10.1109/JSTQE.2020.2983579.

[14] H. Shu, B. Shen, Q. Deng, M. Jin, X. Wang, and Z. Zhou, "A Design Guideline for Mode (DE) Multiplexer Based on Integrated Tapered Asymmetric Directional Coupler", en, *IEEE Photonics Journal*, vol. 11, no. 5, pp. 1–12, 2019, ISSN: 1943-0655, 1943-0647. DOI: 10.1109/JPHOT.2019.2941742.

[15] D. T. Tan, P. C. Sun, and Y. Fainman, "Monolithic nonlinear pulse compressor on a silicon chip", en, *Nature Communications*, vol. 1, no. 1, p. 116, 2010, ISSN: 2041-1723. DOI: 10.1038/ncomms1113.

[16] Y. Li, L. Xu, D. Wang, Q. Huang, C. Zhang, and X. Zhang, "Large group delay and low loss optical delay line based on chirped waveguide Bragg gratings", en, *Optics Express*, vol. 31, no. 3, p. 4630, 2023, ISSN: 1094-4087. DOI: 10.1364/OE.480375.

8 - Summary and future work

Summary

8.1 . Summary

An on-chip supercontinuum source has garnered significant attention in research due to its potential to provide compact light sources for applications in metrology, spectroscopy, imaging, and telecommunications, while maintaining a portable device size and minimizing energy consumption. Silicon photonics has become essential in realizing this vision, thanks to its high nonlinearity, mature fabrication processes, and non-toxic properties. In particular, silicon nitride (Si_3N_4) has emerged as one of the most promising material platforms for applications in the visible and infrared spectral ranges, due to its wide transparency window and low-loss characteristics. This manuscript investigates potential solutions to the challenges associated with supercontinuum generation (SCG) on the Si_3N_4 platform, aiming for a flexible SCG with reduced pump power requirements,

The study leverages high-quality, ultra-low-loss buried Si_3N_4 fabrication provided by the CEA LETI foundry while also working to develop fabrication processes within the C2N cleanroom, aiming for greater flexibility and the capability to achieve smaller feature sizes. Both of them are addressed in Chapter.4. While Si_3N_4 waveguides fabricated in the C2N cleanroom demonstrate low propagation losses, the primary challenges involve addressing stress-induced fissures and the presence of micro-pillars within the trench. Various characterization techniques have been developed to effectively monitor waveguide losses and dispersion properties.

The nonlinear characterization is performed on a width-invariant Si_3N_4 waveguide fabricated at C2N, as discussed in Chapter 5. The details of the measurements are presented, including the experimental setup, coupling efficiency estimation, spectral broadening, and temporal coherence analysis.

To overcome the limitations of current dispersion engineering, a novel method has been introduced to tailor spectral broadening by generating multiple dispersive waves (DWs) as defined by the quasi-phase-matching (QPM) condition. By introducing periodicity in the waveguide width, dispersion is modulated, which directly influences nonlinear dynamics and facilitates DW generation under QPM conditions. The design guidelines for this approach are detailed in Chapter 6. Both experiments and simulations under various dispersion conditions have been conducted to examine the spectral broadening based on the QPM condition. This method serves as a valuable complement to current dispersion engineering and can be applied across different material platforms.

To decrease the demand for ultra-short and high-power pump pulse for SCG, the necessary building block of pulse compression is studied in Chapter.7. A theoretical study of self-similar compression adapted to Si_3N_4 is carried out including an amplified pulse propagation in normal dispersion and a pulse compressor. Given the initial 1 ps pulse with a peak power of 100 W, a linear chirped amplified pulse is achieved in a 5 cm long waveguide with a gain of 2 dB/cm.

This linear chirp characteristic is robust to higher-order dispersion and initial pulse shape. A wide-band pulse compressor is also proposed to provide adequate dispersion compensation. The compressor features an asymmetric Bragg grating combined with a modal directional coupler. The design offers a bandwidth of 70 nm around the wavelength of 1550 nm, which supports pulse compression down to 150 fs. The bandwidth is limited by the stitching error during the fabrication. These preliminary results indicate an exciting future of ultra-short pulse compression in the integrated waveguide.

8.2 . Future work

Up til now, all the on-chip SCG demonstration need a table scale ultra-short femtosecond laser. Although the peak power of pump has been largely reduced comparing to fiber platform, the ultra-short pump pulse duration is inevitable for high energy conversion efficiency. Therefore, towards a fully integrated Si_3N_4 SCG system, more effort needs to be made in pulse compression.

In the short term, work will follow the guidelines outlined in Chapter 7 to achieve self-similar pulse compression. The first task will be to experimentally demonstrate self-similar pulse propagation, as described in Section 7.1.1, using hybrid integrated erbium-doped crystalline oxide on Si_3N_4 waveguides. This amplification step will prepare the broadened and chirped spectrum for pulse compression. Concurrently, the design of the pulse compressor will be further investigated, focusing on achieving a wide, oscillation-free linear group delay. Key areas of study will include apodization techniques and eliminating stitch errors during fabrication.

In the mid-term, the goal will be to integrate the pulse compression stage with the waveguide for SCG. The aim is to produce an octave-spanning coherent supercontinuum using picosecond pulses. In the long term, with sufficient on-chip amplification, an integrated laser source will be added, ultimately leading to a fully integrated on-chip SCG system.

List of Tables

List of Figures

List of Publications

In peer reviewed journals:[1], [2].
In conference:[3]–[5].

References

[1] Y. Yang, V. Turpaud, C. Lafforgue, *et al.*, "Generation of multiple user-defined dispersive waves in a silicon nitride waveguide", en, *Optica*, vol. 11, no. 8, p. 1070, 2024, ISSN: 2334-2536. DOI: 10.1364/OPTICA.521625.

[2] R. Fernández De Cabo, A. Sánchez-Sánchez, Y. Yang, *et al.*, "Broadband mode exchanger based on subwavelength Y-junctions", en, *Nanophotonics*, vol. 13, no. 21, pp. 4037–4045, 2024, ISSN: 2192-8614. DOI: 10.1515/nanoph-2024-0291.

[3] Y. Yang, V. Turpaud, C. Lafforgue, *et al.*, "Controlled spectral enhancement in supercontinuum generation by quasi-phase matching Si $_3$ N $_4$ waveguide", in *2024 IEEE Silicon Photonics Conference (SiPhotonics)*, Tokyo Bay, Japan: IEEE, 2024, pp. 1–2, ISBN: 9798350394047. DOI: 10.1109/SiPhotonics60897.2024.10543780.

[4] Y. Yang, C. Lafforgue, Q. Wilmart, *et al.*, "Supercontinuum generation in 800nm thick ultra-low loss silicon nitride waveguides", in *Smart Photonic and Optoelectronic Integrated Circuits 2023*, S. He and L. Vivien, Eds., San Francisco, United States: SPIE, 2023, p. 2, ISBN: 978-1-5106-6437-1. DOI: 10.1117/12.2657444.

[5] V. Turpaud, N. Koompai, T. H. Nhi Nguyen, *et al.*, "Enhancing Mid-Infrared Supercontinuum Generation at Low Pump Power in SiGe Waveguides", in *2023 Conference on Lasers and Electro-Optics Europe & European Quantum Electronics Conference (CLEO/Europe-EQEC)*, Munich, Germany: IEEE, 2023, pp. 1–1, ISBN: 9798350345995. DOI: 10.1109/CLEO/Europe-EQEC57999.2023.10232668.